Numerical Study of a Micro-Swimmer using an Immersed Boundary Method

Aditya Kumar

Technische Universiteit Delft

TU Delft Delft University of Technology

Challenge the future

Numerical Study of a Micro-Swimmer using an Immersed Boundary Method

by

Aditya Kumar

in partial fulfillment of the requirements for the degree of

Master of Science
in Mechanical Engineering

at the Delft University of Technology,
to be defended on Friday February 23, 2018 at 10:00 AM.

P&E Report Number: 2882

Supervisors:	Prof. dr. ir. G. Ooms	TU-Delft
	Dr. ir. M.J.B.M. Pourquie	TU-Delft
Thesis committee:	Dr. Cristian Picioreanu	TU-Delft
	Dr. Daniel Tam	TU-Delft

Acknowledgements

I would like to thank my supervisors Prof.dr.ir. Gijs Ooms and Dr. Mathieu Pourquie for their supervision and guidance during this thesis. I would also like to thank them for providing feedback on my lunch talk and the thesis report. Furthermore, I would like to thank Dr. Daniel Tam and Dr. Cristian Picioreanu for accepting to be part of the thesis committee.

Special thanks go out to *Digvijay, Keerthi, Sai,Naren,Veera and Vaibhav* for all their help and useful feedback on my thesis report. Enriching discussions with them on *State capitals, PhD, Coimbatore, Mixture, Netayan, Thata and Indian classical music* has made my experience of working in the laboratory more enjoyable. Thank you *Ankit and Abhiroop* for all those memorable conversations on *UP, Dhanbad and Wasseypur*. Somewhere in the near future, we could start a business there. Thank you *Antaran* for all of your interesting insights into Fluid Dynamics, and those wonderful visits to The Hague. Thank you *Carsten* for the insights from your Judo lessons. They were very useful to me in my thesis.

Last but not the least, i would like to thank my parents and relatives in India, for all their love, support and encouragement.

Abstract

The environment in which microscopic organisms live in is dominated by viscous forces because of their small length scales. Inertial forces are of little use to them in their propulsion mechanisms. As a consequence of this, an organism such as the scallop which moves through time-reversible deformations of its body would not propel itself in a regime dominated by visocus forces. Hence, microscopic organisms use appendages like cilia and flagella that are not time reversible to move forward. However, inertial effects become important to microscopic organisms at the relevant time and length scales. For example, inertia is used by a microscopic organism such as *Paramecium* to escape/attack its predator/prey [Hamel et al., 2011].

The effects of inertia on the model of a spherically ciliated micro-organism are studied numerically using an Immersed Boundary Method (IBM) in the present work. In this model given by [Felderhof, 2015], the distortions of the *envelope* that is generated by connecting all the tips of the cilia together, are prescribed. The unsteady Reynolds number ($Re_\omega = \frac{\omega L^2}{\nu}$) which characterizes the influence of unsteady inertia that is generated by the beat of the organism, is varied from 0.025 to 18. The code which uses a Volume Penalization/Volume of Solid IBM to simulate the distorting sphere is validated for several test cases.

The mean swimming velocity of the organism that is obtained numerically from the code is in agreement with the analytical model for two cases of the unsteady Reynolds number. The mean swimming velocity is found to decrease at increasing inertia. The flow pattern that is obtained in the near-field as a result of the distorting sphere is significantly different from those obtained with the existing models available in literature.

Contents

List of Tables

List of Figures

1

Introduction

1.1. Low Reynolds Number Flows

Micro-organisms inhabit an environment dominated by viscous forces because of their small length scales. For a human being with a typical length scale (L) of 1 m, swimming in water with an average velocity (U) of 1 $\frac{m}{s}$, the Reynolds number,*Re*, (defined as the ratio of inertial to viscous forces) is 10^6, while for some micro-organisms (L ≈1 μm, U≈30 $\frac{\mu m}{s}$), it is 10^{-5}. In such an "inertialess" environment (Re « 1), the mechanism of locomotion of a micro-organism differs from that of a macroscopic organism. A macroscopic organism such as a scallop owes its ability to propel forward to inertial forces by slowly opening and rapidly closing its shells in a reversible manner as shown in Fig. 1.1. In closing its shell rapidly, it expels the fluid between its shells, thereby moving forward. In a microscopic environment however, this reciprocal motion of the scallop would not help it or any other organism to move forward. This is known as the Scallop theorem [Purcell, 1977].

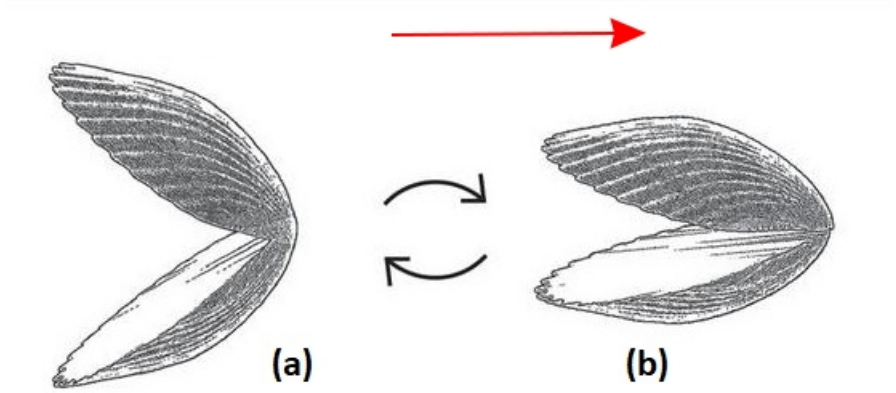

Figure 1.1: A scallop moving by opening (frame *a*) and closing its shells (frame *b*). The direction of its motion is towards the right as shown by the red arrow. This mechanism of motion is termed as jumping. Reproduced from [Qiu et al., 2014].

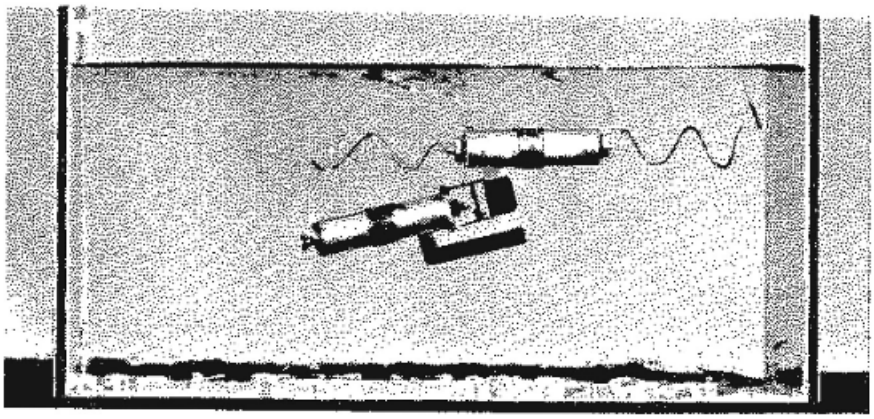

Figure 1.2: Swimming devices as shown in the film *Low Reynolds Number Flows* by G.I Taylor. The first device from bottom employs a time reversible flapping motion. Unlike the second device from the bottom, it does not swim in the highly viscous fluid surrounding it [NCFMF, 1972].

Sir Geoffrey Ingram Taylor has shown a demonstration of the Scallop theorem in his film *Low Reynolds Number Flows*. In the film, two model-swimmers were shown. The first swimmer (the first device from the top in Fig. 1.2) employed a spiral to propel itself, while the second swimmer (the second device from the top in Fig. 1.2) employed a time-reversible flapping tail to propel itself. It was shown that when the second swimmer was put into a highly viscous fluid, it did not produce a net motion. This was because, the motion produced by the forward stroke of the flapping tail was cancelled by the motion produced by its backward stroke. In conclusion, the exact mechanisms of the locomotion used by a macroscopic organism cannot be employed by an organism living at the micro-scale. Naturally, the question arises as to how does a microscopic organism propel itself forward.

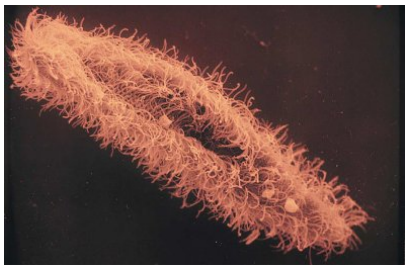

(a) Cilia on a *Paramecium* cell.
Reproduced from [Valentine et al., 2012].

(b) A spermatozoon whipping its flagellum to propel forward. Source : *images.thevine.com.au*

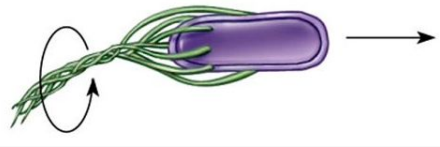

(c) Bacterium rotating its flagellar bundle to propel forward.
Reproduced from [Cowan, 2018].

Figure 1.3: Flagellated and Cilated micro-organisms.

A microscopic organism propels forward by employing deformations through its appendages such as cilia (hair-like structures) and flagella (whip-like structures) as shown in Fig. 1.3a & 1.3b, 1.3c respectively. These are not time-reversible and thus help the organism to move [Blake, 1971]. The differences between cilia and flagella come through their sizes and beat sequences. Flagella average around 10μm in size and beat in a sinusoidal fashion while cilia are much shorter averaging around 2

μm in size and have two distinguishing stages in a beat [Elgeti et al., 2015]. The differences between their beat sequences will be explained in a following section.
The earliest of models to study the swimming of microscopic organisms (with flagella) was proposed by G.I Taylor in 1951 [Taylor, 1951]. He considered an *inextensible* sheet which propagates transverse waves along its length and has calculated its mean swimming velocity to the fourth order in its amplitude. The direction of swimming of the sheet and its physical interpretation is summarized below.

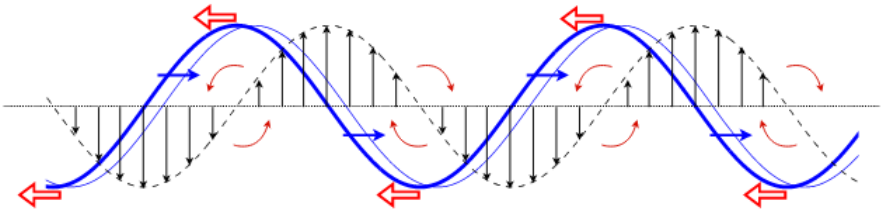

Figure 1.4: Taylor's swimming sheet. The thick blue line represents the wave at the time instant *t*. Wave at a time instant $t+\Delta t$ is represented by the thin blue line. Velocities of the material points on the sheet are represented by the black vertical arrows. Curved red arrows represent vorticities induced by the velocities. The blue arrows indicate the direction of propogation of the wave. The sheet swims in the opposite direction as indicated by the red arrows. Reproduced from [Lauga and Powers, 2009].

As seen in Fig. 1.4, the sheet moves towards the left by propagating transverse waves along its length in the opposite direction (towards the right). The wave at a time instant 't' displaces to the right in a small time interval 'Δt'. The propagation of the wave results in positive (upward) and negative (downward) velocities along the length of the sheet, inducing an alternating profile of vorticity. The vorticity is anti-clockwise at the crests and clockwise at the troughs of the wave. The induced flow due to the vorticity at the crests and the troughs is towards left. Hence the sheet swims to the left. [Lauga and Powers, 2009].

Flagellated micro-organisms as shown in Fig. 1.3b and 1.3c are driven by a single flagellum or by rotating bundles of flagella. Ciliated micro-organisms on the other hand have several rows of cilia attached to their surface as shown in Fig. 1.3a. The beat cycle of a single cilia can be categorized into a power stroke and a recovery stroke as shown in Fig. 1.5.

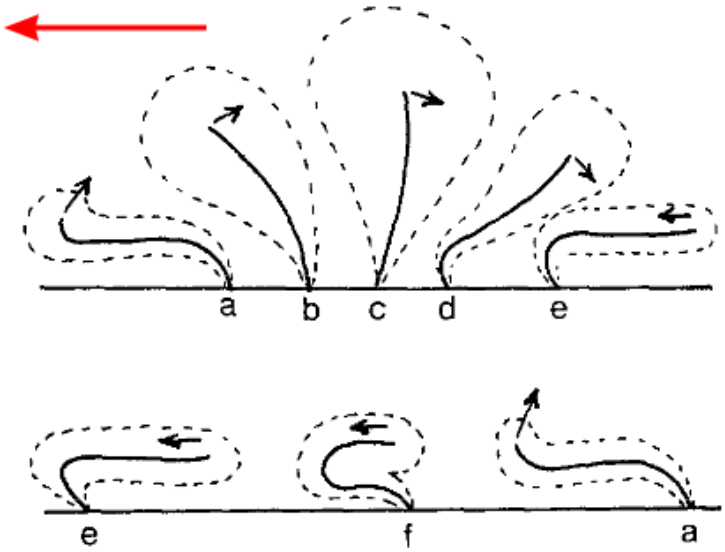

Figure 1.5: Power and recovery stroke of a single cilium attached to the cell surface (black horizontal straight line). The frames *a* to *e* in the top row represent the power stroke and the frames *e* to *a* in the bottom row denote the recovery stroke. Red arrow indicates the direction of the motion of the cell. Reproduced from [Sleigh, 1989].

During the power stroke as shown by the frames a to e in the top row in Fig. 1.5, the motion of the cilium is fast and not bent. In the recovery stroke as shown by the frames *e* to *a* in the bottom row, the cilium folds in such a way that it moves tangentially to the fluid, gradually coming back to its original position. The drag acting on the cilium when it is perpendicular to the cell surface (frame *c*) is twice the drag acting on it when it is parallel to the cell surface (frame *f*) [Tillett, 1970]. This generates a net motion in the forward direction as shown by the red arrow.

In nature, several organisms such as *Opalina* or *Paramecium* have a surface shrouded with rows of closely packed cilia. The beat of each cilium is therefore not isolated and is hydrodynamically influenced by its neighbours [Sleigh, 1989]. Hence, neighbouring cilia beat out of phase with each other, leading to a non-synchronous, wave-like pattern as shown in Fig. 1.6. These are known as Metachronal waves[1][Tamm and Horridge, 1970].

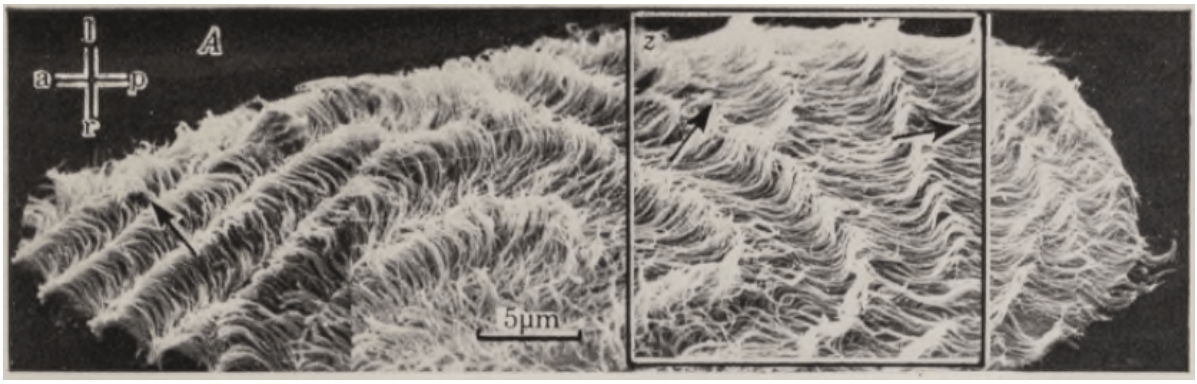

Figure 1.6: Metachronal waves of Cilia on the surface of the micro-organism *Opalina*. Black arrows indicate the direction of propagation of the waves. Reproduced from [Tamm and Horridge, 1970].

The earliest model for ciliary propulsion was developed by Lighthill in 1952 [Lighthill, 1952]. He models a spherical micro-organism whose surface is densely covered with short, closely packed cilia. Because of the length[2], density and closely packed nature of the cilia, their tips are considered to form a flexible, impermeable sheet, thus forming an envelope around the organism as shown by Fig. 1.7. He considers small amplitude perturbations 'ϵ' of the envelope and calculates the mean swimming velocity to the second order in its amplitude (ϵ^2). This is known as the spherical squirmer model or the envelope model. A 'steady' squirmer model can be obtained by neglecting the radial deformations of the envelope and by assuming that the tangential velocities on the mean surface of the envelope do not vary in time.

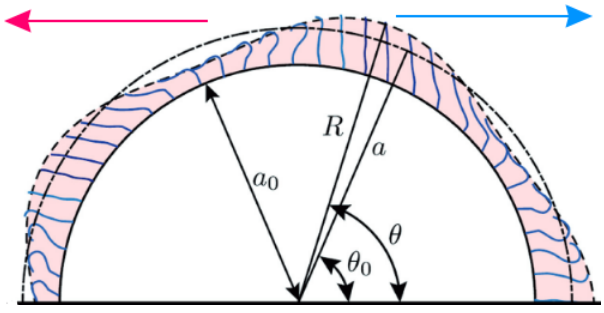

Figure 1.7: The envelope model (one-half) developed by Lighthill [Lighthill, 1952]. The sphere with radius a_0 indicates the cell surface. The region covered by cilia is given in pink and the dashed lines bordering the pink region denote the envelope. The sphere with radius *a* denotes the mean surface of the envelope. Magenta and blue arrows indicate the direction of propagation of the wave and the direction of swimming respectively. Reproduced from [Pedley, 2016].

[1] The reasons for the appearance of these waves are not yet completely understood, though hydrodynamic influences between cilia adjacent to each other seem to be one of the possible reasons [Guirao and Joanny, 2007].

[2] Cilia in organisms such as *Opalina* and *Paramecium* are typically 20 times shorter than their body lengths and are spaced at 65 times shorter than their body lengths [Childress, 1981].

The steady squirmer model has been widely used across literature to study the influence of inertia on self-propelled bodies [Wang and Ardekani, 2012a], nutrient uptake by micro-organisms [Magar and Pedley, 2005], interaction between swimmers [Ishikawa et al., 2006], and dynamics of bacterial suspensions [Ishikawa and Pedley, 2007]. This thesis aims to study the effects of inertia on the combined-stroke-swimmer (explained in the following section) which cannot be realized by the steady squirmer model. Inertia is used by organisms living at the micro-scale as their escape mechanisms which involve fast time scales. *Paramecium* uses inertia to flee/attack its predator/prey or while responding to a localized stimuli [Hamel et al., 2011].

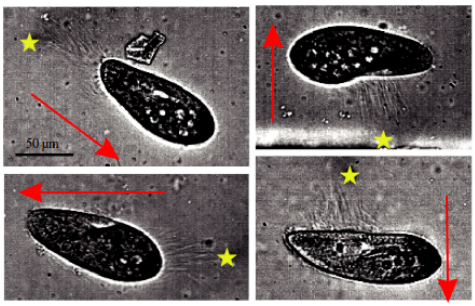

Figure 1.8: *Paramecium* fleeing by ejecting thin rod-like structures in response to localized heating by a laser as shown by the yellow star. The ejections are directed towards the laser source. The direction of its escape is shown by the red arrows. Reproduced from [Hamel et al., 2011].

As shown in Fig. 1.8, *Paramecium*, which is sensitive to temperature, ejects thin rod like structures known as *Trichocysts* in the direction of the laser (shown by the yellow star) to escape from localized heating. The discharge of these structures is done in such way that the drag acting on the ejected structures balances the drag acting on the cell escaping in the opposite direction (shown by the arrows in red).

In addition to using inertia while escaping, inertial effects become important to organisms as they grow in size during their life cycles to larger length scales. Organisms such as fish larvae for example, emerge from their eggs into a viscosity dominated regime ($Re < 20$). During their lifecycle, they grow in size to length scales large enough to use inertia to propel their bodies ($Re \approx 10^3$), eventually reaching adulthood [Müller and Videler, 1996]. Fig. 1.9 depicts the length scales at which inertia can become important to swimming organisms.

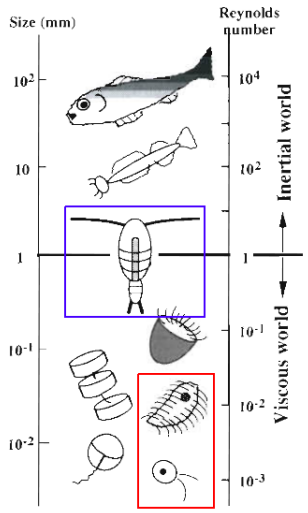

Figure 1.9: Length scales and their associated Reynolds numbers for swimming organisms. *Paramecium* (first from the top in the red box) and *Chlamydomonas* (second from the top in the red box) live in a viscosity dominated regime. Coepods (shown in the blue box) measure about 1 *mm* in size and live at the border between inertia and viscosity dominated regimes. Reproduced from [Naganuma, 1996].

1.2. Immersed boundary methods

The technique used in this thesis to study the effects of inertia is called an Immersed boundary method (IBM) [Mittal and Iaccarino, 2005]. It uses cartesian grids to simulate fluid flow. It was introduced by Peskin [Peskin, 1972] in 1972 to simulate flow around heart-valves. Commercial software packages such as ANSYS-FLUENT use body-conforming grids as shown in Fig. 1.10 to numerically solve the Navier-Stokes equations.

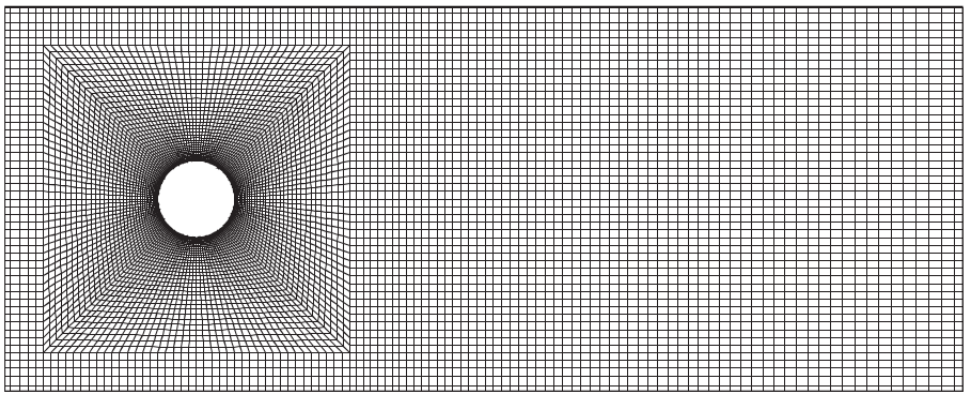

Figure 1.10: A body conforming grid used to simulate a flow over a cylinder at a Reynolds number of 150, cells close to the cylinder wall are made finer to resolve the boundary layer. Reproduced from [Behara and Mittal, 2010].

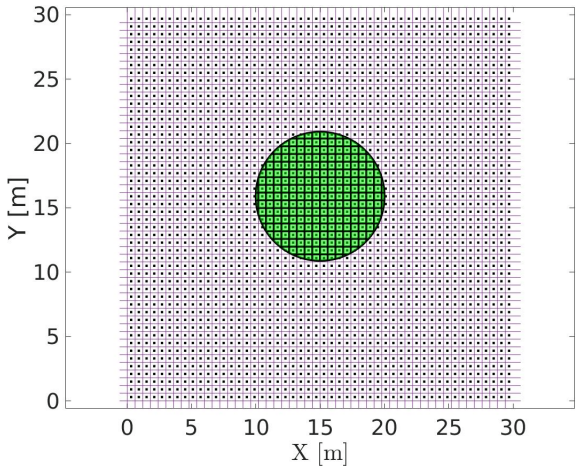

Figure 1.11: A non-body conforming grid used by an Immersed boundary method (IBM). The grid cuts across the cylinder as shown in green.

Simulating the fluid flow around a deforming/moving object by using a body-conforming grid is a time-consuming and error-prone process. This is because the grid needs to be re-generated at every time-step, and the solution computed from the previous time-step needs to be projected onto the new grid. An alternative to this is using an Immersed boundary method (IBM).

The grid used by this technique, cuts across the body and modifies the Navier-Stokes equations in the vicinity of the object as shown in Fig. 1.11, to satisfy the no-slip and no-penetration boundary condition. Thus, the object is 'immersed' in a Cartesian grid. The Navier-Stokes equations are solved numerically by considering both the advection and the diffusion terms. At higher Reynolds numbers, effects of the advection (inertial) terms become important. Hence the influence of inertia on the micro-organism can be determined. Larger amplitudes of deformation for the micro-organism are also relatively easier to incorporate in the IBM, which is analytically difficult. This was also one of the reasons to choose a numerical implementation.

1.3. Objective

The objective of the thesis is to numerically study the effect of inertia on the model of a swimming micro-organism that is developed by B.U. Felderhof [Felderhof, 2015]. The results obtained from the numerical model will then be compared to that of the analytical solution to the model.

In order to achieve this, following sub-objectives were formulated.

- Develop a Fortran code using an Immersed boundary method (IBM) for simulating the deformable object.
- Validate the Fortran code for several test cases.
- Simulate the microswimmer and obtain the mean swimming velocity for different regimes, and compare it to the analytical solution to the model.

1.4. Outline

In **Chapter 2** a theoretical introduction to low Reynolds number flows is presented. The difference between the model used in this thesis for a swimming micro-organism and the model existing in literature is also discussed.
In **Chapter 3**, the numerical method is discussed. Details on the IBM that is used in this thesis are given.
In **Chapter 4**, several test cases for the code validation are presented and compared to those of a body conforming grid (FLUENT).
In **Chapter 5** the results obtained for the swimmer are discussed, followed by the conclusions in **Chapter 6**.

2

Theoretical Background

2.1. Fundamental Solutions to Stokes Flow

Microscopic organisms live in a regime dominated by viscous forces as explained in section 1.1. Hence, the inertial terms (LHS of eq 2.2) can be neglected from the Navier-Stokes equation (eq 2.2) leading to the Stokes equation (eq 2.3).

$$\nabla \cdot \vec{u} = 0 \tag{2.1}$$

$$\rho \frac{\partial \vec{u}}{\partial t} + \rho \vec{u} \cdot \nabla \vec{u} = -\nabla p + \mu \nabla^2 \vec{u} + \vec{f} \tag{2.2}$$

$$\nabla p = \mu \nabla^2 \vec{u} + \vec{f} \tag{2.3}$$

The Stokes equation (eq 2.3) is linear and independent of time. Hence, singular solutions can be found, and by superimposing these solutions, the flow induced by the swimming micro-organisms can be determined. This will be explained in the following sections.

The most basic of these solutions is the *Stokeslet*. It represents the flow field generated by a point force in an unbounded fluid. The flow field created by the Stokeslet is shown in Fig. 2.1a. The velocity ($\vec{u}$) and the pressure (p) fields at a point with position vector $\vec{r}$ due to the Stokeslet with a strength and a direction $\vec{\alpha}$ is given by the equations 2.4 and 2.5.

$$\vec{u} = \frac{\vec{\alpha}}{r} + \frac{(\vec{\alpha} \cdot \vec{r})\vec{r}}{r^3} \tag{2.4}$$

$$p = 2\mu \frac{\vec{\alpha} \cdot \vec{r}}{r^3} \tag{2.5}$$

where μ is the absolute viscosity of the fluid ($\frac{kg}{ms}$).

The Stokeslet is the lowest order singularity where the velocity fields die out the least slowly in the order $O(\frac{1}{r})$ as compared to higher order singularities. Higher order derivatives of the Stokeslet are also solutions to the Stokes equation. The stresslet (force dipole) is a higher order derivative of the Stokeslet and is shown in Fig. 2.1b. Physically, it is a pair of equal and opposite Stokeslets separated by a distance δd (not shown in the figure). The velocity fields induced by the stresslet decay as $O(\frac{1}{r^2})$. The stresslet can approximate the far-field flow (>7R, 'R' is the characteristic length scale of the organism) of a swimmer quite well [Drescher et al., 2011]. This is shown in Fig. 2.1d and 2.1e. Hence, the flow fields induced by the swimmers at a point far away are obtained by considering the swimmer as a force dipole. The bacteria *E.coli*, for instance, can be considered as a force dipole with its thrust coming from the rear and the drag acting on the front of the organism. This is shown in Fig. 2.2a. An organism such as *Chalmydomonas* which obtains its thrust from the front and the drag acting on the rear can be represented as a force dipole with an orientation opposite to that of *E.coli*, as shown in the Fig. 2.2b. Other examples of higher order singularities used to recreate the flow fields by the micro-organisms are the source dipole $O(\frac{1}{r^3})$ as shown in Fig. 2.1c, the force quadrupole $O(\frac{1}{r^4})$ and the force octupole $O(\frac{1}{r^8})$.

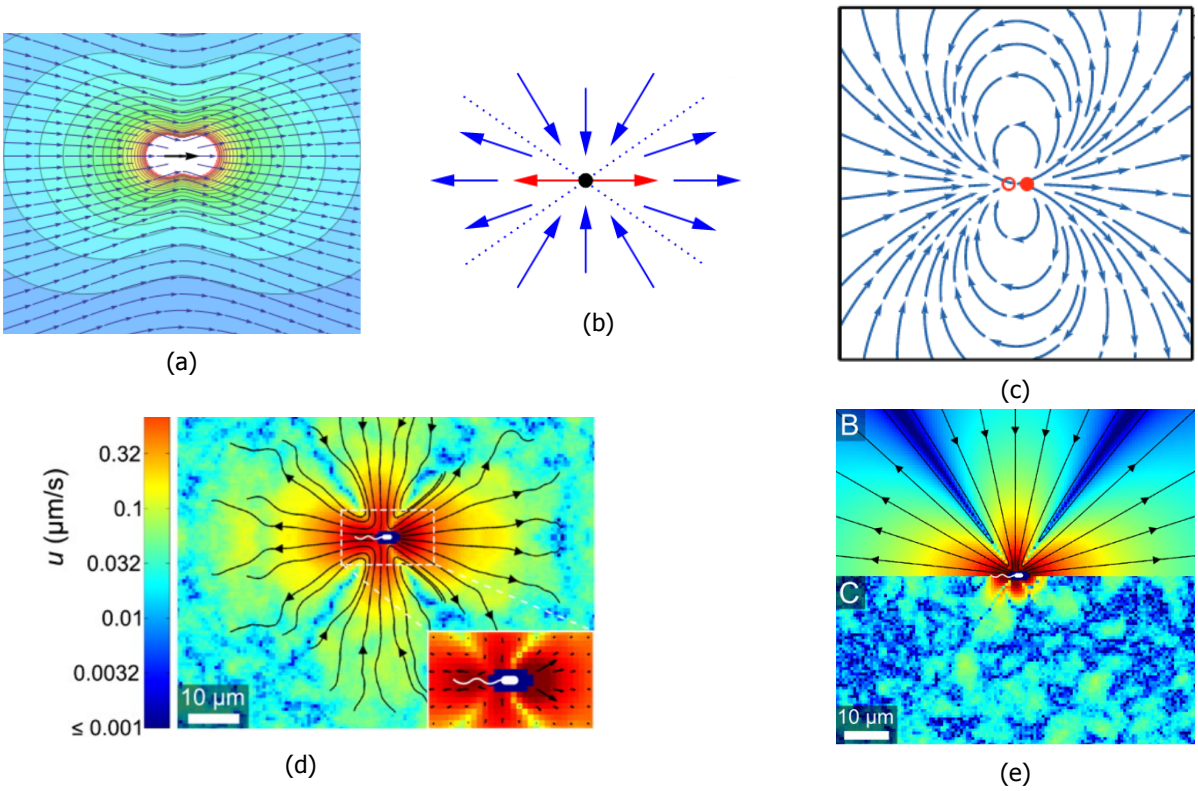

Figure 2.1: Flow fields created by the singular solutions to the Stokes equation. (a): Stokeslet, the flow field created by a point force (shown by the black arrow) in an unbounded fluid; (b): Stresslet (or the force dipole), a higher order singularity used to represent the flow field around swimming micro-organisms. It is obtained by placing two Stokeslets which are equal in magnitude (indicated by the red arrows) opposite to each other. Reproduced from [de Graaf and Stenhammar, 2017]; (c): Source dipole, a third order singularity constructed by placing a source (filled red circle) and a sink (hollow red circle) close to each other. Reproduced from [Zöttl and Stark, 2016]. (d): Experimental measurement of the average flow field around the bacteria *E.coli*; (e):*Top (B)* : flow fields obtained from the stresslet model that is fitted to the experimental measurements shown in panel *d* to the left; *bottom (C)* : flow field after removing the stresslet model from the experimental measurement on the same color scale as panel *d*. Differences can be seen only close to the body of the swimmer. Reproduced from [Drescher et al., 2011].

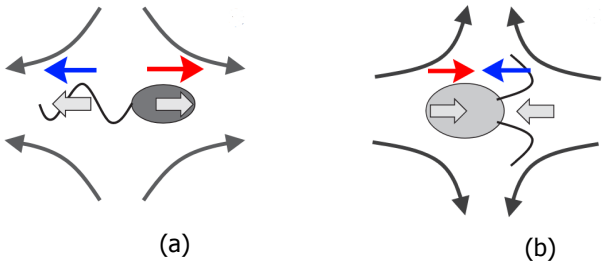

Figure 2.2: Swimming micro-organisms *E.coli* and *Chalmydomonas* represented by force dipoles. (a): In an organism such as *E.coli*, the thrust comes from the rear and its direction is indicated by the blue arrow. The drag acts on the front of the organism and its direction is indicated by the red arrow; (b) In *Chalmydomonas*, the thrust comes from the front and its direction is indicated by the blue arrow. The drag acts on the rear of the organism and its direction is indicated by the red arrow. Reproduced from [Ishikawa, 2009].

2.2. Steady Squirmer

The flow field induced by a ciliated micro-organism can also be represented in terms of Stokes-singularities. This will be explained in the later parts of the section. An introduction to the steady squirmer model in greater detail is provided in the first few paragraphs of this section.
As previously explained in section 1.1, a simple mathematical model (also known as the 'squirmer' model) to study ciliary propulsion was developed by Lighthill [Lighthill, 1952] and Blake [Blake, 1971]. In this approach, the cilia are considered to be very closely bundled so that no fluid can penetrate the surface formed when all the tips of the cilia are connected together. The region below this surface is ignored. Sub-layer models have also been developed by Blake [Blake, 1972] by considering the flow inside the cilia layer. However, this approach is not considered in this thesis.

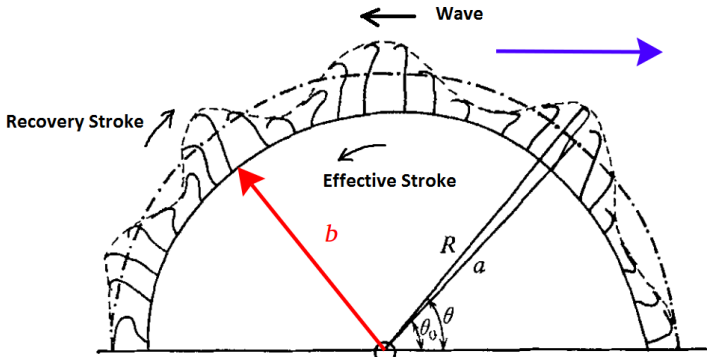

Figure 2.3: The envelope model developed by [Blake, 1971]. The sphere with radius *b* represents the surface of the micro-organism without the cilia. The surface with radius *R* represents the envelope. The sphere denoted with radius *a* denotes the mean surface of the envelope. The swimming direction is indicated by the blue arrow. Reproduced from [Blake, 1971].

In nature, a single cilium beats out of phase with its neighbouring cilia due to the hydrodynamic interactions between each other. This generates a wave-like pattern known as a Metachronal wave. When the Metachronal wave is along the direction of the effective stroke, it is called symplectic metachrony and the vice versa is called antiplectic metachrony. This is illustrated in the Appendix A.1. The no-slip and the no penetration boundary conditions on the envelope are valid only for the case of symplectic metachrony [Blake, 1971].

In the squrimer model, the mean shape of the swimmer is approximated as a sphere of radius *a*. In a frame of reference that moves with the sphere, the velocity fields are found as a set of fundamental solutions to the Stokes equation. They are expressed in a spherical coordinate system where *r* denotes the radial distance and θ denotes the polar angle. The velocity fields are obtained under the assumption of axial symmetry. At the surface of the swimmer ($r = a$), the velocity fields are given by equations 2.6 and 2.7. Here $P_n(cos\theta)$ and $P_n'(cos\theta)$ denote the Legendre polynomials and their first derivatives respectively.

$$u_r|_{r=a} = \sum_{n=0}^{\infty} A_n(t) P_n(\cos\theta) \tag{2.6}$$

$$u_\theta|_{r=a} = \sum_{n=1}^{\infty} B_n(t) \frac{2\sin\theta}{n(n+1)} P_n'(\cos\theta) \tag{2.7}$$

Equations 2.6 and 2.7 are simplified by assuming that the radial velocity at the surface of the swimmer vanishes and the tangential velocities at the surface of the swimmer are time independent. In addition to this, only the first two terms of the equation 2.7 are retained. Hence, the tangential velocity of the swimmer is derived as shown in equation 2.8. This is known as the steady squrimer model or the B1-B2 model [Ishikawa and Pedley, 2007].

$$u_\theta|_{r=a} = \frac{B_1}{3} \cdot \sin\theta + B_2 \cdot \sin\theta\cos\theta \tag{2.8}$$

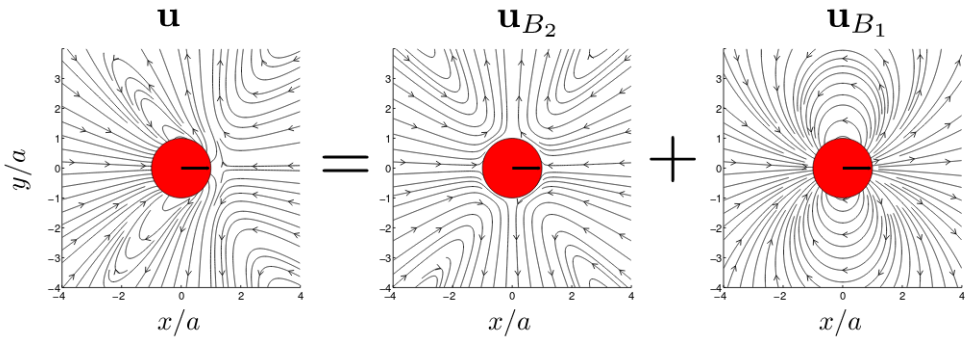

Figure 2.4: Flow field ($\mathbf{u}$) around a squirmer in the laboratory frame of reference constructed from the singularity solutions of Stokes flow. $\mathbf{u_{B1}}$ represents the contribution from the source dipole and $\mathbf{u_{B2}}$ represents the contribution from the stresslet. Reproduced from [Delmotte et al., 2015].

As seen in Fig. 2.4, the flow field around a squirmer can be represented as a combination of the flow fields from two singularity solutions, the source dipole and the stresslet. The terms B_1 and B_2 in equation 2.8 relate to the strength of the source dipole and the strength of the stresslet respectively. Only the first term in the equation 2.8 determines the swimming velocity of the squirmer which is given by $\frac{2B_1}{3}$. This is derived from the condition that the squirmer is force-free and is irrespective of the size of the particle [Molina et al., 2013]. The Stokeslet does not contribute to the far field because the swimmer is force free.

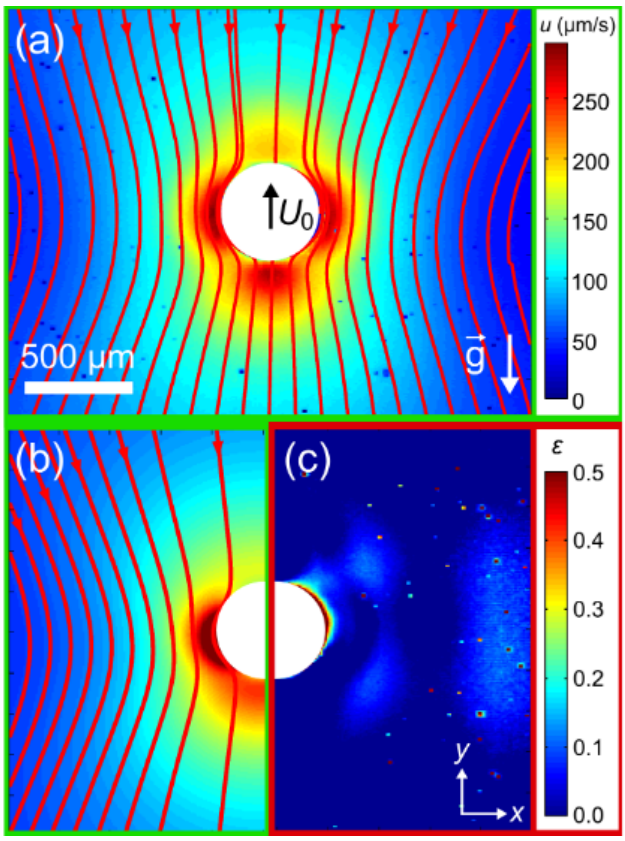

Figure 2.5: Flow field around *Volvox* in the laboratory frame of reference. (a): The experimentally measured flow field ; (b): The fitted flow field with the contribution from the Stokeslet with the same color scale as panel *a* ; (c): The relative error ε is defined as $\frac{|u_{exp}-u_{fit}|}{|u_{exp}|}$ between the experimental flow field in panel *a* and the fitted model in panel *b*. $\vec{g}$ denotes gravity. The swimming direction is indicated by the black arrow. Reproduced from [Drescher et al., 2010].

The experimental measurements of Drescher [Drescher et al., 2010] on the spherically ciliated alga *Volvox*, indicate that there is strong contribution from the Stokeslet to the flow field, despite the minute density difference between the fluid and the alga ($\frac{\rho_{volvox}-\rho_{fluid}}{\rho_{fluid}} \approx 0.3\%$) as shown in panels *a,b,c* in the Fig. 2.5. The differences between the experiments and the fitted model are restricted to a narrow region close to the swimmer as shown by panel *c* in Fig. 2.5. The source dipole dominates in the near field as shown by Fig. 2.6. This is observed after removing the Stokeslet contribution. The contribution of the stresslet is small, causing an asymmetrical velocity profile between the front and the rear portion of the organism, as shown in Fig. 2.6.

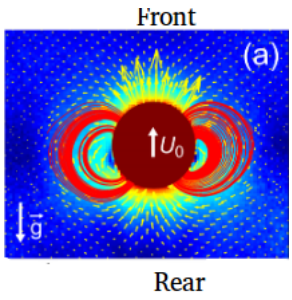

Figure 2.6: The contours of the experimentally measured velocity fields near *Volvox* obtained after subtracting the contribution from the Stokeslet. The source dipole dominates the flow field. The swimming direction is indicted by the white arrow. $\vec{g}$ is gravity. Reproduced from [Drescher et al., 2010].

2.3. Pushers,Pullers and Neutral Squirmers

The ratio, $\beta = \frac{B_2}{B_1}$ is a typical characteristic of a swimmer. When $\beta > 0$, the swimmer is known as a puller, while $\beta < 0$ represents a pusher and $\beta = 0$ represents a neutral swimmer. The flow field around a pusher, a puller and a neutral squirmer in the laboratory frame of reference and in a frame of reference that moves with the squirmer is shown in Fig. 2.7.

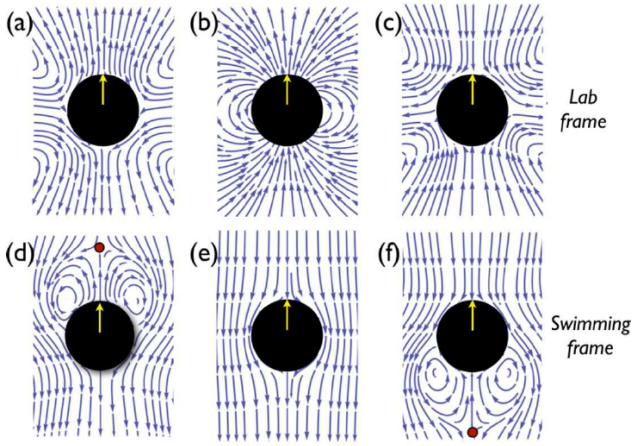

Figure 2.7: Flow fields around various types of squirmers. The flow fields around a pusher ($\beta = -5$) in a laboratory frame and in a moving frame of reference are given in panels *a* and *d* respectively, while those of a puller ($\beta = +5$) in a laboratory frame and in a moving frame of reference are given in panels *c* and *f* respectively. The flow fields around a neutral squirmer ($\beta = 0$) in a laboratory frame and in a moving frame of reference are given in panels *b* and *e* respectively. The red dot indicates the stagnation point in the flow field. The arrow in yellow indicates the direction of swimming. Reproduced from [Evans et al., 2011].

As shown by Fig. 2.7, there exist regions of re-circulation behind a puller and in front of a pusher in a moving frame of reference. The flows in the far-field induced by the swimming micro-organisms

such as *E.coli* and *Chlamydomonas* can be studied by considering them as either pushers or pullers. A pusher such as *E.coli* draws the fluid surrounding it, from its sides and pushes the fluid along its length as shown by the panel *a* in Fig. 2.8. A puller such as *Chlamydomonas* does the opposite by pulling the fluid along its length and expelling it sideways as shown by the panel *b* in Fig. 2.8. Hence, the flow fields induced by pushers or pullers can be either extensile or contractile as shown by the panels *c* and *d* in Fig. 2.8 respectively [Dunkel et al., 2010].

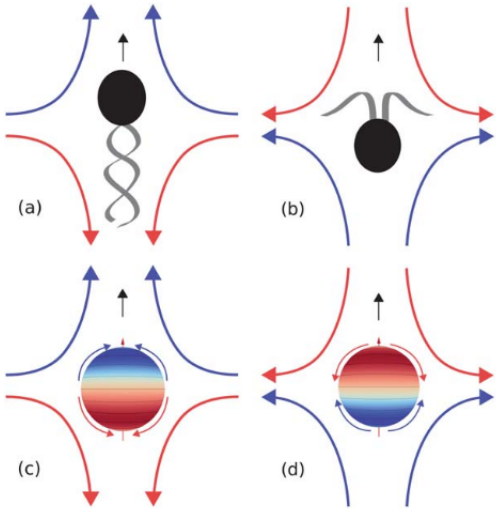

Figure 2.8: Flow fields induced by pushers and pullers. (a) and (c): The pusher *E.coli* shown in black, inducing an extensile flow field (shown by panel *c*). (b) and (d): The puller *Chlamydomonas* shown in black inducing a contractile flow field (shown by panel *d*). Reproduced from [Molina et al., 2013].

2.4. Inertial Effects on a Squirmer

Wang and Ardekani [Wang and Ardekani, 2012a] investigated the effects of inertia on pullers and pushers for the Reynolds numbers ranging from 10^{-3} to 10^{0} for different values of β. The velocity scale for the Reynolds number is the strength of the stresslet B_2. They find that inertia increases the swimming speed of the pusher by 60%, while it reduces the swimming speed of a puller. As discussed in section 2.3, there is a region of closed streamlines formed in front of a pusher, while this region is formed at the back of a puller.

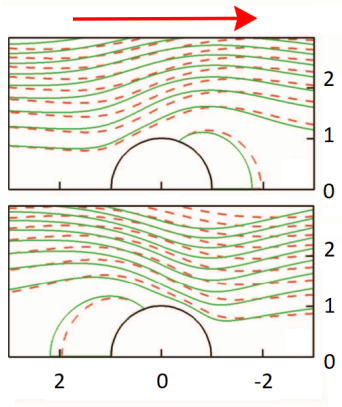

Figure 2.9: Streamlines for a pusher (*top*) and a puller (*bottom*) in a co-moving frame of reference respectively. The dashed red lines indicate the streamlines at *Re*=0, and the continuous green lines indicate the streamlines at *Re*=1. The swimming direction is denoted by the red arrow. The *Z* and *X* (not shown in the figure) axes point in the horizontal and vertical direction respectively. Reproduced from [Wang and Ardekani, 2012a].

As seen in Fig. 2.9, inertia shortens the region of re-circulation for a pusher and enlarges the region of re-circulation for a puller hence reducing the swimming speed of the puller and increasing the speed of the pusher.

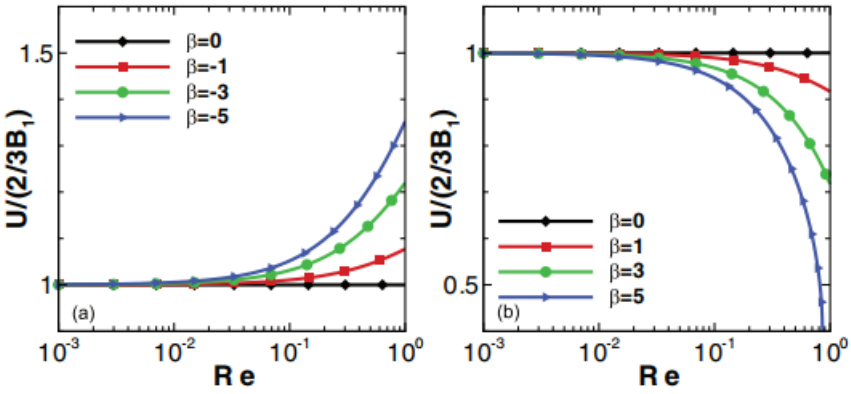

Figure 2.10: The non-dimensionalized swimming velocity for a pusher and puller at different values of β. The swimming velocity is non-dimensionalized by the velocity that is predicted by the B1-B2 model ($\frac{2B_1}{3}$). The Reynolds number is plotted along the horizontal axis and the non-dimensional swimming velocity is plotted along the vertical axis. Reproduced from [Wang and Ardekani, 2012a].

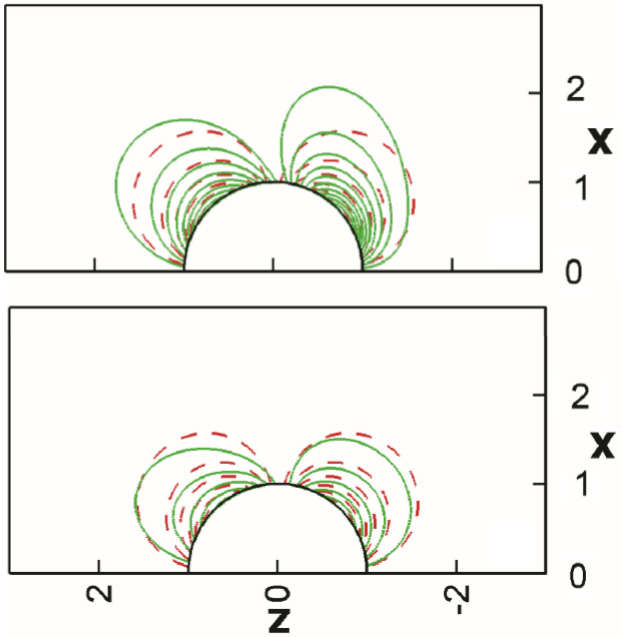

Figure 2.11: Non-dimensionalized contours of the vorticity for a puller (*top*) and puller (*bottom*). The solid green lines denote the contours at *Re*=1, and the dashed red lines denote the contours at *Re*=0. Reproduced from [Wang and Ardekani, 2012a].

The effects of inertia are more pronounced at higher values of β at higher Reynolds numbers. This is shown by Fig. 2.10. The vorticity generated at the surface of the organism is larger due to inertial effects in a puller and is diminished by inertial effects in a pusher. This enhances in mixing the fluid for a puller, while diminishing the mixing in a pusher. This is shown in Fig. 2.11.

2.5. Unsteady Squirmer

Wang and Ardekani [Wang and Ardekani, 2012b] consider the effects of the virtual mass force and the Basset force in addition to the Stokes drag that arise when a squirmer is accelerating, on the swimming velocity of the organism. They find that the effects of the virtual mass force and the Basset forces are negligible when $StRe << 1$, where St is the Strouhal number given by $\frac{fL}{U}$ and Re is the Reynolds number given by $\frac{UL}{\nu}$, where f, L, U, ν denote the charecteristic frequency of the beat, the swimming velocity of the organism, the length scale of the organism and the dynamic viscocity of the fluid respectively. The Strouhal number is the ratio of the time scale of the unsteady inertia that is generated by the surface distortions of the organism to the time scale of the convective inertia of the organism. The Reynolds number is the ratio of the convective inertial force on the organism which scales as $\rho\frac{U^2}{L}$ to the viscous force on the organism which scales as $\mu\frac{V}{L}$. The effects of the Basset force and the added mass forces become important at $StRe >> 1$.

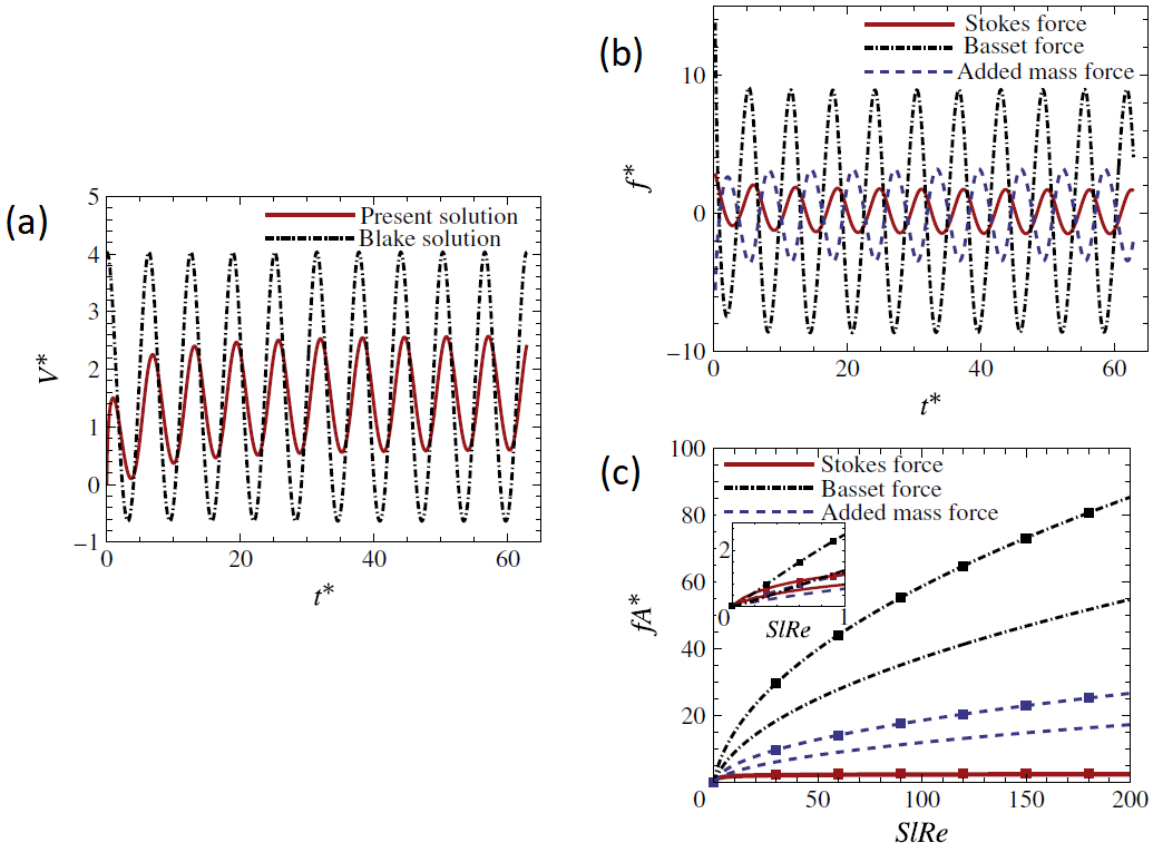

Figure 2.12: Swimming velocity and the forces on an unsteady squirmer. (a): The non-dimensionalized swimming velocity (V^*) as a function of the non-dimensional time (t^*) obtained by considering the effects of the basset and the added mass forces (shown in red) and without considering their effects (shown in black). (b): The non-dimensional Stokes drag (shown in red), Basset force (shown in black) and the added mass force (shown in blue) as a function of the non-dimensional time ($t*$). (c): The amplitude (fA^*) of the Basset force , the added mass force and the Stokes drag as a function of the non-dimensional time ($t*$). Reproduced from Wang and Ardekani [2012b].

As shown in panel *b* Fig. 2.12 the magnitude of the basset force and the added mass force is much larger than the Stokes drag acting on the squirmer. The mean swimming velocity as predicted by them considering the added mass force and the Basset force differs from the solution by Blake which does not consider the two forces. The effects of these two forces is more pronounced at $StRe \sim O(1)$ as shown in panel *c* in Fig. 2.12.

2.6. Effects of a Distorting Sphere

The B1-B2 model derives a flow pattern u_θ by assuming a slip velocity on the mean surface of the envelope. Instead of deriving the flow pattern from the assumptions made on the envelope, B.U. Felderhof [Felderhof, 2015] prescribes the deformations of a sphere with radius *a* and calculates the swimming velocities induced from the deformations of the sphere to the second order in the perturbations of the sphere ($\vec{\xi}$). The swimming velocities are derived in a laboratory frame of reference where the fluid is at rest at infinity. The deformations of the sphere prescribed analytically by him are used in the present work. Their details are described below.

A spherical coordinate system is used where $\vec{s}$ (r,θ,ϕ) denotes a point on the sphere, with radial distance r, azimuthal angle θ and polar angle ϕ. The perturbation $\vec{\xi}$ of the sphere is axisymmetric and is given by equation 2.9, where $\vec{u_i}$ and $\vec{v_i}$ as described by equations 2.10 & 2.11, are functions of the Legendre polynomials ($P_i(cos\theta)$) and their derivatives ($P_i^1(cos\theta)$) respectively. $M_i(t)$ & $K_i(t)$ are periodic functions of time *t* given by equations 2.12 and 2.13. ω is the characteristic frequency of the deformation.

$$\vec{\xi}(\vec{s},t) = \sum_{i=1}^{\infty} M_i(t)\vec{u_i}(a,\theta) + \sum_{i=2}^{\infty} K_i(t)\vec{v_i}(a,\theta) \tag{2.9}$$

$$\vec{u_i}(r,\theta) = (\frac{a}{r})^{i+2}[(i+1)P_i(cos\theta)\vec{e_r} + P_i^1(cos\theta)\vec{e_\theta}] \tag{2.10}$$

$$\vec{v_i}(r,\theta) = (\frac{a}{r})^{i}[(i+1)P_i(cos\theta)\vec{e_r} + \frac{i-2}{i}P_i^1(cos\theta)\vec{e_\theta}] \tag{2.11}$$

$$M_i(t) = a(\mu_{is}cos\omega t - \mu_{ic}sin\omega t) \tag{2.12}$$

$$K_i(t) = a(\kappa_{is}cos\omega t - \kappa_{ic}sin\omega t) \tag{2.13}$$

The first three terms i.e i =1,2,3 are considered in the expansion of $\vec{\xi}$ (eq 2.14) to prescribe the deformation of the sphere.

$$\vec{\xi}(\vec{s},t) = \sum_{i=1}^{3} M_i(t)\vec{u_i}(a,\theta) + \sum_{i=2}^{3} K_i(t)\vec{v_i}(a,\theta) \tag{2.14}$$

The expansions for $\vec{u_1}(r,\theta), \vec{u_2}(r,\theta), \vec{v_1}(r,\theta), \vec{v_2}(r,\theta)$ used by [Felderhof, 2015] are given by equations 2.15-2.18.

$$\vec{u_1}(r,\theta) = (\frac{a}{r})^3[2cos\theta\vec{e_r} + sin\theta\vec{e_\theta}] \tag{2.15}$$

$$\vec{u_2}(r,\theta) = (\frac{3a^4}{4r^4})[(1+3cos2\theta)\vec{e_r} + 2sin2\theta\vec{e_\theta}] \tag{2.16}$$

$$\vec{v_1}(r,\theta) = (\frac{a}{r})[2cos\theta\vec{e_r} - sin\theta\vec{e_\theta}] \tag{2.17}$$

$$\vec{v_2}(r,\theta) = (\frac{3a^2}{4r^2})[(1+3cos2\theta)\vec{e_\theta}] \tag{2.18}$$

The set of coefficients $\mu_{1c},\mu_{1s},\mu_{2c},\mu_{2s},\mu_{3c},\mu_{3s}$ and $\kappa_{1c},\kappa_{1s},\kappa_{2c},\kappa_{2s},\kappa_{3c},\kappa_{3s}$ as shown in the RHS of equations 2.12 and 2.13 characterize the type of deformation ($\vec{\xi}$) of the sphere. A different combination of the coefficients leads to a different swimmer with a distinct deformation. The combined-stroke - swimmer, the squriming swimmer and the potential swimmer as described by [Felderhof, 2015] are shown in Fig. 2.13 , 2.14 and 2.15 respectively. They are obtained by using different combinations of the coefficients.

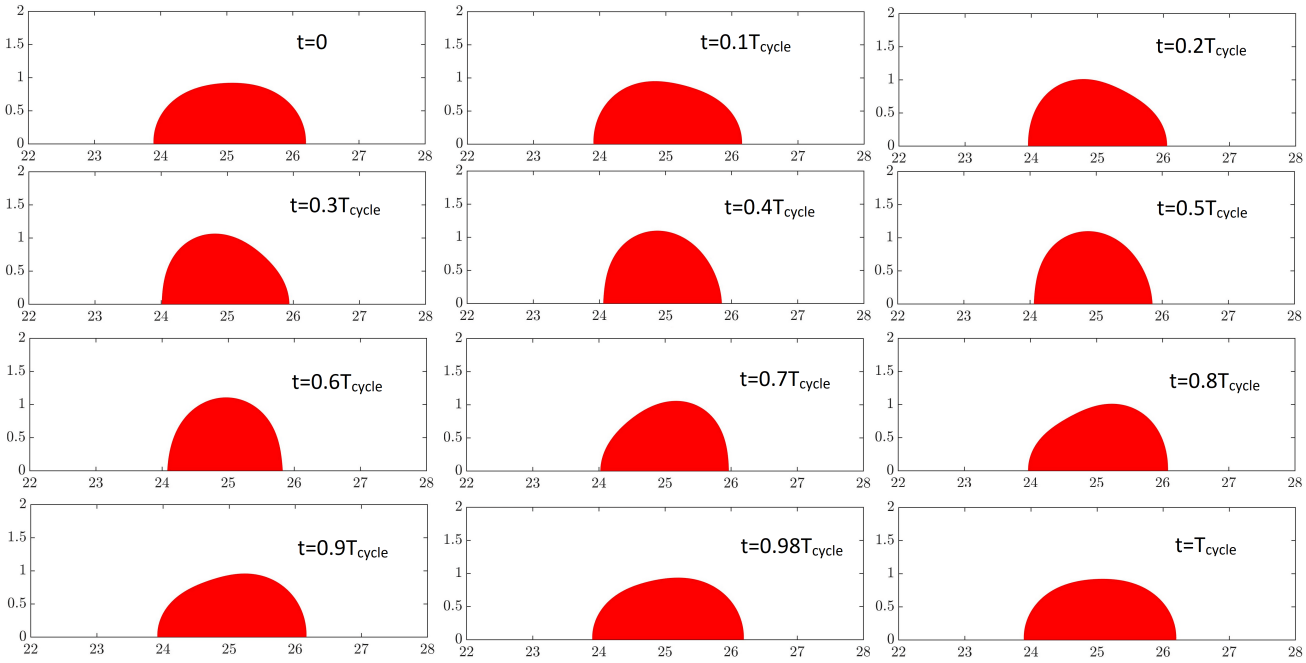

Figure 2.13: Deformations (one-half) of the combined-stroke-swimmer ($\mu_{1c} = 0.05, \kappa_{3c} = -0.022, \kappa_{2s} = 0.0621$) as shown in red. The sequence is to be read clockwise from top-left. T_{cycle} in the frames denotes the cycle time of the swimmer. The Z and R axes (not shown in the figure) are in the horizontal and the vertical direction respectively.

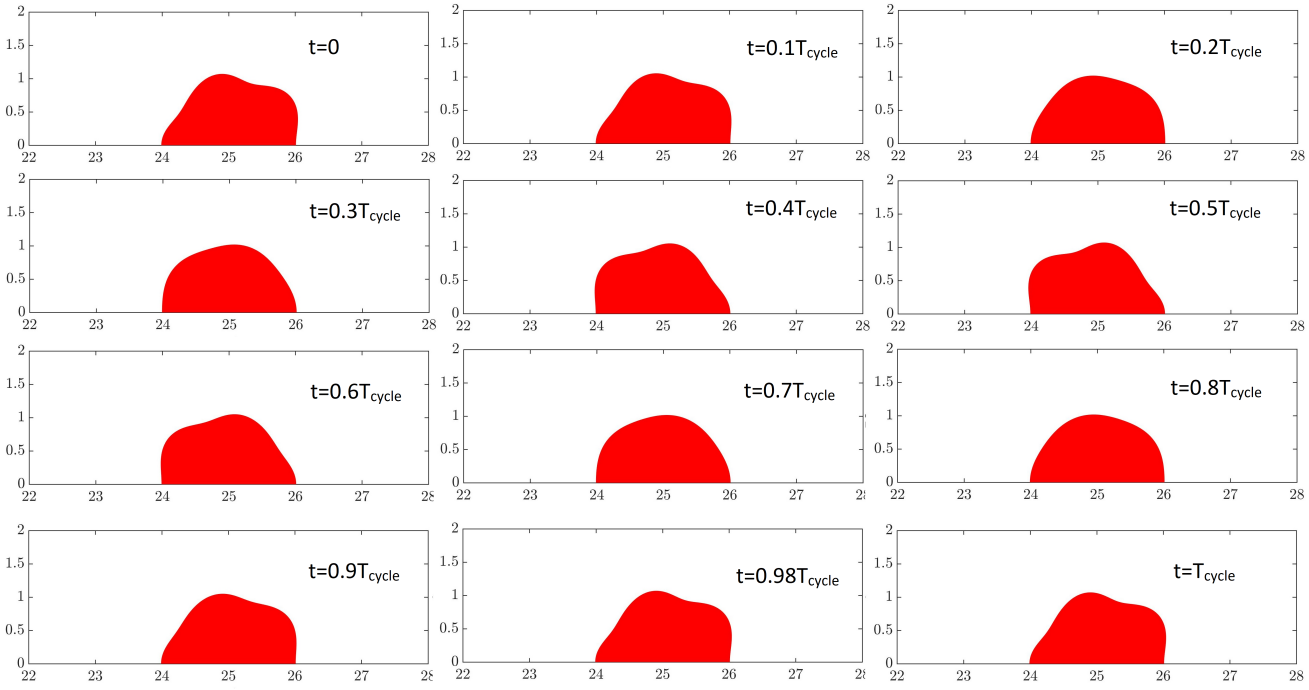

Figure 2.14: Deformations (one-half) of the squirming swimmer ($\mu_{2c} = 0.05, \mu_{3s} = 0.053, \kappa_{2c} = -0.05, \kappa_{3s} = -0.053$) as shown in red. The sequence is to be read clockwise from top-left. T_{cycle} in the frames denotes the cycle time of the swimmer. The Z and R axes (not shown in the figure) are in the horizontal and the vertical direction respectively.

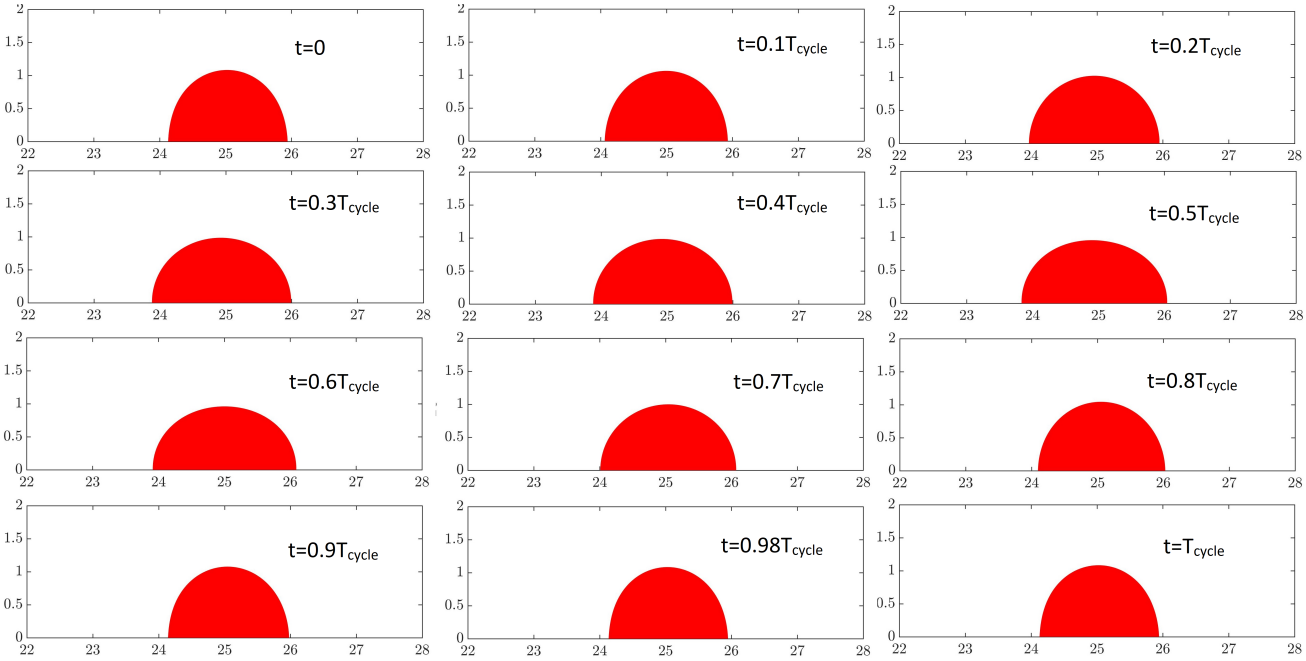

Figure 2.15: Deformations (one-half) of the potential swimmer ($\mu_{1c} = 0.025, \mu_{2s} = 0.038, \kappa_{2s} = -0.0471$) as shown in red. The sequence is to be read clockwise from top-left. T_{cycle} in the frames denotes the cycle time of the swimmer. The Z and R axes (not shown in the figure) are in the horizontal and the vertical direction respectively.

The following dimensionless numbers are of use to analyze the effects of inertia on the combined-stroke -swimmer.

Scale Number

The scale number as defined by [Felderhof, 2015], is a measure of inertia generated by the surface of the distorting sphere. It is given by equation 2.19 where ω is the characteristic frequency of the distortion, *a* is the radius of the sphere, and ν is the kinematic viscosity of the fluid in which the sphere is swimming.

$$s = a(\frac{\omega}{2\nu})^{\frac{1}{2}} \tag{2.19}$$

Unsteady Reynolds Number

The unsteady Reynolds number characterizes the ratio of the unsteady inertial forces to viscous forces. It is given by equation 2.20 where ω ($\frac{2\pi}{T_{cycle}}$) is the characteristic frequency of the organism, *L* is the length scale of the organism and ν is the kinematic viscosity of the fluid in which it swims.

$$Re_{\omega} = \frac{\omega L^2}{\nu} \tag{2.20}$$

Reynolds Number

The Reynolds number characterizes the ratio of inertial forces to viscous forces. It is given by equation 2.21 where *U* is the characteristic velocity of the organism, *L* is the characteristic length scale of the organism, and ν is the kinematic viscosity of the fluid in which it swims.

$$Re = \frac{UL}{\nu} \tag{2.21}$$

The swimming velocity to the second order in the deformation ($\vec{\xi}$) obtained by B.U. Felderhof [Felderhof, 2015] for the combined-stoke-swimmer for $\mu_{1c} = 0.05$ is shown in the Fig. 2.16. At large scale numbers (s > 3) where inertial effects become important, the swimming velocity decreases in

magnitude and changes in sign, leading to a change in the direction of swimming sphere. The mean swimming velocity as a function of the scale number as obtained by the analytical solution as shown in Fig. 2.16 will be compared to the numerical solution obtained in this thesis.

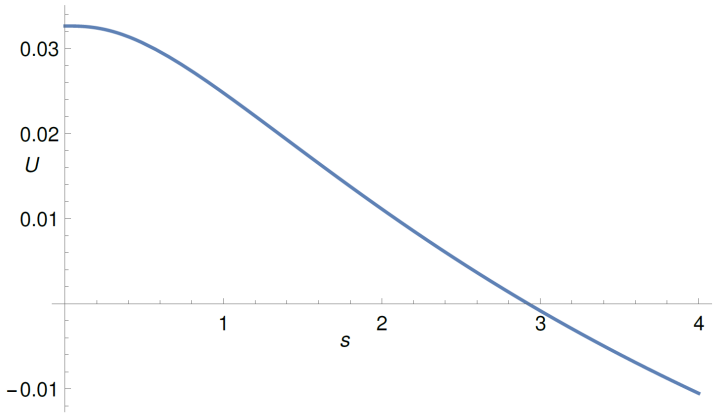

Figure 2.16: Swimming velocity ($\frac{m}{s}$) as a function of the logarithm of the scale number (s) for the combined-stroke-swimmer with the coefficients $\mu_{1c} = 0.05, \kappa_{3c} = -0.022, \kappa_{2s} = 0.0621$. Reproduced from [Felderhof, 2015].

The swimming velocity also depends on the values of the coefficients that are chosen. The non-dimensional swimming velocity (second order in the deformation $\vec{\xi}$) for $\mu_{1c} = 1.0$ as obtained by [Felderhof, 2015] for a large range of scale numbers ($s > 100$) is shown in the Fig. 2.17. In a recent publication, [Felderhof and Jones, 2017] find the optimal efficiency of the swimmer at asymptotically large scale number.

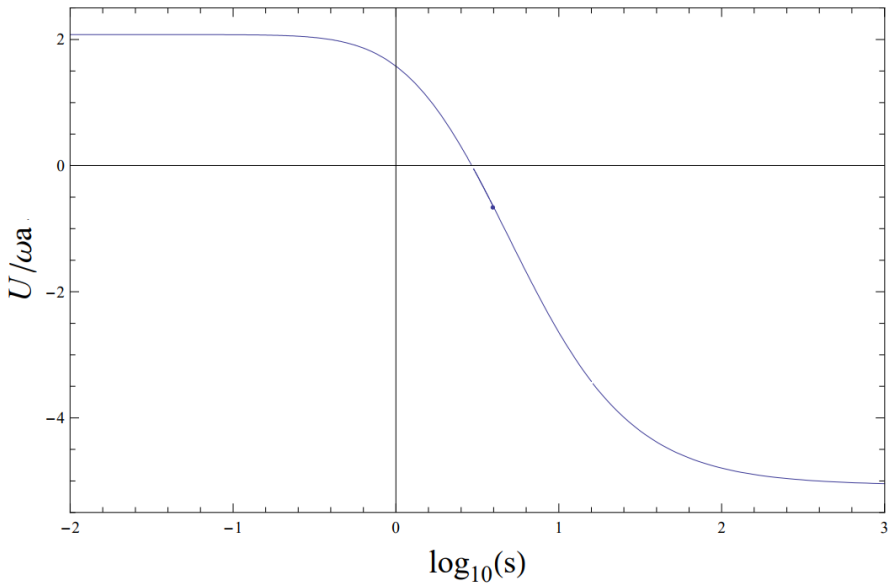

Figure 2.17: Non-dimensional swimming velocity ($\frac{U}{\omega a}$) as a function of the logarithm of the scale number (s) for the combined-stroke-swimmer with $\mu_{1c} = 1.0$. Reproduced from [Felderhof, 2015].

3

Numerical Method

In this chapter, details on the numerical method are described. The grid used and the Volume Penalization/Volume of Solid scheme adapted to this work are described in the following sections.

3.1. Staggered Grid

In Fig. 3.1, the X and Y axes point in the streamwise direction and the normal direction respectively. The velocity components along the streamwise direction and the normal direction are U and V are shown by the blue and green arrows respectively. The U and V velocities are stored at the cell faces, while the pressure is stored at the cell centres as shown by the red dots in the figure. A staggered grid is used to avoid the pressure and the velocity getting decoupled [Versteeg and Malalasekera, 2007].

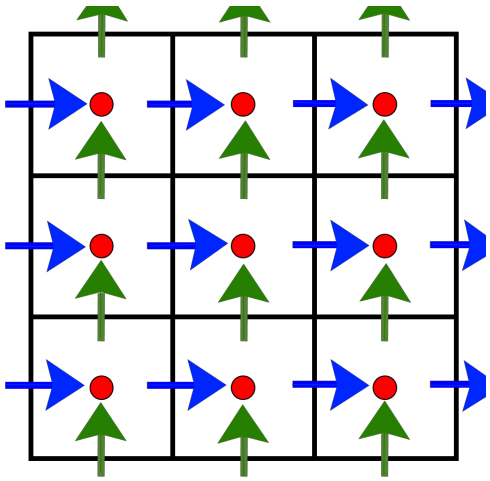

Figure 3.1: The staggered grid used in the present work used to simulate the fluid flow. The blue arrows represent the U velocities in the streamwise direction and the green arrows represent the V velocities in the normal direction respectively. The red dots represent the pressure points. Reproduced from [Niazi Ardekani et al., 2018].

3.2. Discretization of the Navier Stokes Equations

The code uses the finite volume scheme. Hence the Navier-Stokes equations (eq 3.1) are integrated over a control volume.

$$\rho \frac{\partial \vec{u}}{\partial t} + \rho \vec{u} \cdot \nabla \vec{u} = -\nabla p + \mu(\nabla^2 \vec{u}) + \vec{f} \tag{3.1}$$

Using Gauss divergence theorem, the integrals for momentum and diffusion are converted to surface integrals. They are then evaluated over the surface of a grid cell as shown by equation 3.2.

$$\int_V \rho \frac{\partial \vec{u}}{\partial t} dV + \int_V \nabla \cdot (\rho \vec{u} \vec{u}) dV = \int_V -\nabla p dV + \int_V \mu \nabla^2 \vec{u} dV + \int_V \vec{f} dV \tag{3.2}$$

3.3. Fractional Step Methods

Integration of equation 3.2 in time, is done in parts. In the first part, an intermediate velocity ($\mathbf{u}^*$) is obtained from a guessed value for the pressure field ($p^{n-1/2}$) as done in equation 3.3. The symbols $\mathbf{A^n}$ and $\mathbf{D^n}$ denote the advection and the diffusion terms at the old time levels respectively, Δt indicates the time-step and ν indicates the kinematic viscosity of the fluid. This intermediate velocity ($\mathbf{u}^*$) is not divergence free. In order to correct this, a pressure that corresponds to an intermediate divergence free velocity field is obtained (eq 3.4) and the intermediate velocities are corrected to obtain the velocities at the next time-step (eq 3.5). The guessed value of pressure ($p^{n-1/2}$) is also corrected to obtain the pressure at the new time level (eq 3.6).

$$\frac{\mathbf{u}^* - \mathbf{u^n}}{\Delta t} = -(\nabla p^{n-1/2} - \mathbf{A^n} + \nu \mathbf{D^n}) \tag{3.3}$$

$$\nabla^2 \tilde{p} - \frac{1}{\Delta t} \nabla \cdot \mathbf{u}^* = 0 \tag{3.4}$$

$$\mathbf{u^{n+1}} = \mathbf{u}^* - \Delta t \nabla \tilde{p} \tag{3.5}$$

$$p^{n+1/2} = p^{n-1/2} + \tilde{p} \tag{3.6}$$

In an Immersed boundary method, equations 3.3-3.6 are modified to account for the presence of an obstacle in the domain. The intermediate velocity computed from eq 3.3 is modified by a forcing term ($f^{n+1/2}$) into a second intermediate velocity ($\mathbf{u}^{**}$) at the location of the obstacle (eq 3.8). The velocities at the new time level are obtained from the pressure (eq 3.10). The scheme is given by equations 3.7-3.11. This is known as a fully explicit scheme.

$$\frac{\mathbf{u}^* - \mathbf{u^n}}{\Delta t} = -(\nabla p^{n-1/2} - \mathbf{A^n} + \nu \mathbf{D^n}) \tag{3.7}$$

$$\mathbf{u}^{**} = \mathbf{u}^* + \Delta t f^{n+1/2} \tag{3.8}$$

$$\nabla^2 \tilde{p} - \frac{1}{\Delta t} \nabla \cdot \mathbf{u}^{**} = 0 \tag{3.9}$$

$$\mathbf{u^{n+1}} = \mathbf{u}^{**} - \Delta t (\nabla \tilde{p}) \tag{3.10}$$

$$p^{n+1/2} = p^{n-1/2} + \tilde{p} \tag{3.11}$$

3.4. Restrictions on the time-step

A fully explicit scheme given by equations 3.7 -3.11 has one major disadvantage. It does not allow for large time-steps. The diffusion and the Courant criteria for restrictions on the time step for the fully explicit scheme are given by equation 3.12 and equation 3.13 respectively. The diffusion criteria is more restrictive as compared to the Courant criteria. The time-step 'Δt' for the diffusion criteria is proportional to the square of the grid spacing ($\Delta x, \Delta y$) while the Courant criteria (eq 3.13) is less restrictive with 'Δt' varying linearly as the grid spacing. Hence, extremely small time steps are required to solve the equations 3.7-3.11. This restriction on the time-step can be overcome by using an implicit scheme for the diffusion term. Hence, for regimes which are highly viscous, an implicit treatment of the diffusion terms is preferred.

$$\frac{\nu \Delta t}{dx^2} + \frac{\nu \Delta t}{dy^2} \leq 0.5 \tag{3.12}$$

and,

$$\frac{U \Delta t}{dx} + \frac{V \Delta t}{dy} \leq C_{max} \tag{3.13}$$

3.5. Implicit Scheme

In order to overcome the restrictions posed by the fully explicit scheme as mentioned in section 3.4, an implicit integration for the diffusion is used in this work. This scheme is given by equations 3.14-3.18. A Crank-Nicholson scheme is used for the implicit integration of the diffusion terms, while the advection terms are integrated through a 2^{nd} order Adams-Bashforth scheme, which consists of using the advection terms from the current and the old time level respectively ($\mathbf{A^n}, \mathbf{A^{n-1}}$). In addition to this, extra terms to the pressure correction equation (eq 3.18) are added due to the diffusion terms being implicitly solved.

$$\frac{\mathbf{u}^* - \mathbf{u}^\mathbf{n}}{\Delta t} = \frac{\nu}{2}\nabla^2(\mathbf{u}^\mathbf{n} + \mathbf{u}^*) - \nabla p^{n-1/2} - (\frac{3}{2}\mathbf{A}^\mathbf{n} - \frac{1}{2}\mathbf{A}^{\mathbf{n-1}}) \tag{3.14}$$

$$\mathbf{u}^{**} = \mathbf{u}^* + \Delta t f^{n+1/2} \tag{3.15}$$

$$\nabla^2\tilde{p} = \frac{1}{\Delta t}\nabla \cdot \mathbf{u}^{**} \tag{3.16}$$

$$\mathbf{u}^{\mathbf{n+1}} = \mathbf{u}^{**} - \Delta t\nabla\tilde{p} \tag{3.17}$$

$$p^{n+1/2} = p^{n-1/2} + \tilde{p} - \frac{\nu}{2}\nabla^2\tilde{p} \tag{3.18}$$

3.6. Volume Penalization IBM/ Volume of Solid IBM

The distinction between various Immersed boundary methods is in the way they compute the forcing term ($f^{n+1/2}$). In this thesis, the Volume penalization IBM of Kajishima [Kajishima et al., 2001] has been implemented. The forcing term in this IBM is computed from the mass/volume fractions (α) occupied by the immersed object in a cell (eq 3.19) where n denotes the time level.

$$f^{n+1/2} = \alpha^{n+1}(\frac{U_{solid}^{n+1} - u^*}{\Delta t}) \tag{3.19}$$

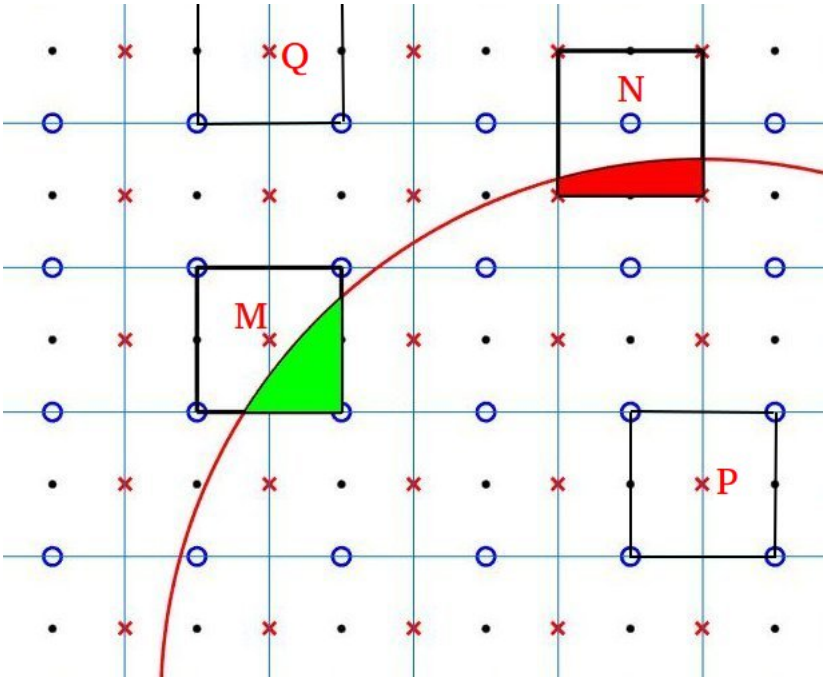

Figure 3.2: Mass/Volume fractions (shown by the areas colored in green and red) occupied by the immersed boundary (shown by the red line) for the partially filled cells centered at points 'M' and 'N'. Crosses (x's) and circles (o's) represent the points where the U and V velocities are computed respectively. Black dots represent the points where the pressure is computed. 'P' and 'Q' represent the centres of the cells which are fully inside and outside the immersed object respectively.

As shown in Fig. 3.2, the volume fractions which are shown in green and red colors are used to compute the forcing term (eq 3.19). For the cell with centre Q which lies completely outside the immersed solid, the volume fraction (α) is 0. For the cell with centre P which lies completely inside the immersed solid, the volume fraction (α) is 1.

On the basis of their location, there are two methods to evaluate the volume fractions. In the first method, the cells are centered around the velocity points as shown in Fig. 3.3a. Hence the volume fractions are computed directly at the velocity points. In the second method, the cells are centred around the pressure points as shown in Fig. 3.3b. Here, the mass fractions are computed at the pressure points and need to be linearly interpolated to the velocity points thereby losing accuracy. This also diffuses the interface over a grid cell, which is important for a moving/deforming obstacle. In this thesis, the first method is used for accuracy.

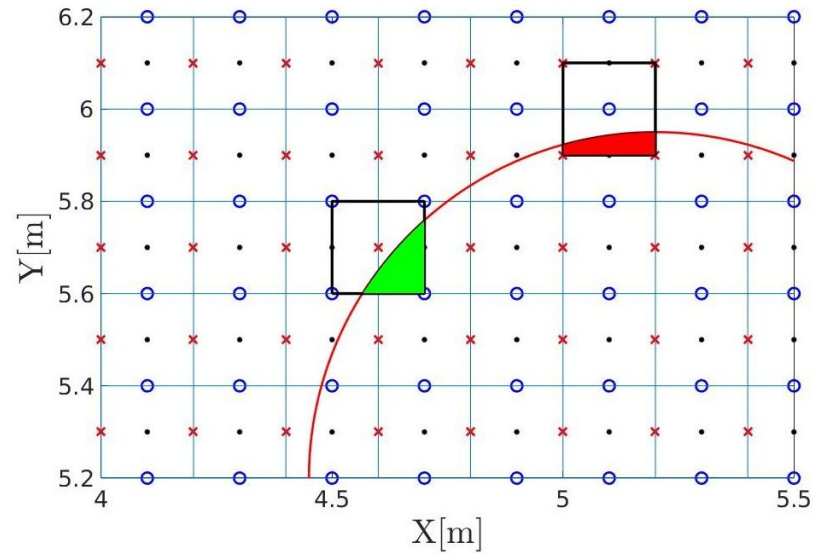

(a)

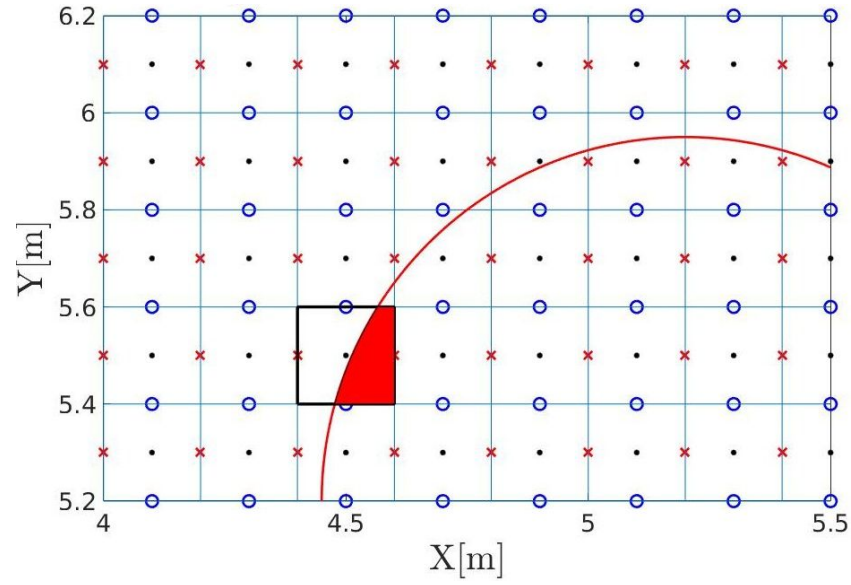

(b)

Figure 3.3: Locations at which the mass/volume fractions are evaluated. (a): The mass fractions (shown by the areas colored in green and red) are evaluated at the U and V velocity points denoted by x's and o's respectively. (b): The mass fractions (shown by the area colored in red) are computed at the pressure points as shown by the black dots and interpolated to the velocity points.

3.7. Methods for computing volume fractions

There are two known techniques for determining the mass fractions. These are the Sub-division volume counting and the Level-Set method respectively. Both of them are explained here briefly.

3.7.1. Sub-division volume counting

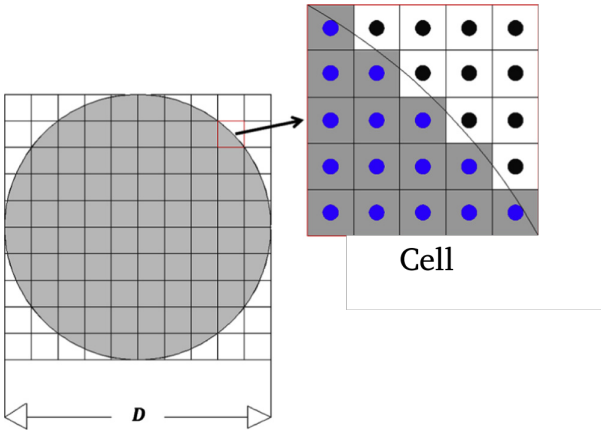

Figure 3.4: Method of Sub-division volume counting. The mass fraction of the solid (shown in grey) in the cell is given by the ratio of the number of the blue dots in the cell to the total number of the dots in the cell. 'D' is the diameter of the immersed solid. Image courtesy [Zaidi et al., 2014].

Sub-division volume counting, as explained in Fig. 3.4, is the process of dividing an interfacial cell into sub-cells and obtaining the mass fractions through the ratio of the number of points inside and outside the solid respectively. Thus the mass fraction of the cell in Fig. 3.4 is given by

$$\alpha_{cell} = \frac{N_{bluepoints}}{N_{totalpoints}} \tag{3.20}$$

3.7.2. Level-Set Method

Kempe et al. [Kempe and Fröhlich, 2012] adapted the method of level-sets from [Osher and Sethian, 1988] to track the solid-fluid interface for a spheroid. In this method, a level set function ϕ is defined in such a way that $\phi = 0$ represents the moving interface $\Gamma(t)$, $\phi < 0$ represents the set of level surfaces that are inside the interface and $\phi > 0$ represents the set of level surfaces that are outside the interface.

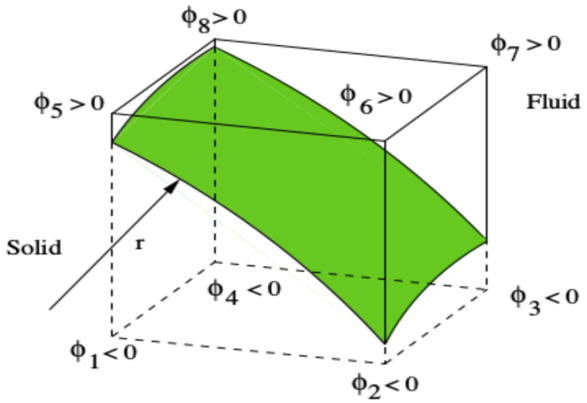

Figure 3.5: Method of Level-Sets from Kempte et al. [Kempe and Fröhlich, 2012]. The fluid-solid interface is shown in green. ϕ represents the level set function for the fluid-solid interface (equation 3.21) and is evaluated at the corner points of the cell. Reproduced from [Kempe and Fröhlich, 2012]

The level-set function as shown in Fig. 3.5 is evaluated at the corner points of the cell. It is given by equation 3.21, where (*x,y*) are the coordinates of the point under consideration, (x_p,y_p) are the coordinates of the geometric centre of the spheroid, and (*a,b,c*) are the lengths of the semi-major axes of the spheroid.

$$\phi_{x,y} = \sqrt{\frac{(x-x_p)^2}{a^2} + \frac{(y-y_p)^2}{b^2} + \frac{(z-z_p)^2}{c^2}} - 1 \tag{3.21}$$

The mass fraction (α) is computed by equation 3.22. In equation 3.22, ϕ_n represents the level-set function defined at the corners (n) of the cube.

$$\alpha = \frac{\Sigma_{n=1}^{n=8} - \phi_n H(-\phi_n)}{\Sigma_{n=1}^{n=8} |\phi_n|} \tag{3.22}$$

where $H(\phi_n)$ is the heaviside step function defined as

$$H(x) = \begin{cases} 0 & x < 0 \\ 1 & x > 0 \end{cases}$$

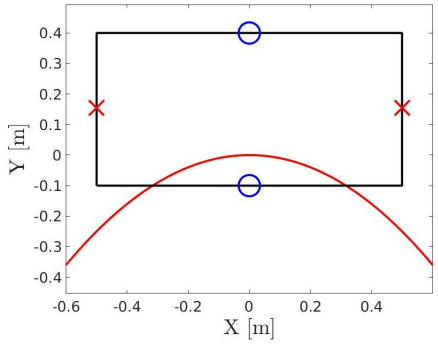

Figure 3.6: Interfacial cells that could occur with a deforming interface. U and V velocities are computed at the points represented by x's and o's respectively. The deforming interface is shown in red.

It is very much possible that there are interfacial cells as shown in Fig. 3.6. In these kinds of cells, all the 4 corners of the cell lie outside the interface (shown in red) and yet there is a finite fraction of the mass of the cell that is occupied by the object. The level-set method however would yield a mass fraction of 0 for these kinds of cells and hence is not used in this work.

All the above mentioned methods are simply not accurate enough to compute the mass fraction. Hence, an accurate method to compute the volume fraction is important. The accuracy issues in the above methods can be overcome by using algorithms from computational geometry. An open source library [Lemoine et al., 2017] implementing these algorithms is utilized in this work for computing the mass fractions. The algorithm for polygon clipping by Joseph O'Rourke [O'Rourke et al., 1982] is used to find the coordinates of the clipped polygon. The area of the polygon is then computed from the Green's theorem as given by the below equation .

$$A = \sum_{k=0}^{n} \frac{(x_{k+1} + x_k)(y_{k+1} - y_k)}{2} \tag{3.23}$$

where A denotes the area of the polygon, and x_k, y_k denote the k^{th} vertices of the polygon. In a Cartesian coordinate system, the volume of the polygon is obtained by multiplying the area by the grid spacing in the *z* direction (Δz). In a cylindrical coordinate system, the volume of the solid formed by the revolution of the polygon is obtained by multiplying the area with the the circumferential length $2\pi r_c$ where r_c is the radius of the centroid of the solid formed by the revolution. The accuracy of this technique in computing the mass fractions is shown in the Appendix A.2. The coupling between the deforming object to the Cartesian grid is shown in the Appendix A.3.

4

Code Validation

In this chapter, validation of the numerical method is presented. Four standard two-dimensional test cases have been used to validate the code. The first-two test cases use a Cartesian coordinate system. The model swimmer, which is of interest to this work, is spherical and deforms its body axisymmetrically. Hence, the Cartesian code was adapted to a cylindrical coordinate system.

4.1. Flow over a stationary cylinder

Steady and unsteady flow over a stationary cylinder at two different Reynolds numbers of 40 and 100 have been simulated. The values of the drag and the lift coefficients obtained for both the cases are found to be in good agreement with those reported in the literature.

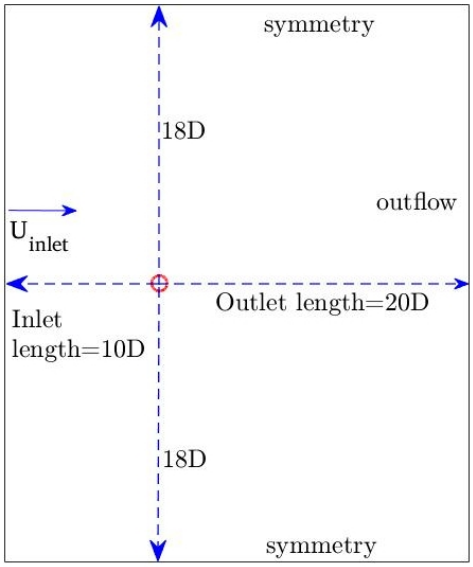

Figure 4.1: Computational domain of *30D X 36D* as used in the test cases.The cylinder with a diameter '*D*' is indicated in red. Inflow and outflow boundary conditions are imposed at the left and the right boundaries respectively. Symmetry boundary conditions are imposed on the top and bottom boundaries respectively. The direction of the flow is from left to right

As shown in Fig. 4.1, a large computational domain of *30D X 36D* (where *D* denotes the diameter of the cylinder) is chosen to prevent any influence of the boundary conditions on the flow near the cylinder. A uniform flow velocity ($u = U_{inlet} = 1$, $v = 0$) is imposed at the left boundary. Outflow ($\frac{\partial u}{\partial x} = 0$, $\frac{\partial v}{\partial x} = 0$) boundary conditions are imposed at the right boundary. The top and bottom boundaries are

specified with symmetry boundary conditions ($\frac{\partial u}{\partial y} = 0$, $v = 0$). Neumann boundary condition for the pressure ($\frac{\partial p}{\partial n} = 0$) is imposed for the all the boundaries except the right, where the Dirichlet boundary condition ($p = 0$) is specified. A uniform grid has been chosen with $\Delta x = \Delta y = \frac{D}{32}$ with a fixed time step $\Delta t = 0.01$ (*CFL*=$\frac{U_\infty \Delta t}{\Delta x} = 0.32$), where *CFL* denotes the Courant-Friedrichs-Lewy condition. The mean value of the drag coefficient (for the case of an unsteady flow over the cylinder) that was obtained for a lower grid resolution with $\Delta x = \Delta y = \frac{D}{16}$ and a time step $\Delta t = 0.01$ (*CFL=0.16*) differed by 5% with the standard value found in literature. On refining the grid, the mean value drag differed by about 0.7% with the value found in literature. Hence the finer grid was chosen for the further test cases. The differences in the drag and the lift coefficients for the two grids are shown in the Appendix A.4.

4.2. Steady flow

The drag and the lift coefficients for the steady flow over a cylinder at a Reynolds number of 40 have been compared to values reported in the literature. The numerical schemes chosen in the code and in FLUENT for this and all the other cases which are explained in the subsequent sections, are tabulated in table 4.1. In addition to the drag and the lift coefficients, the characteristic parameters of the wake as shown in Fig. 4.2 are compared to values from the literature. Both of them are found to be in good agreement with each other and are tabulated in table 4.2.

Settings chosen	**FLUENT**	**Code used in the present work**
Spatial Discretization	Central Differencing	Central Differencing
Temporal Discretization	Second order Implicit	Crank-Nicholson (2^{nd} order), Adams-Bashforth (3^{rd} order)

Table 4.1: Comparison of the numerical schemes used by a body conforming grid (FLUENT) and the code used in the present work. The Crank-Nicholson and the Adams-Bashforth scheme are used for the integration of the diffusion and the advection terms repsectively.

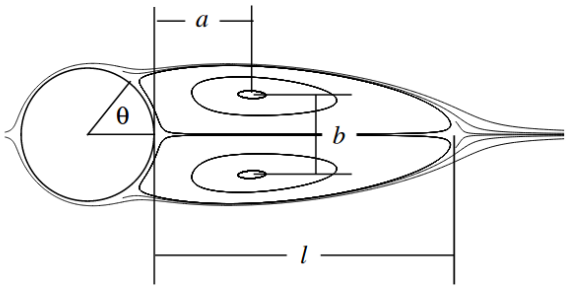

Figure 4.2: Parameters for the steady state wake as defined by Coutanceau and Bouard. *'a'* represents the distance between the cylinder and the centre of the upper vortex, *'b'* represents the distance between the two vortices,*'l'* represents the complete length of the recirculation zone. *'θ'* represents the separation angle calculated from the x-axis.

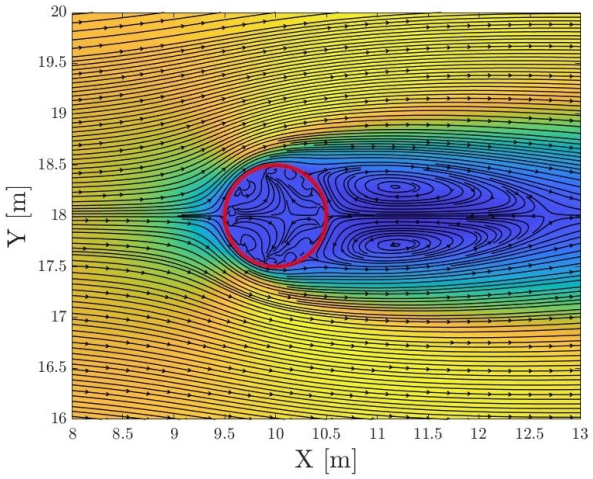

Figure 4.3: The symmetric steady state wake for the flow over a cylinder (shown in red) at a Reynolds number of 40 ($\frac{D}{\Delta x} = 32$,*CFL=0.32*). Streamlines can be seen to penetrate into the surface of the cylinder because the no-slip boundary condition is only approximately enforced in the present IBM.

	$\frac{l}{d}$	$\frac{a}{d}$	$\frac{b}{d}$	$\theta(^\circ)$	C_D
Linnick and Fasel	2.28	0.72	0.6	53.6	1.54
Coutanceau and Bouard (experiment)	2.13	0.76	0.59	53.8	-
Taira and Colonius	2.33	0.75	0.6	54.1	1.55
Present work	2.17	0.69	0.59	53.3	1.56

Table 4.2: Comparison of the steady state wake structure obtained from the present work with values from the literature. The definitions for *a,b,c,d* and *l* can be found in Fig. 4.2. θ denotes the separation angle and C_D denotes the drag coefficient.

The coefficient of pressure (C_p) in Fig. 4.5d is obtained by taking the values of the pressure at the points that lie in the vicinity of the cylinder. The points that lie in the vicinity of the cylinder are the centre of the cells whose distance from the centre of the cylinder is given by equation 4.1. The cells that satisfy the criteria are identified first and the pressures at these points are plotted with the polar angles of the points. The polar angle of these points is given by equation 4.2. Equation 4.1 is only satisfied upto a certain tolerance (on the order of the grid width). This results in identifying multiple points that lie inside and outside the cylinder with the same polar angle. Hence, there appears to be two lines in the curves for the pressure coefficient in Fig. 4.5d.

$$\sqrt{(x_{cell} - x_{cylinder})^2 + (y_{cell} - y_{cylinder})^2} \approx R \tag{4.1}$$

$$\theta \approx tan^{-1} \frac{y_{cell}}{x_{cylinder} - x_{cell}} \tag{4.2}$$

Here, $x_{cell}, y_{cell}, x_{cylinder}, y_{cylinder}$ denote the coordinates of the centre of the cell and the coordinates of the centre of the cylinder respectively. R denotes the radius of the cylinder. The drag and the lift forces for all the cases in the cartesian code are obtained by volume integrals of the force over the body as given by equation 4.3 [Noor et al., 2009]. The drag and the lift coefficients are then obtained by scaling them accordingly as given by equations 4.4 and 4.5 respectively.

$$\vec{F} = \sum_{n=1}^{n=N} \vec{f}_n dV_n \tag{4.3}$$

where, N is the number of cells in the grid, dV is the volume of the grid cell, and f_n is the forcing in one time step given by equation 3.19.

$$C_D = \frac{F_D}{0.5\rho U_\infty^2 A} \tag{4.4}$$

$$C_L = \frac{F_L}{0.5\rho U_\infty^2 A} \tag{4.5}$$

where, F_D, F_L are the drag force and the lift force obtained from equation 4.3, U_∞ is the fluid velocity at infinity and A is the frontal area of the object. In the axisymmetric case, the volume of each element (dV) can be obtained by $rdrdz$.

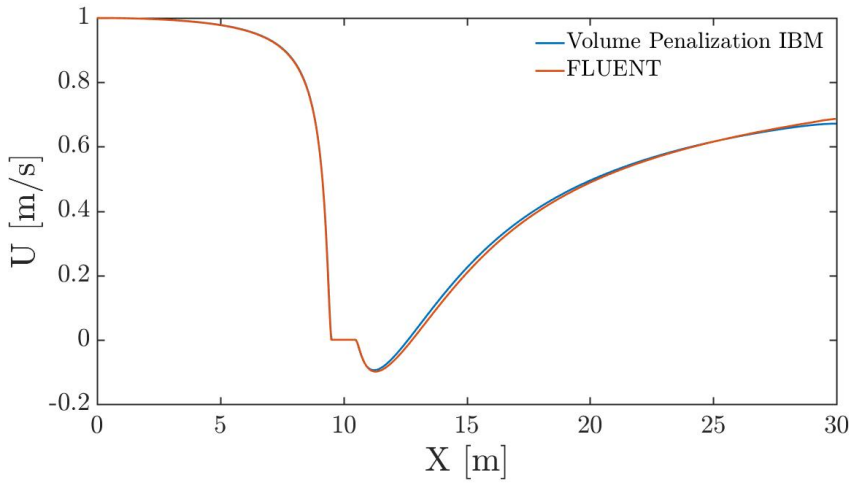

(a)

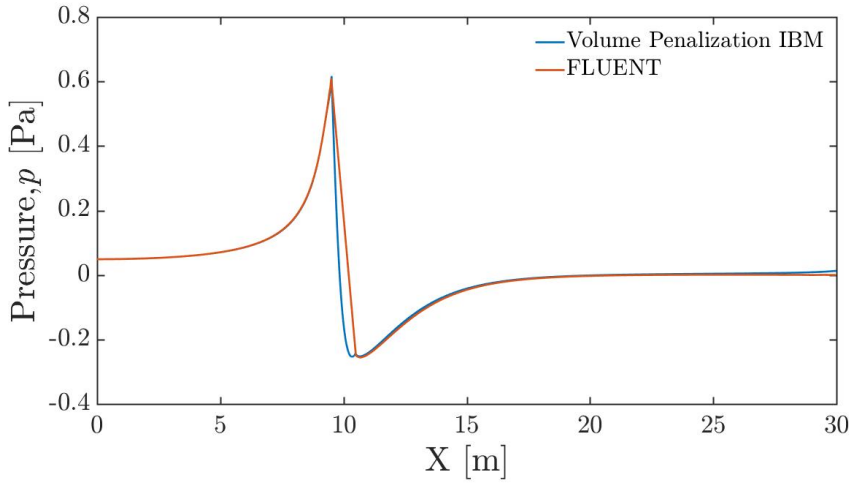

(b)

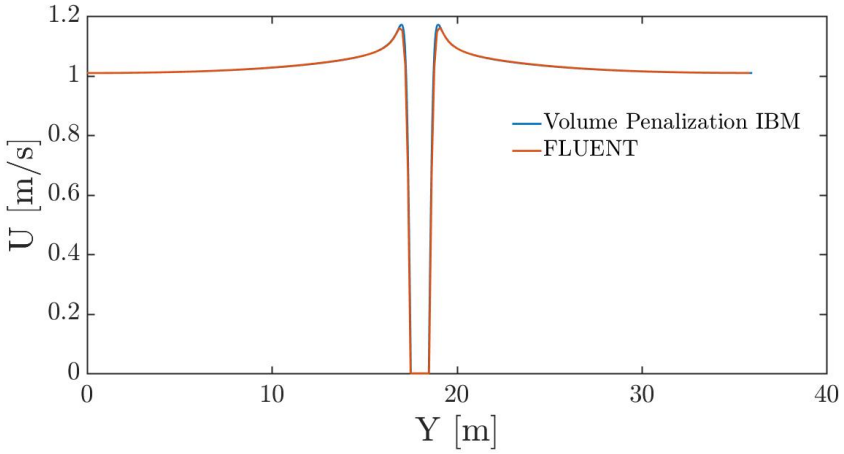

(c)

Figure 4.4: Comparison of the velocity and the pressure profiles obtained from the present IBM with those from a body conforming grid (FLUENT). (a): U-velocity ($\frac{m}{s}$) plotted along the horizontal centreline; (b): Pressure (Pa) plotted along the horizontal centreline; (C): U-velocity ($\frac{m}{s}$) along the vertical centreline.

The velocity and the pressure profiles obtained from the present work have been compared to those from a code (FLUENT) that uses body conforming grids. These are shown in Fig.4.4a,4.4b & 4.4c. As can be seen from the Fig. 4.4a, the length of the recirculation region is determined accurately by the present-IBM. A close up of the contours for the pressure and the vorticity are shown in Fig. 4.5a and Fig. 4.5b. It can be seen from Fig. 4.5a that the behaviour of the pressure near the cylinder is smooth.

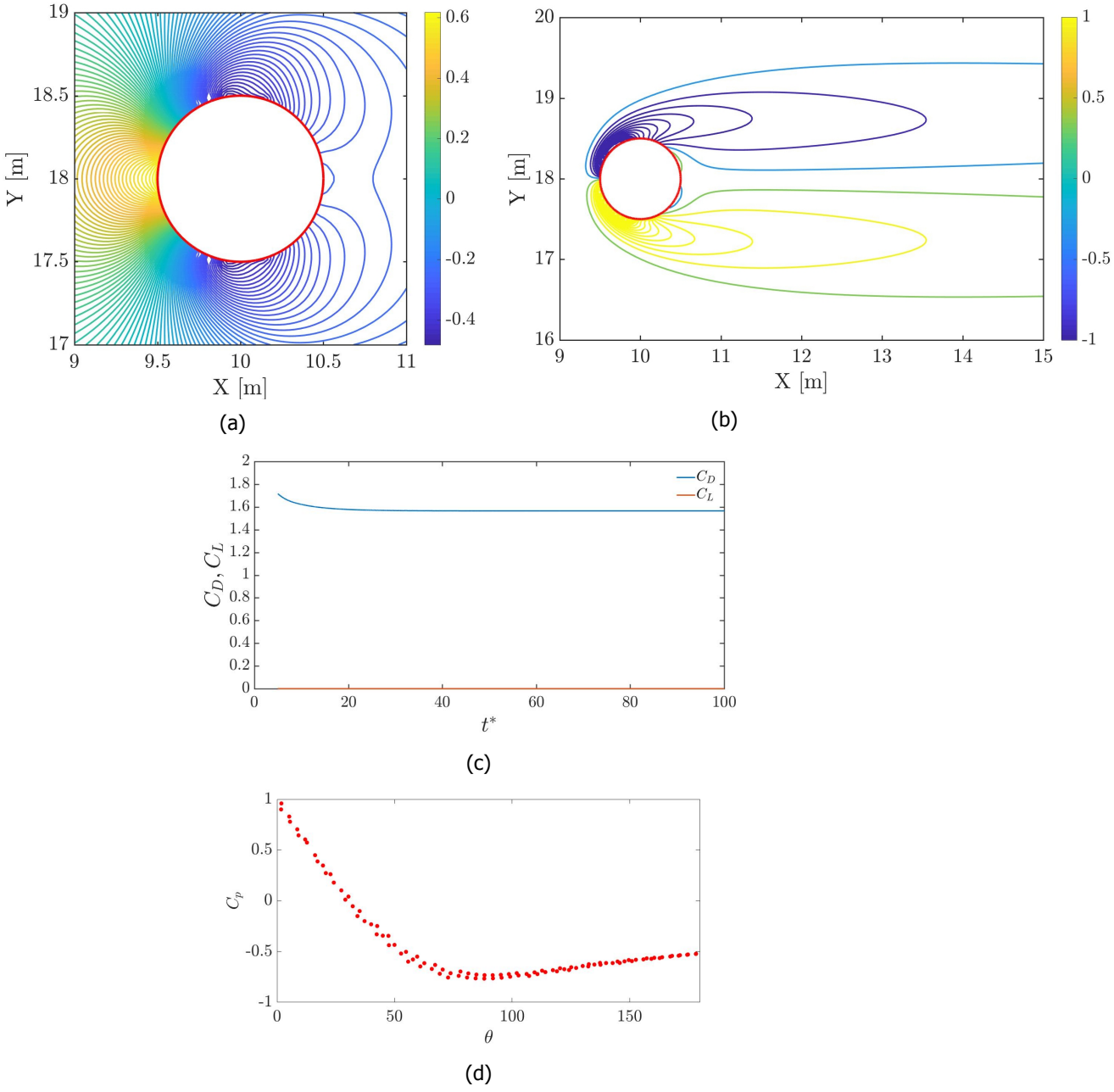

Figure 4.5: Results for the flow over a cylinder (shown in red), at a Reynolds number of 40 that is obtained from the code. The inside of the cylinder is coloured in white. (a): Contours of the pressure (Pa) close to the cylinder; (b): Contours of the vorticity close to the cylinder. (c): The drag and the lift coefficients plotted against the non-dimensional time ($\frac{tU}{d}$). The value for the drag coefficient (C_D) remains steady at 1.565 and the value for the lift coefficient is of the order of machine zero. (d): The plot of the pressure coefficient (C_p) obtained from the code only along the the upper half of the surface of the cylinder (θ).

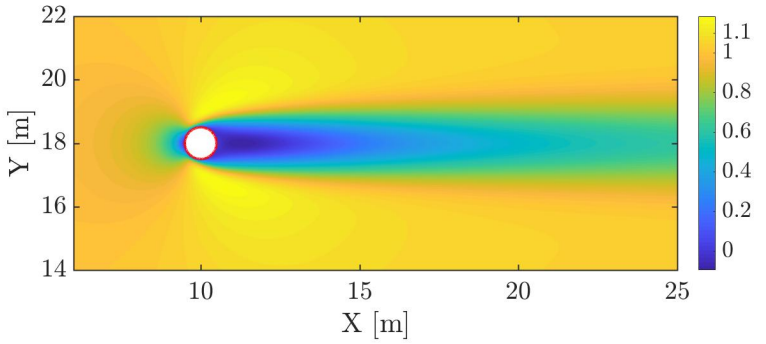

(a)

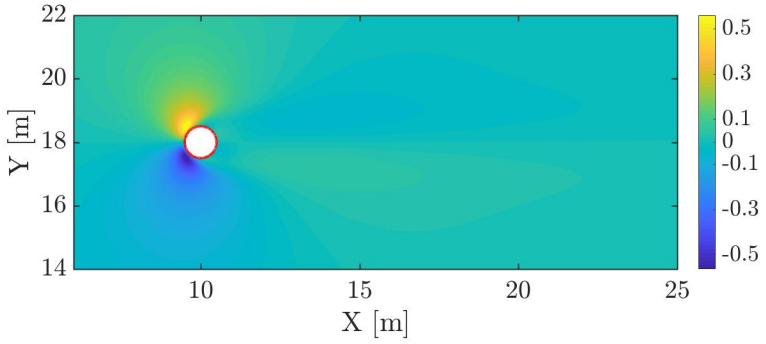

(b)

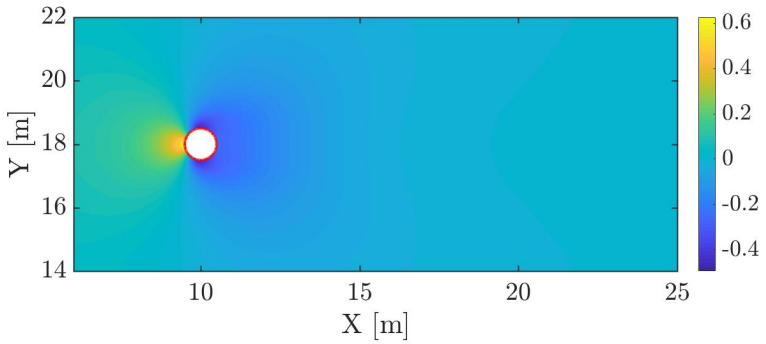

(c)

Figure 4.6: Flow over the cylinder at a Reynolds number of 40. (a): Contours of the u (x-component) velocity in $\frac{m}{s}$. (b): Contours of the v (y-component) velocity in the $\frac{m}{s}$. (c): Contours of the pressure p in Pa.

4.3. Unsteady flow

The mean value of the drag coefficient and the peak value of the lift coefficient (which is a very sensitive quantity to the numerical errors in the code) for the case of an unsteady flow over a cylinder at a Reynolds number of 100 have been plotted in Fig. 4.7. They are compared to the standard values found in the literature and are tabulated in table 4.3. They are found to be in good agreement with the values reported in the literature.

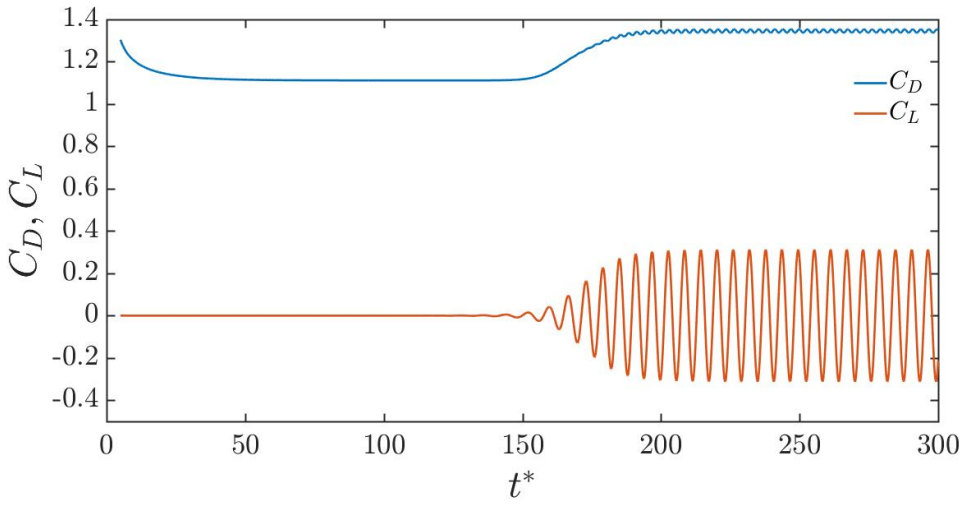

Figure 4.7: Drag (C_D) and the lift (C_L) coefficients as a function of the non dimensional time t^* ($\frac{tU}{d}$) for the flow over a cylinder at a Reynolds number of 100. The average drag coefficient (C_D) obtained was 1.34 and the peak value of the lift coefficient (C_L) was 0.33.

	$C_{D,avg}$	$C_{L,peak}$
Body Conforming Grid [Park et al., 1998]	1.33	0.33
Present work	1.34	0.31

Table 4.3: Comparison of the mean value for the drag and the peak value for the lift coefficient between those obtained from a body conforming grid with the present work.

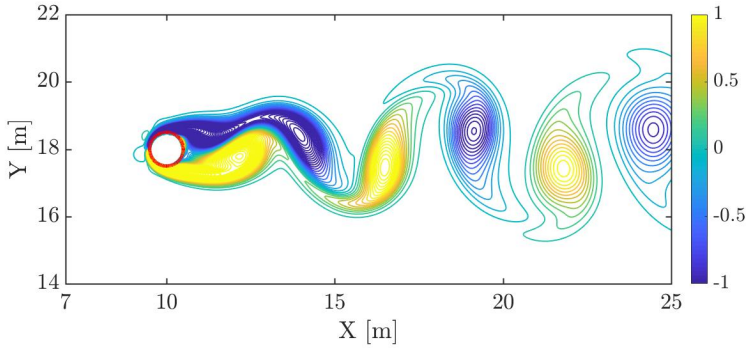

Figure 4.8: Contours of Vorticity ($\frac{1}{s}$) for the flow over a cylinder at a Reynolds number of 100 at t^* =300.

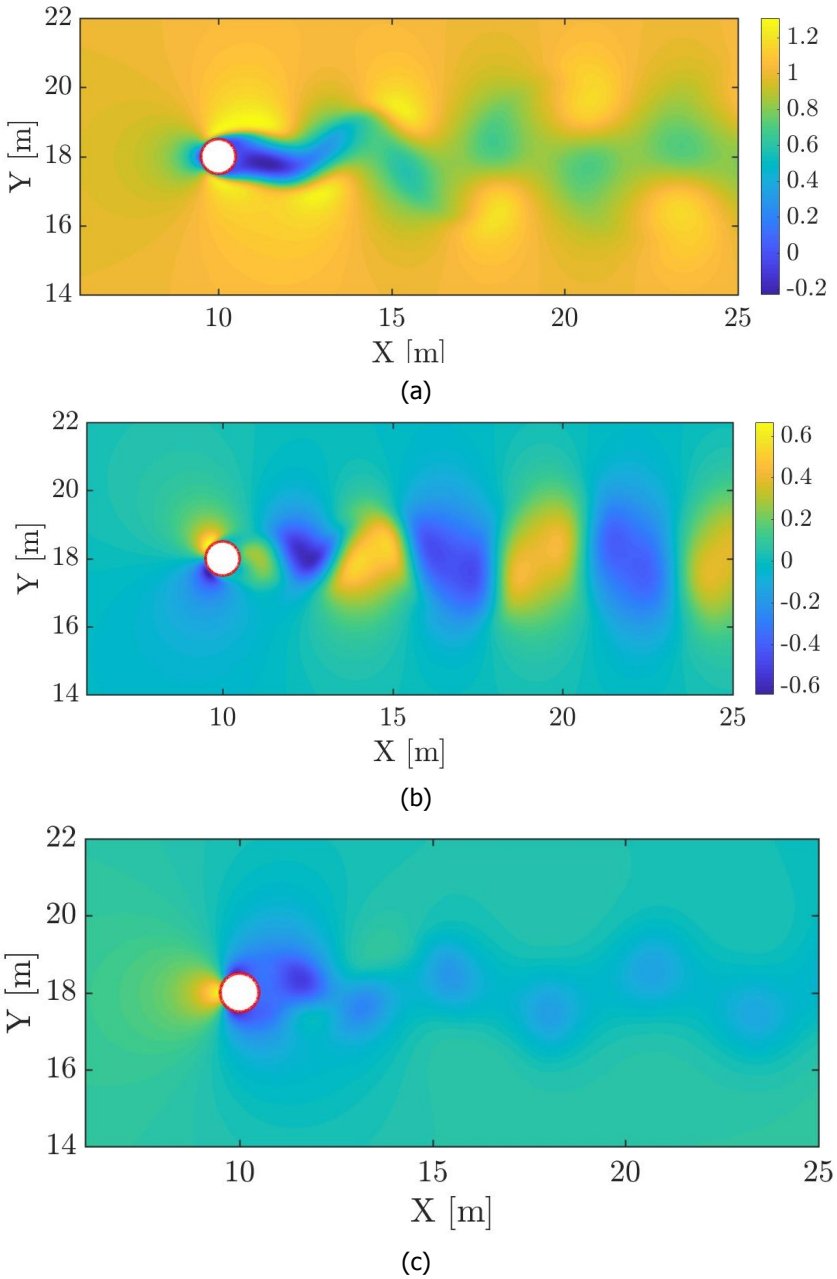

Figure 4.9: Flow over the cylinder at a Reynolds number of 100. (a): Contours of the u (x-component) velocity in $\frac{m}{s}$. (b): Contours of the v (y-component) velocity in the $\frac{m}{s}$. (c): Contours of the pressure p in Pa.

A variant of the volume penalization scheme where the volume fractions (α) are set to binary i.e. 1 when the cell is completely inside or partially filled and 0 when the cell is completely outside, is also tested for the steady flow over a cylinder. The velocity, the pressure and the drag and the lift coefficients from this variant are compared to the non-binary variant for the Reynolds number of 40 and are shown in the Appendix A.5. The drag coefficient obtained from the binary case differed by 1% from the non-binary case for the chosen grid resolution. The binary variant is expected to worsen the problem of spurious force oscillations (explained in section 4.4) as seen in the volume penalization scheme. Hence, the non-binary variant was chosen to be implemented for the further test runs.

4.4. Flow Over a transversely oscillating cylinder

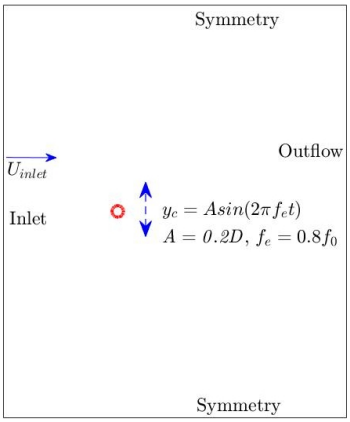

Figure 4.10: Amplitude ('A') and frequency of oscillation ('f_e') of the cylinder. The computational domain and the boundary conditions are the same as the previous case (Fig. 4.11 in section 4.1). The cylinder with diameter 'D' is shown in red.

The second test case was to simulate the flow over a transversely oscillating cylinder at a frequency close to the natural frequency of vortex shedding at $Re = 185$ and obtain the mean value of the drag and the root-mean square values for the lift coefficient. The computational domain remains the same as the one chosen for the stationary cylinder (Fig. 4.10). The flow over an oscillating cylinder at a Reynolds number of 185 is a standard test case for which data is easily available from literature to compare against. Spurious force oscillations (explained in section 4.4) are observed close to the natural frequency of vortex shedding at $Re = 185$. Hence, the cylinder oscillating at close to its natural frequency at the Reynolds number of 185 was chosen.

$$y_c = Asin(2\pi f_e t) \tag{4.6}$$

The oscillations of the centre of the cylinder are prescribed according to equation 4.6, where A is the amplitude, f_e is the forced frequency of oscillation and y_c is the centre of the cylinder. The results for the mean value of the drag and the RMS value for the lift for the forcing frequency have been presented.The drag and the lift coefficients as a function of the non-dimensional time t^* ($\frac{tU}{d}$) are shown in Fig. 4.11. The mean value for the drag is good agreement with [Amiralaei et al., 2010]. The rms value for the lift was 0.2366 while the rms value for the lift obtained from [Uhlmann, 2005] for the same case was 0.166.

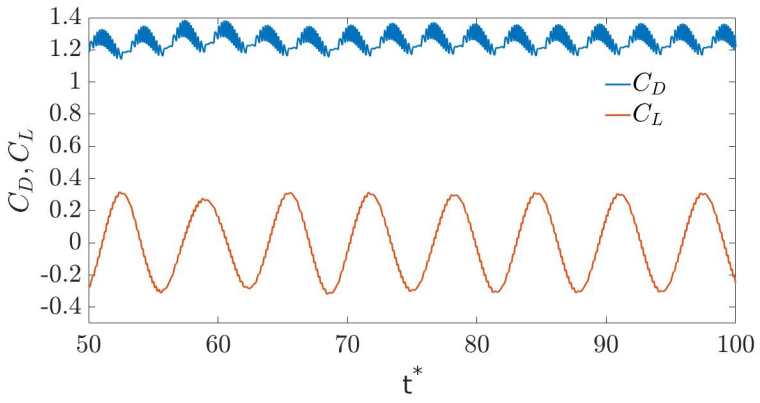

Figure 4.11: The drag and the lift coefficients as function of the non-dimensional time $t^*(\frac{tU}{d})$ for an oscillating cylinder at $Re = 185$,$f_e = 0.8f_0$,$A = 0.2D$. The spikes in the curves are a consequence of the volume penalization scheme. $\overline{C_D} = 1.26$,$C_{L,rms}$ =0.2366.

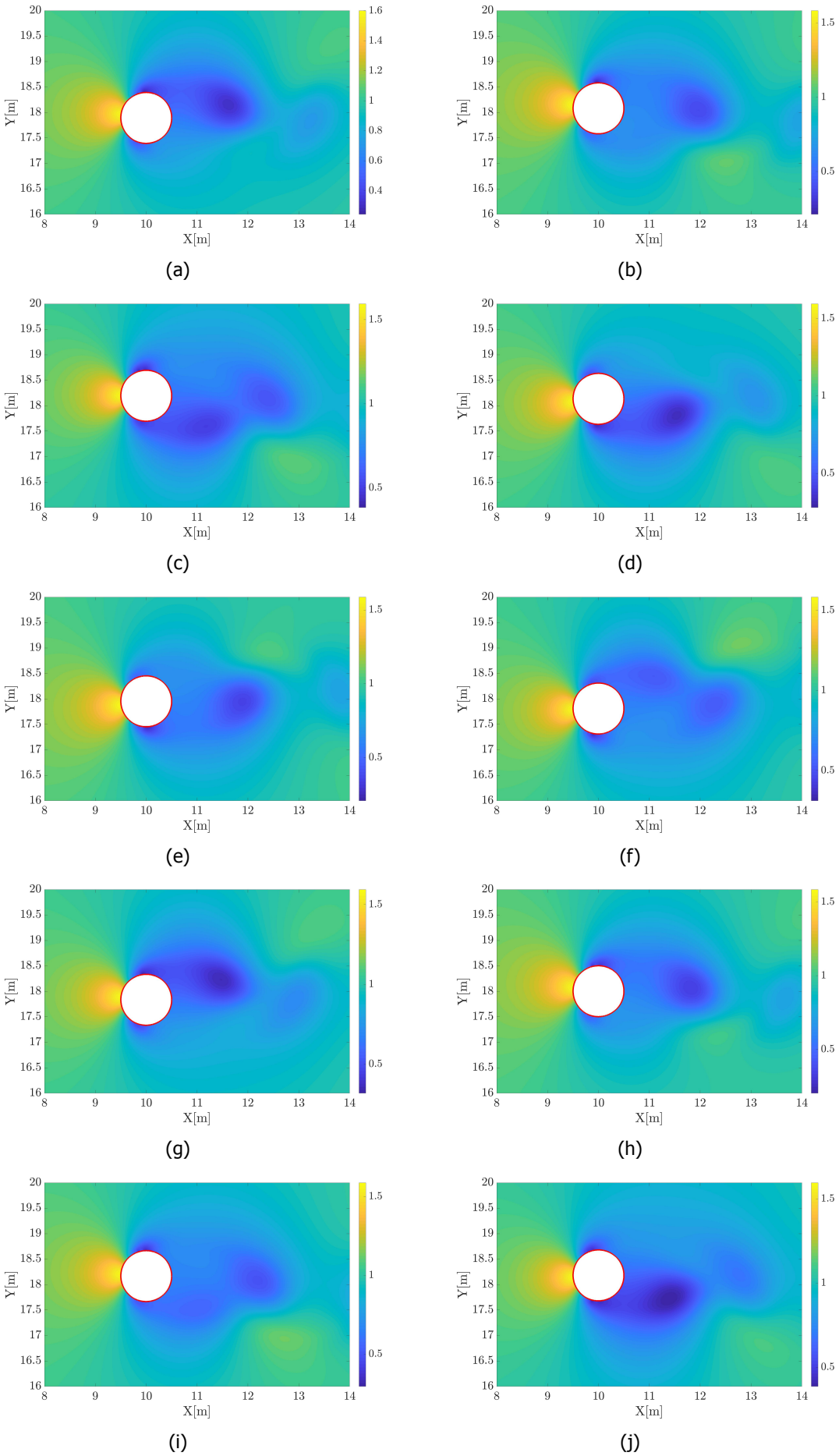

Figure 4.12: Pressure contours at 10 instances of time for 2 cycles of oscillation of the cylinder at *Re*= 185, $f_e = 0.8f_0$, $A = 0.2D$.

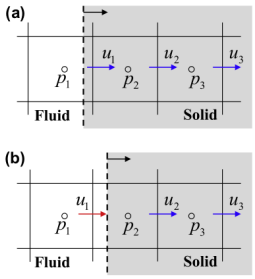

Figure 4.13: The point for the computation of the U-velocity u_1 (shown in blue) switches from solid (shown in grey) as shown in panel *a*, to the fluid as shown in panel *b*, due to the movement of the immersed object. Reproduced from [Lee et al., 2011].

Spurious Force Oscillations (SFO's)

The fictitious force oscillations in the drag and the lift (seen in Fig. 4.14) is because of a grid point switching from solid to fluid, due to the movement of the immersed object, as shown in Fig. 4.13. The grid point that is located inside the solid $t = t_n$ at the old time level is now in the fluid domain at $t = t_{n+1}$. The pressure from the old time level that belonged to the solid now affects the computation of the pressure at the point that is now in the fluid. The volume penalization scheme is expected to alleviate this situation, as the grid point switches only gradually between the solid and the fluid due to the smoothing by the volume fraction α. The resulting pressure field that is computed at the point thus has a contribution from the solid and the fluid. The contribution α is computed very accurately (see the Appendix A.2) in this work. However, this does not help in removing the force oscillations. As shown in Fig. 4.14, interpolating the mass fractions does help a bit in attenuating the force oscillations. However, this too does not remove the force oscillations completely. Hence, other methods to reduce the spurious force oscillations (SFO's) such as increasing the grid spacing or increasing the time step have to be used. The spurious force oscillations worsen in the case of the binary variant in the volume penalization scheme as compared to the non-binary variant. This is shown in the Appendix A.6.

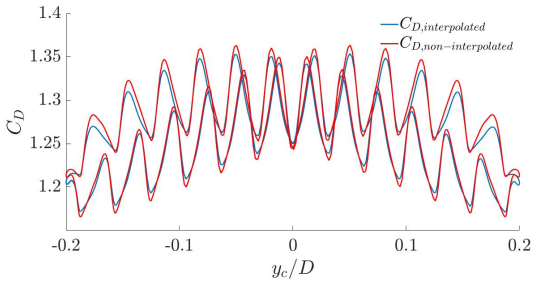

(a)

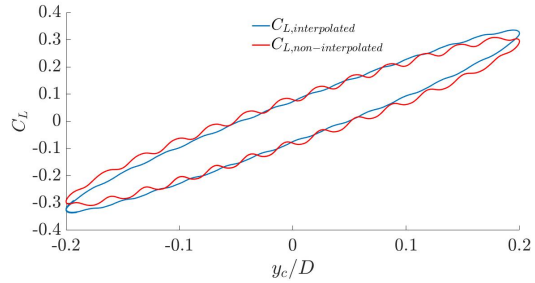

(b)

Figure 4.14: Spurious force oscillations in the drag (panel *a*) and the lift (panel *b*) coefficients for the flow over an oscillating cylinder at *Re*= 185, $f_e = 0.8f_0$,$A = 0.2D$. The curves in red and blue denote the drag coefficients obtained when the mass fractions are non-interpolated and interpolated respectively.

4.5. Axisymmetric flow over a sphere at $Re = 80$

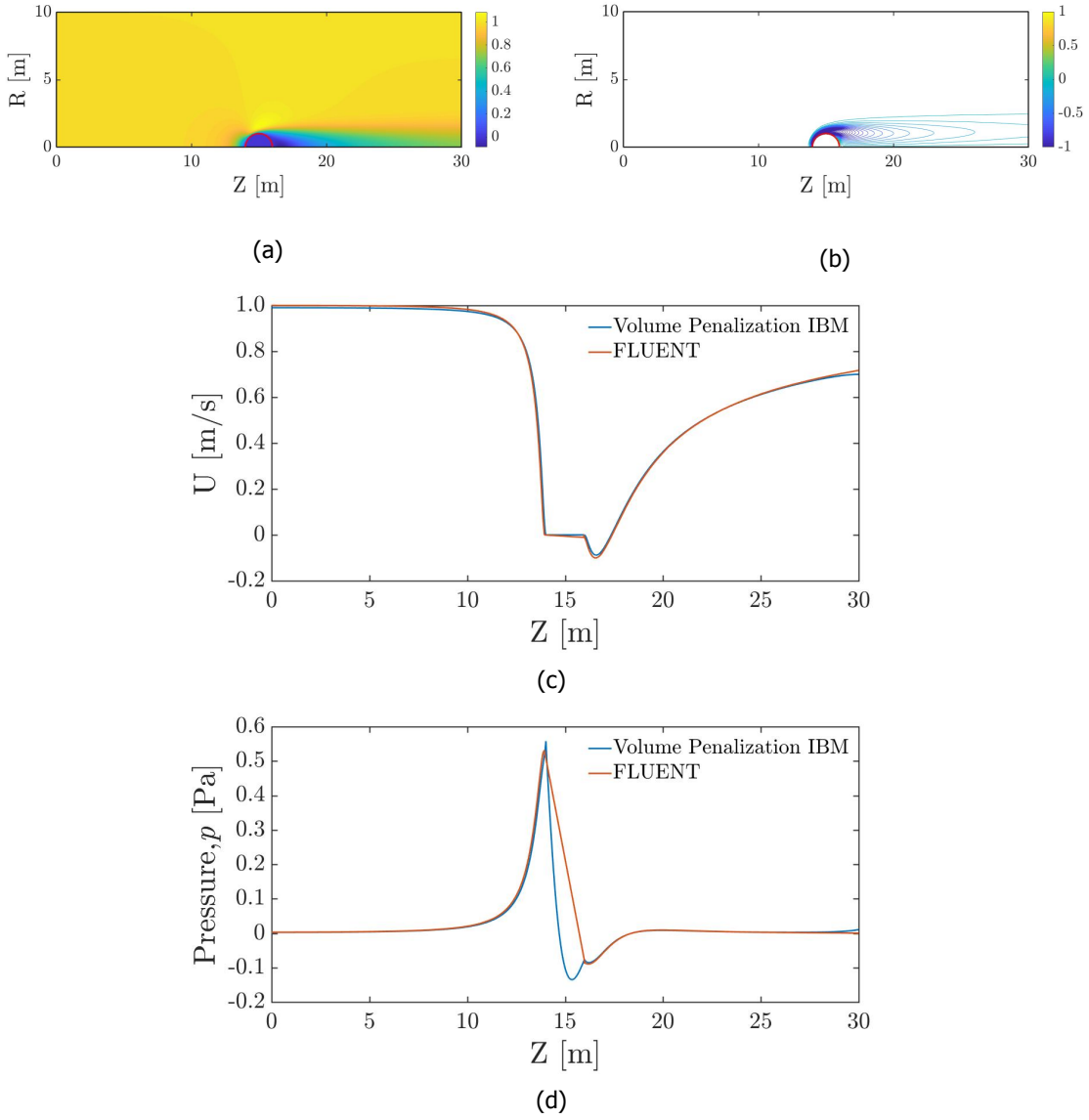

Figure 4.15: Axisymmetric flow over a sphere at a Reynolds number of 80. (a): Contours of the axial velocity (m/s) obtained from the code; (b): Contours of the vorticity ($\frac{1}{s}$) obtained from the code; (c): Comparison of the axial velocity profile (plotted along the axis) obtained from the code with a body conforming grid (FLUENT). (d): Comparison on the pressure (Pa) plotted along the horizontal axis obtained from the code with a body conforming gird (FLUENT).

A third test case to simulate the flow over a deforming cylinder in a Cartesian coordinate system is shown in the Appendix A.7. The mean value of the drag coefficient that is obtained is in reasonable agreement with the value found in literature. The Cartesian code as used in the three test cases is adapted to the cylindrical coordinates to model the swimmer.The case of an axisymmetric flow around a sphere at two Reynolds numbers of 80 ($\nu = 0.025, D = 2, U = 1$) and 0.2 ($\nu = 10, D = 2, U = 1$) was tested prior to modelling the swimmer. As a final test case, the axisymmetric flow over an oscillating sphere at two different values for the viscosity ($\nu = 10$,$\nu = 100$) is simulated. The domain chosen is *30DX36D* in the axial and the radial direction respectively. The sphere is placed along the axis, at the centre of the domain. The simulations for the cases where the sphere stays stationary are done

with a uniform grid ($\Delta x = \Delta y = \frac{D}{64}$), and time step with *CFL=0.32*. The contours of the axial velocity and the vorticity obtained for the axisymmetric flow over a sphere at the Reynolds number of 80 are shown in Fig. 4.15a and 4.15b respectively. The velocity and the pressure for the same case profiles as shown in Fig. 4.15c and 4.15d obtained from the code are compared to those obtained from a body conforming grid (FLUENT) and are in good agreement with them. The coefficient of the pressure for the above case (which is also sensitive to numerical errors) is validated against FLUENT and is shown in Appendix A.8 .

4.6. Grid-Independence

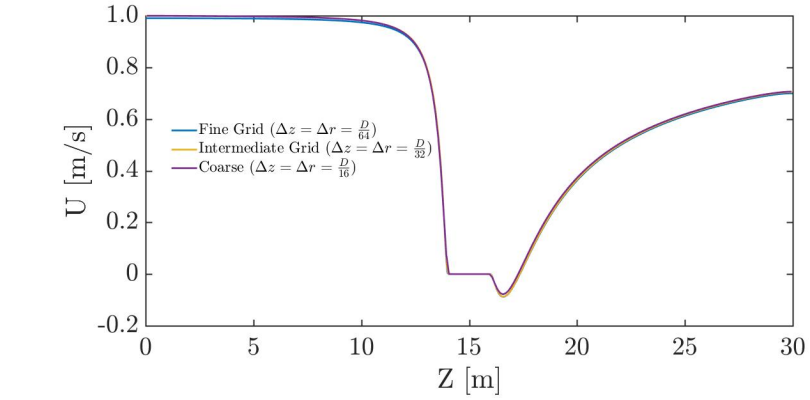

(a)

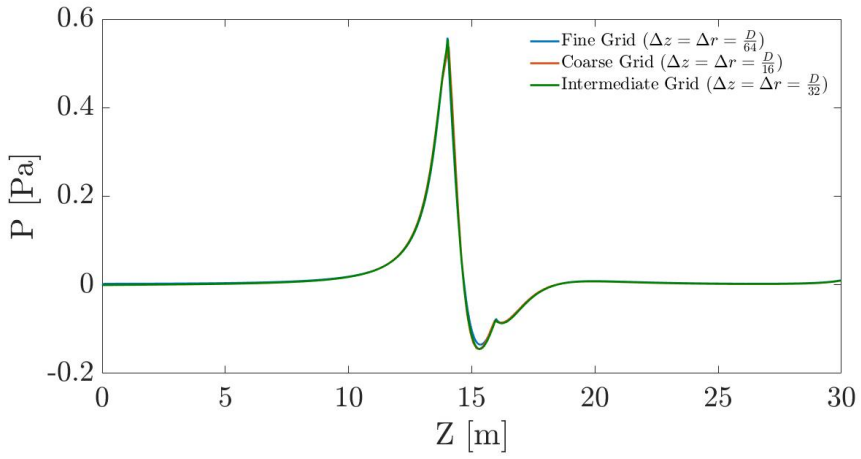

(b)

Figure 4.16: Plots of the axial velocity (panel *a*) and the pressure (panel *b*) along the centreline for three different grid configurations with $\Delta z = \Delta r = \frac{D}{64}, \Delta z = \Delta r = \frac{D}{32}, \Delta z = \Delta r = \frac{D}{16}$.

Uniform grids with three different resolutions ($\Delta z = \Delta r = \frac{D}{64}, \Delta z = \Delta r = \frac{D}{32}, \Delta z = \Delta r = \frac{D}{16}$) were used in this case to check the dependence of the solution on the mesh. The plots of the axial velocity and the pressure along the axis are shown in Fig. 4.16a and Fig. 4.16b. The differences in the solutions obtained are minimal. Hence the intermediate grid was used in all the further test runs.
The contours of the axial velocity for the flow over the sphere at $\nu = 10, D = 2, U = 1$ are shown in Fig. 4.17a. There is no separation observed at this Reynolds number as shown by the streamlines in Fig. 4.17b in contrast to Fig. 4.15a which is obtained at a higher Reynolds number of 80. The velocity and the pressure profiles have been compared to that from a body conforming grid as shown in Fig. 4.17c-Fig. 4.17e. They are found to be in good agreement with each other.

4.7. Axisymmetric flow over the sphere at $Re = 0.2$

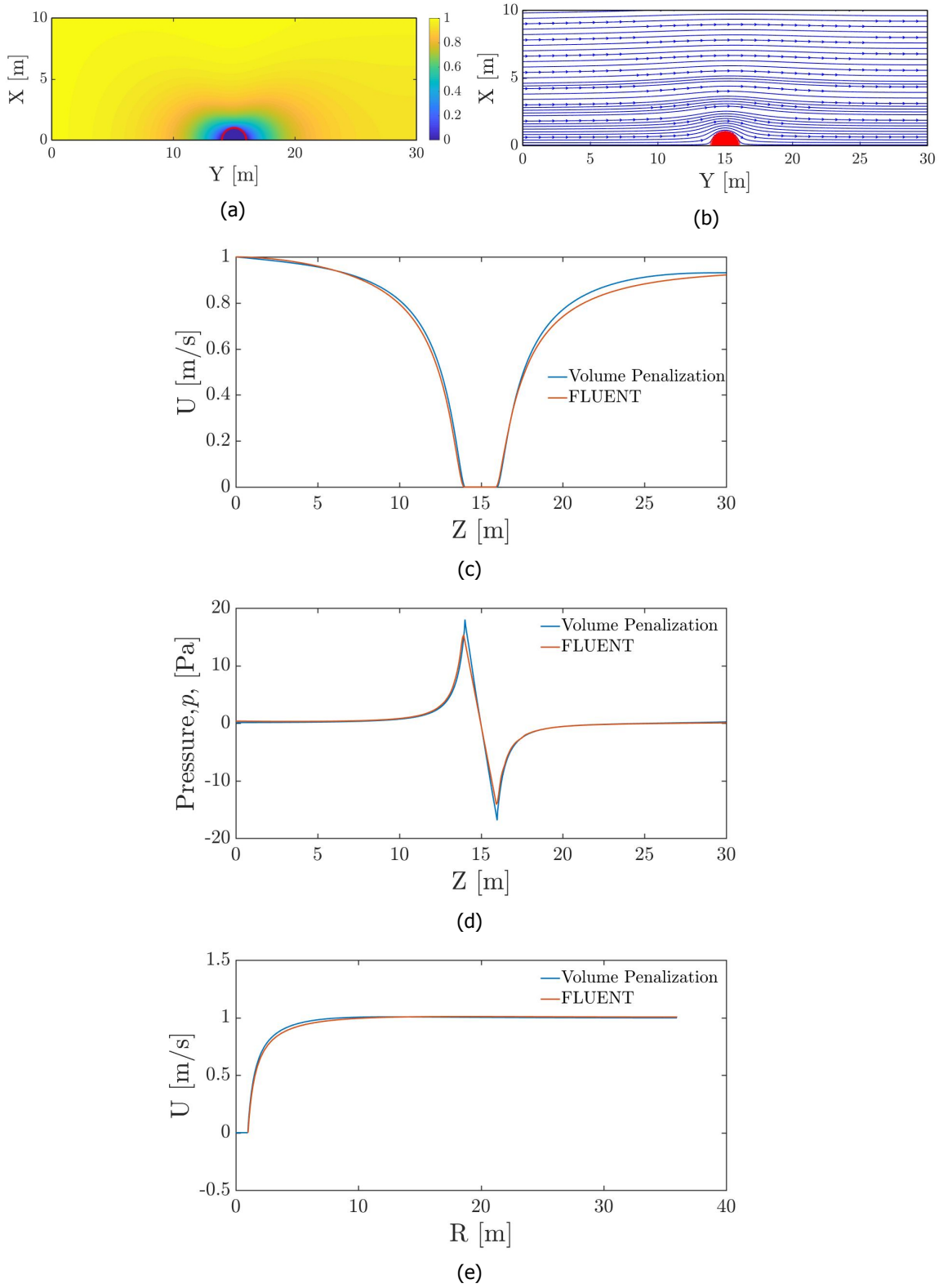

Figure 4.17: Axisymmetric flow over a sphere at a Reynolds number of 0.1. (a): Contours of the axial velocity (m/s) obtained from the code; (b): Streamlines obtained from the code; (c): Comparison of the axial velocity profile (plotted along the axis) obtained from the code with a body conforming grid (FLUENT). (d): Comparison of the pressure (Pa) plotted along the axis obtained from the code with a body conforming grid (FLUENT). (e): Comparison of the axial velocity with the vertical centreline that is obtained from the code with a body conforming grid (FLUENT).

4.8. Axisymmetric flow around an oscillating sphere

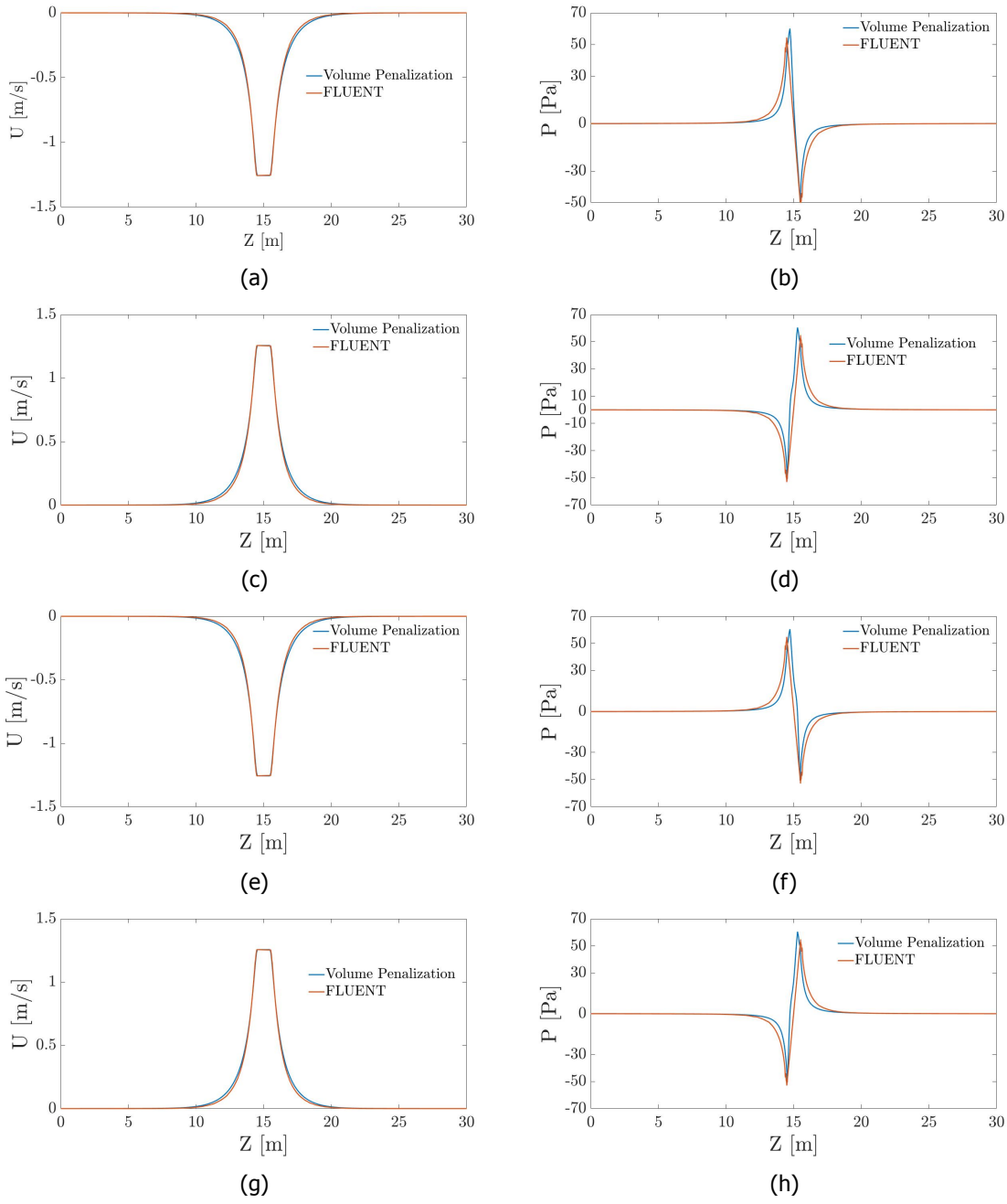

Figure 4.18: Comparison of the axial velocity (left section) and the pressure (right section) along the axis for the flow over a horizontally oscillating sphere, obtained from the code to a body conforming grid (FLUENT) at t=0.5 T_{cycle}, T_{cycle}, 2.5 T_{cycle},4 T_{cycle} respectively from top to bottom. This is done for a viscosity of 10 $\frac{m^2}{s}$.

The case of an axisymmetric flow around an oscillating sphere in a fluid with viscosity (ν=10 $\frac{m^2}{s}$) and (ν=100 $\frac{m^2}{s}$) is chosen to validate a moving object in a cylindrical coordinate system. The domain is a square domain with edge-length 30*D*. The centre of the sphere is a periodic function of time as given by equation 4.7.

$$z_c = Asin(2\pi ft) \tag{4.7}$$

where z_c, A, f, t denote the centre of the sphere, amplitude of the oscillation, frequency of the oscillation and the time respectively. The Amplitude of the oscillation is $A = 0.2D$ and the frequency $f = 1$. The simulation is run for 4 cycles of the oscillations of the sphere. The velocity and the pressure profiles are compared with those of a body conforming grid (FLUENT) and are shown in Fig. 4.18 for a viscosity $\nu = 10\frac{m^2}{s}$ and in Fig. 4.19 for a viscosity $\nu = 100\frac{m^2}{s}$ respectively.

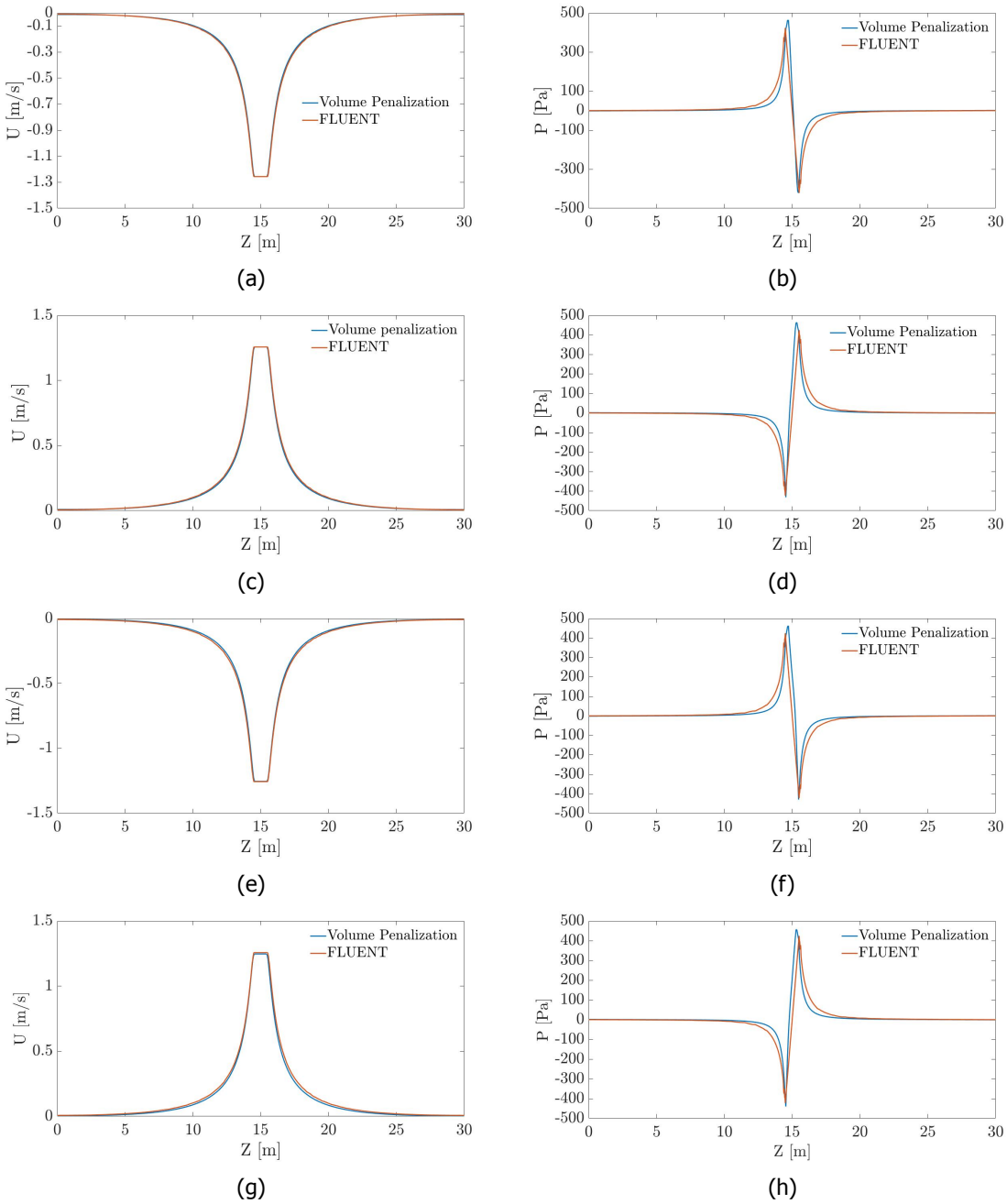

Figure 4.19: Comparison of the axial velocity (left section) and the pressure (right section) along the axis for the flow over a horizontally oscillating sphere, obtained from the code to a body conforming grid (FLUENT) at t=0.5 T_{cycle},T_{cycle}, 1.5 T_{cycle}, 2 T_{cycle} respectively from top to bottom. This is done for a viscosity of 100 $\frac{m^2}{s}$.

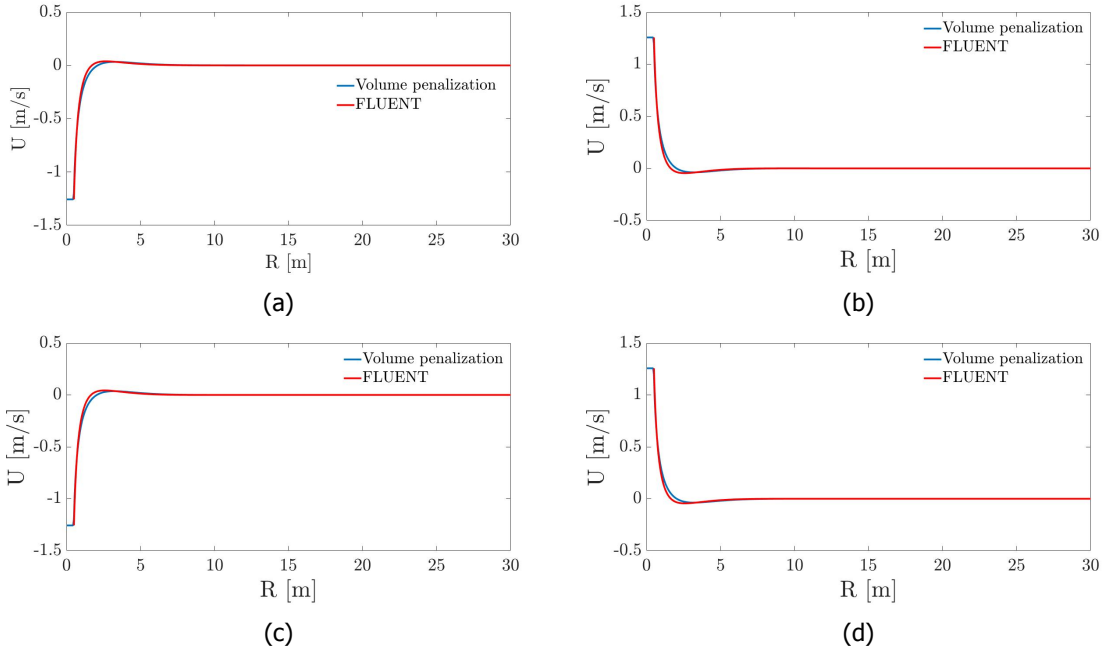

Figure 4.20: Comparison of the axial velocity along the vertical axis for the flow over a horizontally oscillating sphere, obtained from the code to a body conforming grid (FLUENT) at t=0.5 T_{cycle},T_{cycle}, 1.5 T_{cycle}, 2 T_{cycle} respectively from top to bottom. This is done for a viscosity of 10 $\frac{m^2}{s}$.

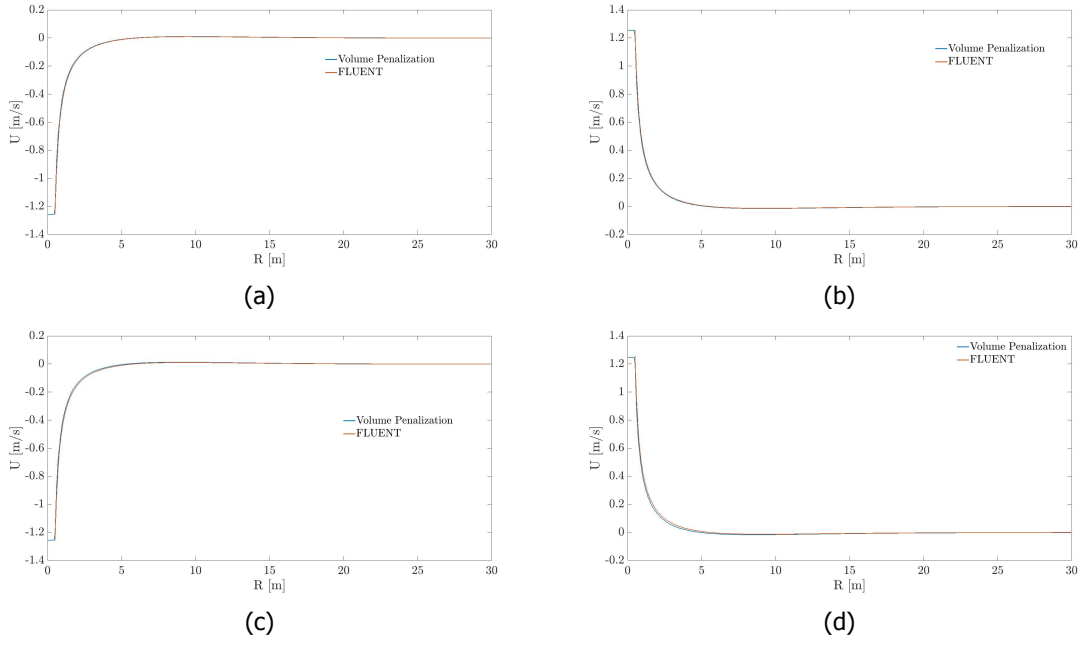

Figure 4.21: Comparison of the axial velocity along the vertical axis for the flow over a horizontally oscillating sphere, obtained from the code to a body conforming grid (FLUENT) at t=0.5 T_{cycle},T_{cycle}, 1.5 T_{cycle}, 2 T_{cycle} respectively from top to bottom. This is done for a viscosity of 100 $\frac{m^2}{s}$.

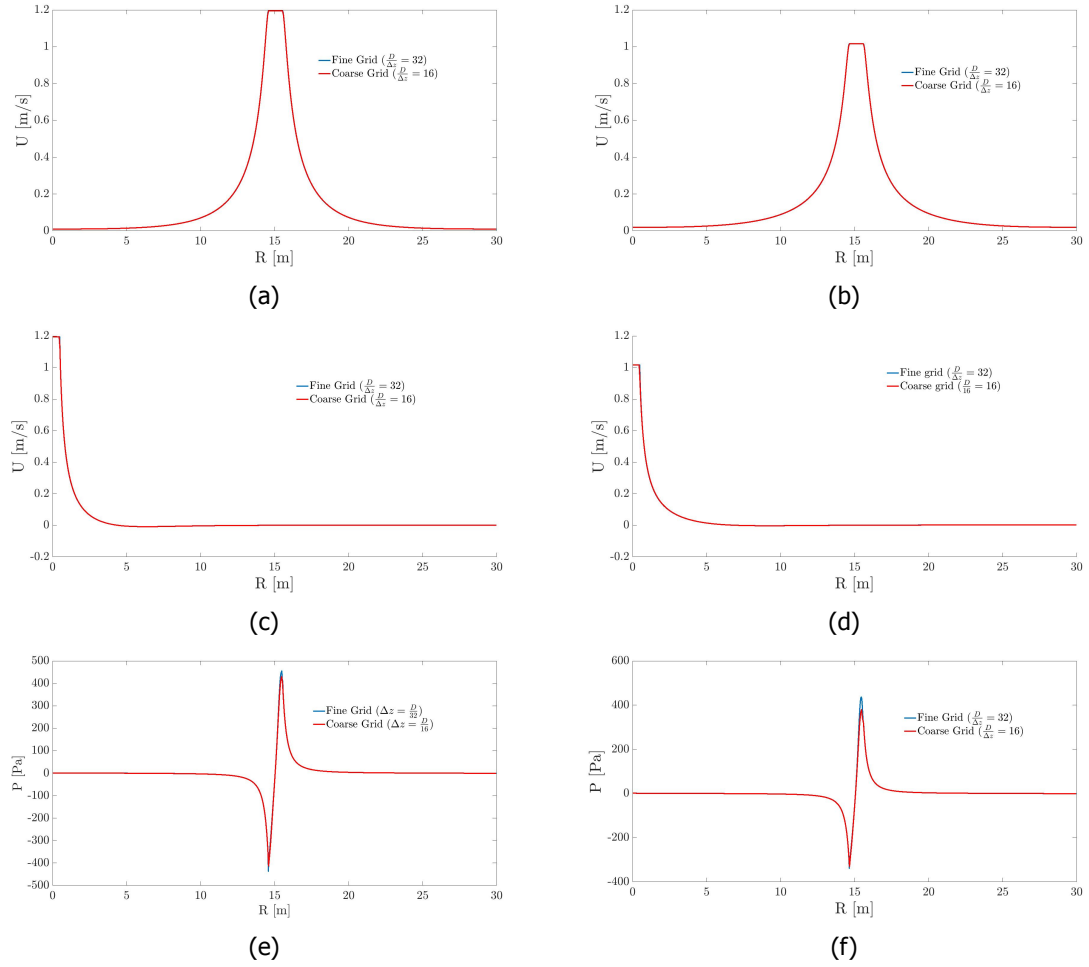

Figure 4.22: Grid Independence for the flow around an oscillating sphere at a viscosity $\nu = 100\frac{m^2}{s}$ for two time instants $t = \frac{T_{cycle}}{20}$ and $t = \frac{T_{cycle}}{10}$. (a): The axial velocity profiles along the axis for $t = \frac{T_{cycle}}{20}$ in the left and the $t = \frac{T_{cycle}}{10}$ in the right. (b): The axial velocity profiles along the vertical centreline $t = \frac{T_{cycle}}{20}$ in the left and the $t = \frac{T_{cycle}}{10}$ in the right. (c): The pressure profiles along the axis for $t = \frac{T_{cycle}}{20}$ in the left and the $t = \frac{T_{cycle}}{10}$ in the right. The red line denotes the coarse grid and the blue line denotes the fine grid.

In both the cases of the oscillating sphere, a second-order accurate upwind scheme was used for the spatial integration and a first order accurate implicit scheme was used for the time-integration in FLUENT. The plots of the axial velocity along the vertical centerline and the axis as obtained from the code, for both the cases of the oscillating sphere as shown in Fig. 4.18-4.21 , are in good agreement with those obtained from FLUENT. There are differences however, in the plots of the pressure along the centreline in both the cases of the oscillating sphere. This could be because of the grid and the time integration scheme used in FLUENT. This could also be related to the addition of the extra terms in the code, in the pressure correction equation as given by equation 3.18. However the addition of the extra terms in the code is necessary as the diffusion terms are being solved implicitly. A finer grid with $\Delta z = \frac{D}{32}, \Delta r = \frac{D}{38}$ is used to check the dependence of the solution on the mesh. The results for the axial velocities and the pressure along the axis and the axial velocities along the vertical centreline for the two time instants $t = \frac{T_{cycle}}{20}$ and $t = \frac{T_{cycle}}{10}$ are shown in Fig. 4.22 respectively.

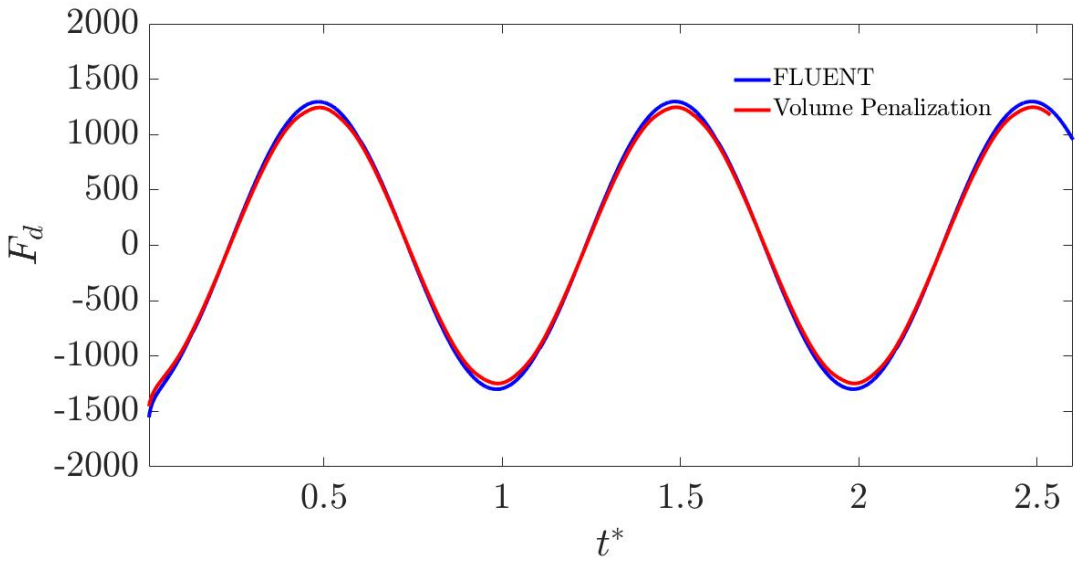

Figure 4.23: Comparison of the unscaled drag force on the oscillating sphere at a viscosity (ν) of 100 $\frac{m^2}{s}$ as obtained from the code (shown in red) with a code that uses a body conforming grid (FLUENT) as shown in blue, for two cycles of the oscillation. t^* denotes the number of cycles. F_d denotes the unscaled drag force.

The drag force (unscaled) for the coarser grid, is compared with FLUENT for the case of the oscillating sphere at the viscosity (ν) of 100 $\frac{m^2}{s}$ for more than two cycles of the oscillation, in Fig. 4.23. It is in good agreement with the body conforming grid (FLUENT).

4.9. Conclusions from the validations of the code

1. The computation of the mass fractions accurately is important as setting the mass fractions to binary leads to spurious force oscillations in the coefficients for the drag and the lift.

2. However, an accurate computation of the mass fractions does not completely solve the problem of the spurious force oscillations seen in the computation of the drag and the lift coefficients for a moving/deforming object.

3. The code is able to handle moving boundaries in highly viscous flows in a cylindrical coordinate system. This can be seen from the plots of the drag coefficients in Fig. 4.23 and the velocity profiles in the figures 4.18-4.21.

4. The grid with the configuration $\Delta z = \frac{D}{16}, \Delta r = \frac{D}{19}$ is sufficient for an accurate computation of the forces and the velocity profiles for a moving boundary in a cylindrical coordinate system. Hence, this grid configuration could be used to model the combined-stroke-swimmer.

5

Results and Discussion

In this chapter, the results obtained for the combined-stoke-swimmer for four cases at increasing scale numbers $s = 0.11, 0.25, 0.79$ and 3.03 are presented. First, a short summary of the combined-stroke-swimmer is presented. Then, the details on the computational domain and the boundary conditions are described. The results including the streamlines, the vorticity and the axial velocity profiles with time which are obtained from the simulations are then presented.

The parameters *a*, $\nu(\frac{m^2}{s})$ and T_{cycle} used in the following sections, denote the radius of the swimmer, kinematic viscosity of the fluid and the cycle time (*sec*) of the swimmer respectively. Re, Re_ω and ω are the Reynolds number, the unsteady Reynolds number and the frequency of the distorting swimmer ($\omega = \frac{2\pi}{T_{cycle}}$) respectively. The swimmer is assumed to be neutrally buoyant, so the density of the swimmer (ρ_s) is the same as the density of the fluid (ρ_f).

5.1. Combined-stroke-swimmer

As explained previously in section 2.6, only the first three terms are considered in the series expansion for the perturbation $\vec{\xi}$ to prescribe the deformations of the sphere. The swimming velocity is then obtained in a labratory frame of reference to the second order in the perturbation $\vec{\xi}$. The deformations are given by equation 5.1. The combined-stroke-swimmer is then realized by specifying values to certain coefficients in the expansion 5.1. The deformations during one cycle for the combined stroke swimmer are shown in Fig. 5.1

$$\vec{\xi}(\vec{s},t) = \sum_{i=1}^{3} M_i(t)\vec{u}_i(a,\theta) + \sum_{i=2}^{3} K_i(t)\vec{v}_i(a,\theta) \tag{5.1}$$

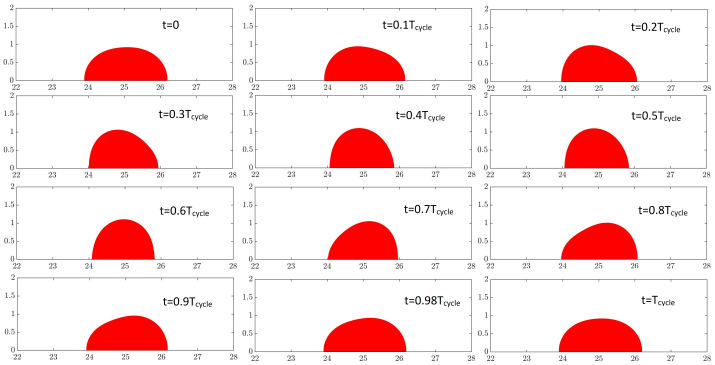

Figure 5.1: Deformations (one-half) of the combined-stroke-swimmer ($\mu_{1c} = 0.05, \kappa_{3c} = -0.022, \kappa_{2s} = 0.0621$ used in equation 5.1) as shown in red. The sequence is to be read clockwise from top-left. T_{cycle} in the frames denotes the cycle time of the swimmer. The Z and R axes are in the horizontal and the vertical direction respectively.

5.2. Domain

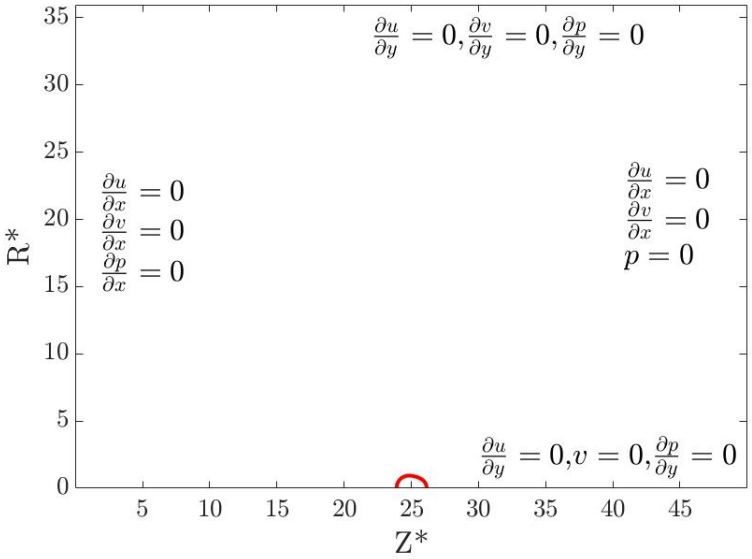

Figure 5.2: Computational domain (2D) for the swimmer. The swimmer is shown in red. R* and Z* are the height and length of the domain non-dimensionalized by the radius of the swimmer. The axis of symmetry is at R*=0. Neumann boundary conditions are used at all the boundaries for the axial and the radial velocities (u,v) and the pressure (p) except at the outlet and at the axis.

As shown in Fig. 5.2, a large computational domain is chosen to minimize the influence of the boundary conditions on the flow near the swimmer. The swimmer (with radius R) is placed at a distance of $25R$ from the left and the right boundaries. The top boundary is $36R$ from the swimmer. The reference frame used in the present work is that of the swimmer. Neumann boundary conditions are used at all the boundaries for the axial (u) and the radial (v) velocities respectively. The swimming velocities are obtained as a function of time, at points which are located at distances increasing radially from the swimmer as shown in Fig. 5.3. Since the frame of reference is a co-moving frame of reference, the axial velocities at all the points obtained in the far field ($> 7R$) should tend to reach the velocity of swimming of the combined-stroke-swimmer.

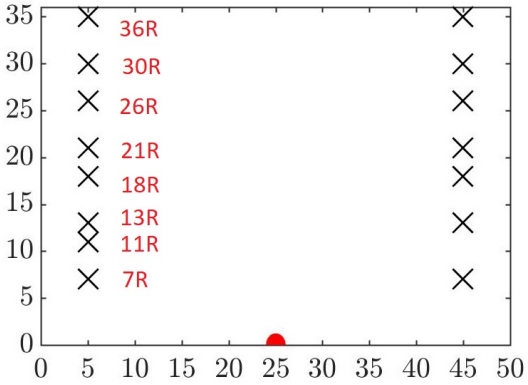

Figure 5.3: Monitor points (shown by the black x's) are placed at distances which increase radially from the swimmer. The velocities induced by the deformations of the swimmer are measured at these points. *R* denotes the radius of the swimmer. The swimmer is shown in red.

5.3. Input Parameters

The combined-stroke-swimmer has been simulated at four increasing scale numbers. The values of the kinematic viscosity (ν), the frequency of distortion (ω) used to achieve the desired scale numbers (s), their corresponding unsteady Reynolds numbers (Re_ω) are tabulated in table 5.1. The characteristic length scale is the radius of the swimmer ($a = 1$) in all the cases.

Case number	$\nu(\frac{m^2}{s})$	$T_{cycle}(s)$	$\omega = \frac{2\pi}{T_{cycle}}$	$s = a\sqrt{\frac{\omega}{2\nu}}$	$Re_\omega = \frac{\omega L^2}{\nu}$
1	100	2.5	2.51	0.11	0.0251
2	100	0.5	12.56	0.25	0.1256
3	2	2.5	2.51	0.79	1.255
4	0.034	10	0.6283	3.03	18.47
5	500	0.5	12.56	0.11	0.02512

Table 5.1: Input parameters used to obtain the swimming velocity of the combined-stroke-swimmer at four different scale numbers (s). The fifth case uses a different viscosity to obtain the same scale number as case 1, to compare with the swimming velocity obtained in case 1.

5.4. Results

The results at four scale numbers $s = 0.11, 0.25, 0.79, 3.03$ are presented in the following section. The axial velocity as a function of the non-dimensionlized time for the fifth case is shown in the Appendix A.9. The axial velocities are plotted with the non-dimensionalized time (ωt) for all the scale numbers in Fig. 5.4 and the non-dimensionalized forces are plotted in Fig. 5.5. The second prediction velocities at the interfacial cells and the interior of the swimmer are given by equation 5.2. There is no interior forcing in all the cases that are simulated.

$$\begin{cases} u^{**} = (1-\alpha)u^* + \alpha U_{solid}^{n+1} & \text{at the interface} \\ u^{**} = u^* & \text{in the interior of the swimmer} \end{cases} \tag{5.2}$$

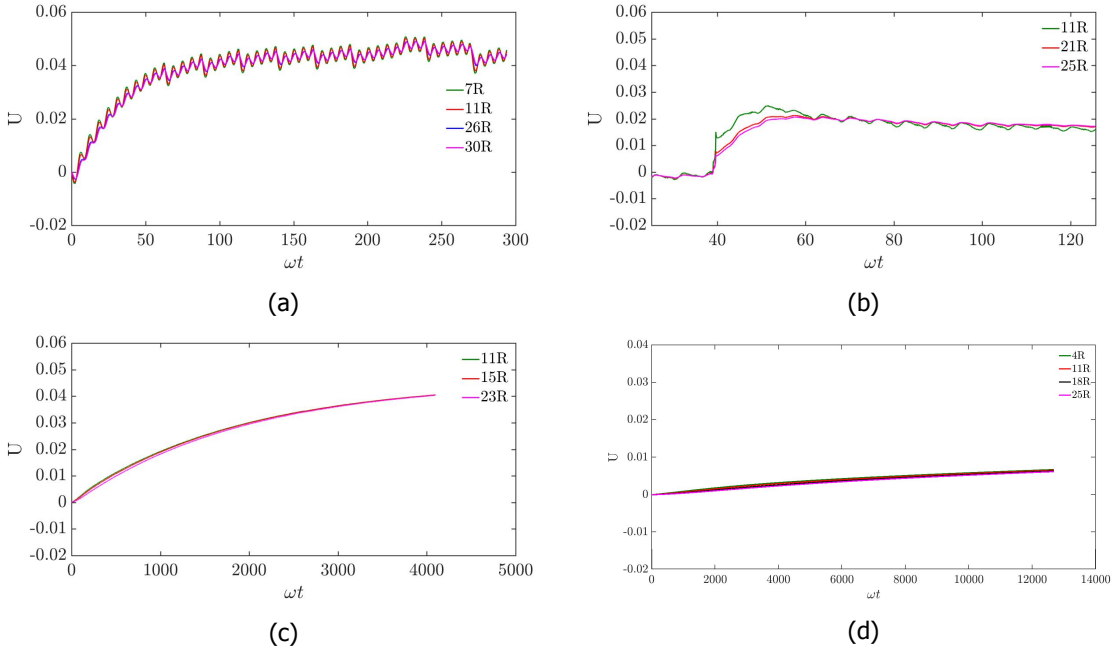

Figure 5.4: The plot of the axial velocities ($\frac{m}{s}$) induced by the swimmer at increasing distances from it with the non-dimensional time (ωt) at (a): $s = 0.11$; (b): $s = 0.25$; (c): $s = 0.79$; (d): $s = 3.03$; *R* denotes the radius of the swimmer. The axial velocities are plotted for (a): 48 cycles (b): 20 cycles (c): 640 cycles, and (d): 1910 cycles of the swimmer respectively.

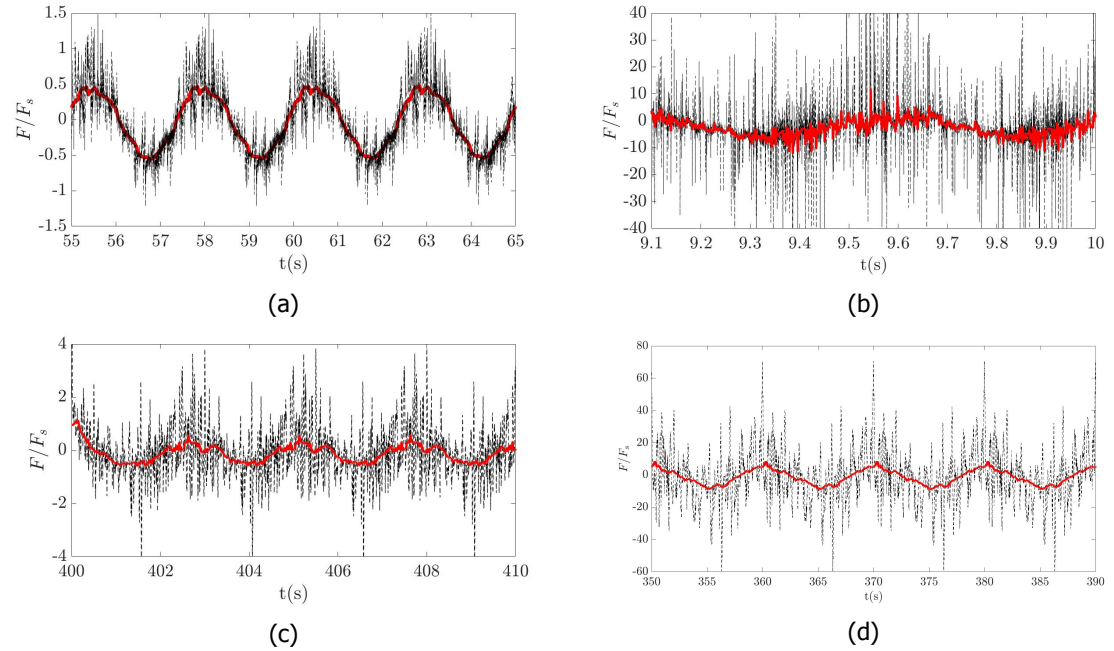

Figure 5.5: The plot of the non-dimensionalized forces on the swimmer at (a): $s = 0.11$; (b): $s = 0.25$; (c): $s = 0.79$; (d): $s = 3.03$; The forces are non- dimensionalized by the Stokes drag acting on a sphere of radius 1 and moving with the velocity of the swimmer at the respective scale number. The forces are plotted for (a): 4 cycles (b): 2 cycles (c): 5 cycles, and (d): 5 cycles of the swimmer respectively. Oscillations in the unfiltered force are observed (shown in black).The spurious oscillations in the curves of the force are a consequence of the Volume penalization scheme that is chosen. The filtered force data is shown in red. A median filter of the 3rd order is used to filter the spurious force oscillations.

5.5. Case 1, $s = 0.11$

The axial velocities are plotted with the non-dimensionalized time in Fig . 5.4a for case 1 ($s = 0.11$). The simulation is done for 49 cycles of the swimmer. The radial velocity induced is 0. There are oscillations in the axial velocities at all the monitor points in the domain. However, this does not imply that the swimmer is accelerating/decelerating. The monitor points are located at finite distances from the swimmer and due to the high viscosity of the fluid, they feel the effects of the surface distortions and oscillate in time. The acceleration of the swimmer (if any) is computed from the force on the swimmer. The axial force on the swimmer that is non-dimensionalized by the Stokes drag ($\propto \mu U_0 l$) on a sphere with the length-scale l and moving with the mean velocity of the swimmer (U_0), is given by Fig. 5.5a. The time average of the force on the swimmer over a cycle is 0. The spurious oscillations in the force curve in Fig. 5.5a are a consequence of the Volume penalization scheme that is chosen. The unsteady Reynolds number for this case is two orders of magnitude less than 1, so the effects of unsteady inertia which arise due to the unsteady beating of the swimmer can be neglected. Hence, there are no fictitious force terms added to the governing equations. In addition to the fictitious forces, the total hydrodynamic force on the swimmer also includes the contribution from the Basset force and the added mass force. The contribution from these two non-fictitious forces become more pronounced at $StRe >> 1$ (see section 2.5). The Strouhal number (St) and the Reynolds number (Re) for the present case ($U \approx 0.04$, $L = a = 1$, $\nu = 100$, $f = \frac{2\pi}{T_{cycle}}$) are given by equations 5.3 and 5.4. As given by equation 5.5, $Re_\omega(StRe) < 1$. Hence, in this case the Basset force and the added mass forces could also be neglected.

$$St = \frac{fL}{U} = \frac{2\pi}{0.04 \cdot 2.5} \approx 62.83 \tag{5.3}$$

$$Re = \frac{UL}{\nu} = \frac{1 * 0.04}{100} \approx 4 \cdot 10^{-4} \tag{5.4}$$

$$StRe = 4 \cdot 10^{-4} \cdot 62.83 \approx 2.5 \cdot 10^{-2} \tag{5.5}$$

The unsteady Reynolds numbers for this case and case 2 (explained in the following section) are close to those obtained for an *Algal cell* and *Opalina* where the effects of unsteady inertia need not be taken into account. This is shown in the table 5.2.

Organism	$a(\mu m)$	$\omega(Hz)$	$U(\frac{mm}{s})$	Re	St	$Re_\omega(StRe)$
Algal cell	5	207.3	0.3	0.0015	3.5	0.005
Opalina	175	25.13	0.1	0.02	44	0.8
Paramecium	125	188.49	1	0.13	24	3
Pleurobrachia	15000	10	-	-	-	3500

Table 5.2: Typical length scales and unsteady reynolds numbers for microscopic organisms. a denotes the radius of the organism. ω denotes the frequency of the beat. U denotes the swimming speed of the organism. Re and St are the Reynolds number and the Strouhal number respectively. Re_ω is the product of the Strouhal and the Reynolds number. Reproduced from [Wang and Ardekani, 2012b].

Streamlines for the far field and the near field are shown in section 5.9 by Fig. 5.6 and Fig. 5.7 respectively. A recirculation region is seen close to the surface of the swimmer in the near-field as shown in Fig. 5.7. The recirculation region shifts its position in the same way as the surface distortions of the swimmer, unlike those in pushers or pullers, where the regions of recirculation appear in front/back of the organisms (see Fig. 2.7). In the far-field, the streamlines are parallel to each other as shown in Fig. 5.6. Contour plots of the vorticity in the near field of the swimmer are shown in section 5.9 by Fig. 5.8. Vorticity that is only generated at the surface of the swimmer is confined to a narrow region close to the surface of the swimmer due to viscous dissipation by the fluid. The vorticity generated at the surface of the swimmer shifts its position in the same way as the surface distortions in a similar manner to the recirculation region.

5.6. Case 2, $s = 0.25$

In this case, the cycle time is reduced by a factor of 5 from the previous case and the dynamic viscosity (ν) remains the same as the previous case to achieve a scale number of 0.25. The axial velocities are plotted against the non-dimensionalized time (ωt) in Fig. 5.4b. The magnitude of the axial velocities are reduced by a factor of 2 when compared to the case at $s = 0.11$. The amplitude of the oscillations of the axial velocities at the monitor points is higher than the case at $s = 0.11$. This is because of the higher frequency of distortion of the swimmer as listed in the table 5.1. The simulation is done for 20 cycles of the swimmer. The force on the swimmer for 2 cycles is shown in Fig. 5.5b. The time average of the force on the swimmer over a cycle is 0. The unsteady Reynolds number (Re_ω) for this case as indicated in table 5.1 remains small (< 1) and comparable to that of *Opalina* for this case as well (see table 5.2). The Strouhal number (St) and the Reynolds number (Re) for the present case are given by equations 5.6 and 5.7. As given by equation 5.8, $StRe < 1$. Hence, in this case the Basset force and the added mass forces are not expected to affect the swimming velocity drastically.

$$St = \frac{fL}{U} = \frac{2\pi}{0.015 \cdot 0.5} \approx 837.75 \tag{5.6}$$

$$Re = \frac{UL}{\nu} = \frac{1 * 0.015}{100} \approx 1.5 \cdot 10^{-4} \tag{5.7}$$

$$StRe = 1.5 \cdot 10^{-4} \cdot 837.75 \approx 1.25 \cdot 10^{-1} \tag{5.8}$$

The combined-stroke-swimmer is in a diffusion dominated regime. At the surface of the swimmer, the distortions generate axial velocities of roughly 1 body length per second. This diffuses across the domain eventually reaching the points located in the far-field. The diffusive time scale is $t_d \sim \frac{L^2}{\nu}$. Thus, it takes around 12 cycles of the swimmer for a point located in the far-field (at 25R) to achieve a constant time-averaged swimming velocity. There is a difference in behaviour from the previous case ($s = 0.11$) as shown by the streamlines in the near field in section 5.10 by Fig. 5.10. The penetration of the recirculation region into the fluid is farther into the domain than the previous case. However, in the far field the streamlines remain parallel to each other. Contour plots of the vorticity in the near field of the swimmer have been shown in section 5.10 by Fig. 5.11. The vorticity is confined to a only narrow region close to the swimmer.

5.7. Case 3, $s = 0.79$

In this case the viscosity and the cycle time was reduced by a factor of 50 from the previous case. The cycle time remains the same as the one used for $s = 0.11$. The axial velocities are plotted against the non-dimensionalized time (ωt) in Fig. 5.4c. They are similar in magnitude to the axial velocities obtained in the case for $s = 0.11$. The simulation is done for 600 cycles of the swimmer. Since, the viscosity in this case is reduced by a factor of 50 from the previous case, it takes a long time ($\sim$ 600 cycles of the swimmer) for a point located in the far-field (25 R) , to attain a constant time-averaged velocity. The diffusive time scale for that point in this case corresponds to 125 cycles of the swimmer. As can be seen from the Fig. 5.5c, the oscillations in the axial velocities are absent. This is because of the lower viscosity used in this case. The effects of the surface distortions are not felt by the monitor points located in the fluid because of its reduced viscosity. Hence the oscillations in these points are absent. The force averaged over a period on the swimmer remains 0 as can be seen from Fig .5.5c.

The Strouhal number and the Reynolds number and their product for this case are given by equations 5.9,5.10 and 5.11. In this case $StRe \sim O(1)$. The contribution from the basset and and the added mass force is therefore expected to have a small effect on the velocity of the swimmer.

$$St = \frac{fL}{U} = \frac{2\pi}{0.04 \cdot 2.5} \approx 62.83 \tag{5.9}$$

$$Re = \frac{UL}{\nu} = \frac{1 * 0.04}{2} \approx 2 \cdot 10^{-2} \tag{5.10}$$

$$StRe = 2 \cdot 10^{-2} \cdot 62.83 \approx 1.2566 \tag{5.11}$$

Streamlines for the far field and the near field are shown in section by Fig. 5.12 and Fig. 5.13 respectively. A streamline and vorticity pattern (section 5.11, Fig. 5.14) similar to that of case 1

is observed. The vorticity generated at the surface of the swimmer is higher because the viscous dissipation is lesser in this case.

5.8. Case 4, $s = 3.03$

The viscosity in this case is reduced by two orders of magnitude from the case for $s = 0.79$. The axial velocities are plotted against the non-dimensionalized time (ωt) in Fig. 5.4d. The swimming velocity at this scale number is an order of magnitude lesser than the cases for $s = 0.11, 0.25$ and 0.79. The simulation is done for 2000 cycles of the swimmer. Inertia has a strong effect at this scale number. There are no oscillations in the plots of the axial velocities as shown in Fig.5.4d because of the extremely low viscosity used in this case. The force on the swimmer averaged over a period remains 0 as shown in Fig. 5.5d. The Strouhal number and the Reynolds number and their product for this case are given by equations 5.12,5.13 and 5.14. In this case $StRe > 1$. The contribution from the basset and the added mass force is therefore expected to have a non-negligible effect on the velocity of the swimmer.

$$St = \frac{fL}{U} = \frac{2\pi}{0.006 \cdot 10} \approx 104.719 \tag{5.12}$$

$$Re = \frac{UL}{\nu} = \frac{1 * 0.006}{0.034} \approx 176 \cdot 10^{-2} \tag{5.13}$$

$$StRe = 176 \cdot 10^{-2} \cdot 104.71 \approx 18.47 \tag{5.14}$$

Streamlines for the far field and the near field have been shown in section 5.12 by Fig. 5.15 & Fig. 5.16. Contour plots of the vorticity in the near field of the swimmer have been shown in section 5.12 by Fig. 5.17. Both show similar behaviour to the case at $s = 0.79$. All the cases are summarized in table 5.3.

Case number	$\nu(\frac{m^2}{s})$	$T_{cycle}(s)$	$\omega = \frac{2\pi}{T_{cycle}}$	$s = a\sqrt{\frac{\omega}{2\nu}}$	$Re_\omega = \frac{\omega L^2}{\nu}$	$\overline{U}\ (\frac{m}{s})$
1	100	2.5	2.51	0.11	0.0251	0.04
2	100	0.5	12.56	0.25	0.1256	0.017
3	2	2.5	2.51	0.79	1.255	0.04
4	0.034	10	0.6283	3.03	18.47	0.006
5	500	0.5	12.56	0.11	0.02512	0.45

Table 5.3: Input parameters and the numerically obtained mean swimming velocities (in the fifth column).

5.9. Streamlines and the vorticity for case 1

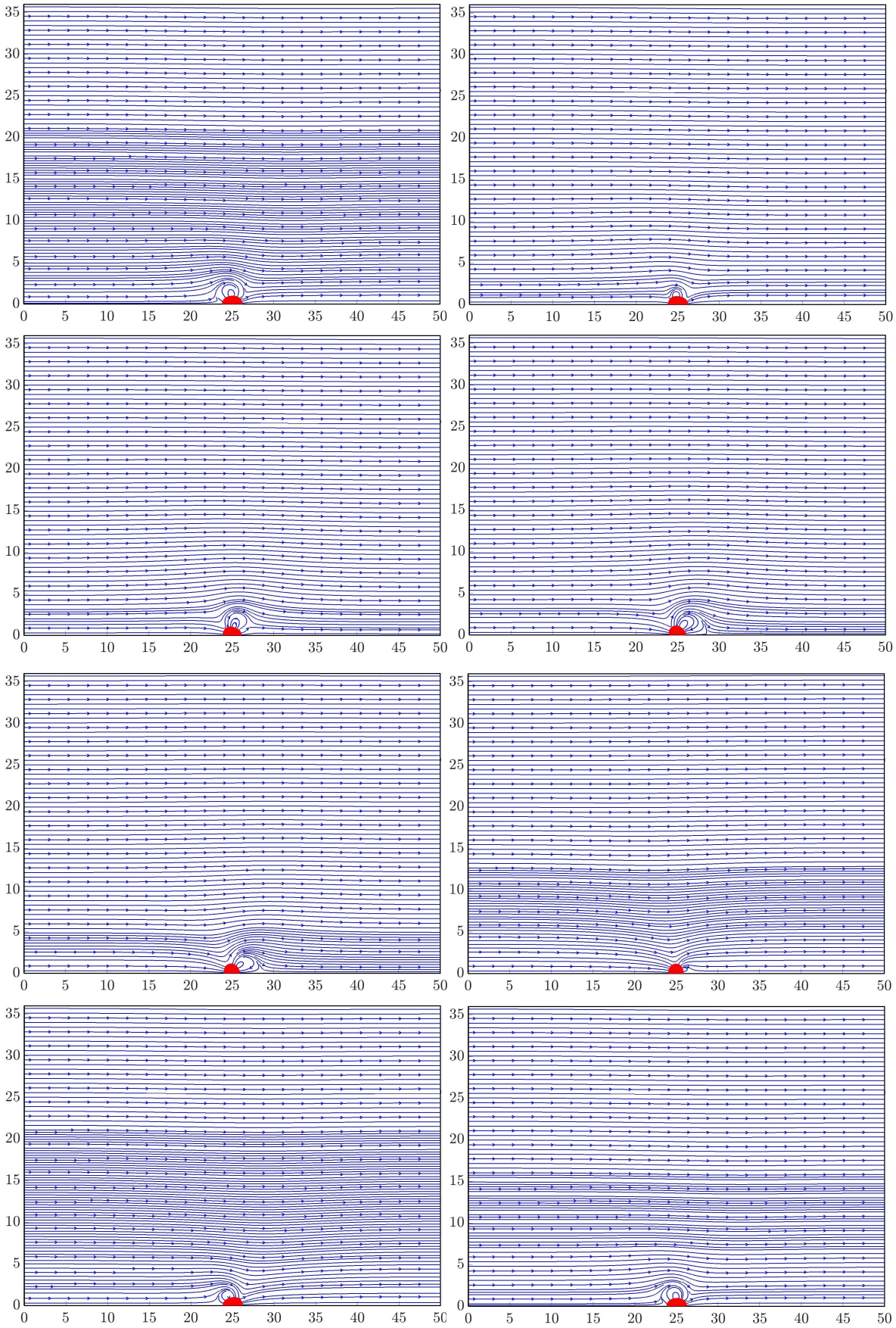

Figure 5.6: Streamlines in a co-moving frame for $s = 0.11$ in the far field of the combined-stroke -swimmer at 8 instants of the cycle. The sequence is to be read clockwise from top-left. The swimmer is moving to the left.

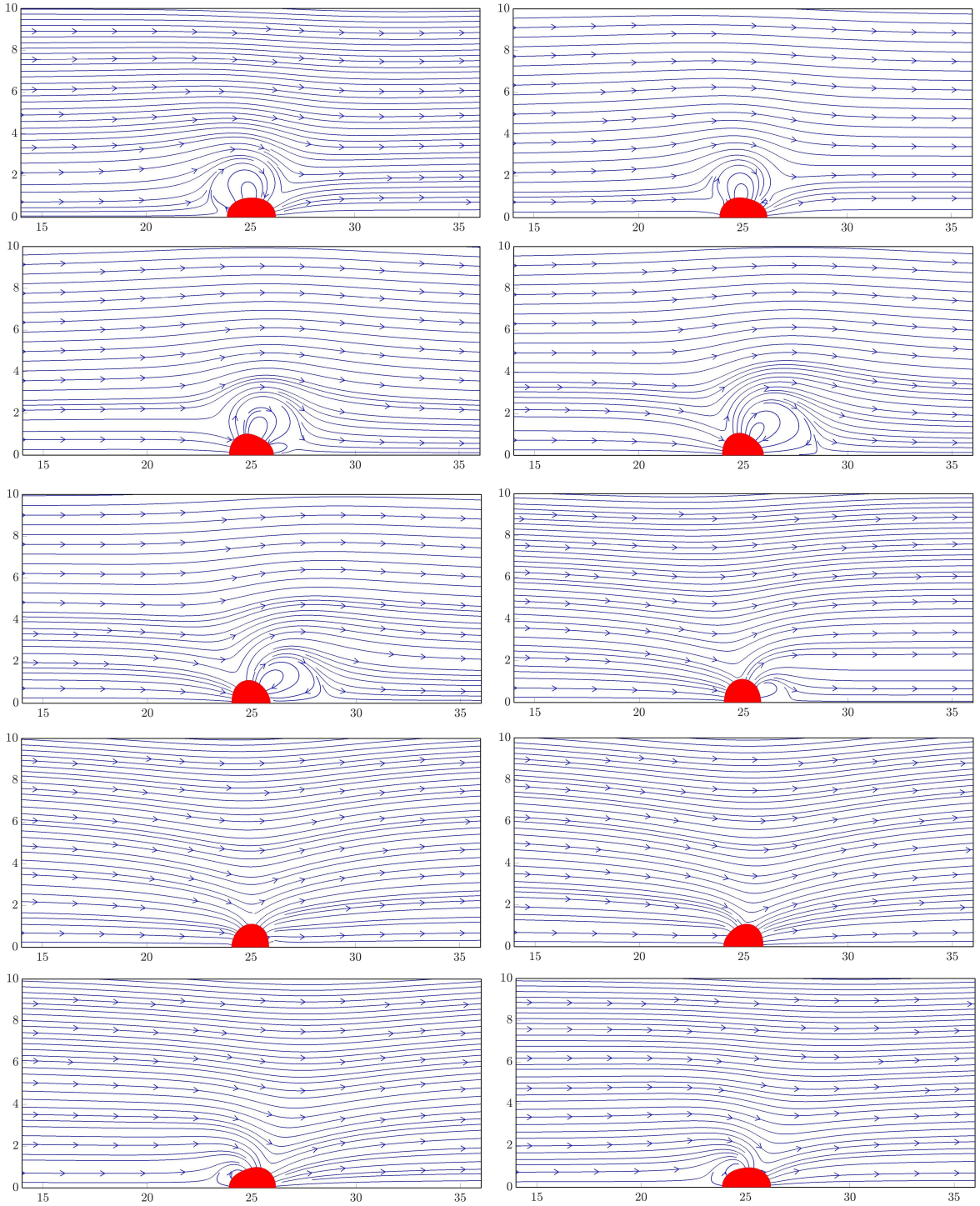

Figure 5.7: Streamlines in a co-moving frame for $s = 0.11$ in the near field of the combined-stroke -swimmer at 10 instants of its cycle. The sequence is to be read clockwise from top-left. The swimmer is moving to the left.

Contours of the vorticity for case 1

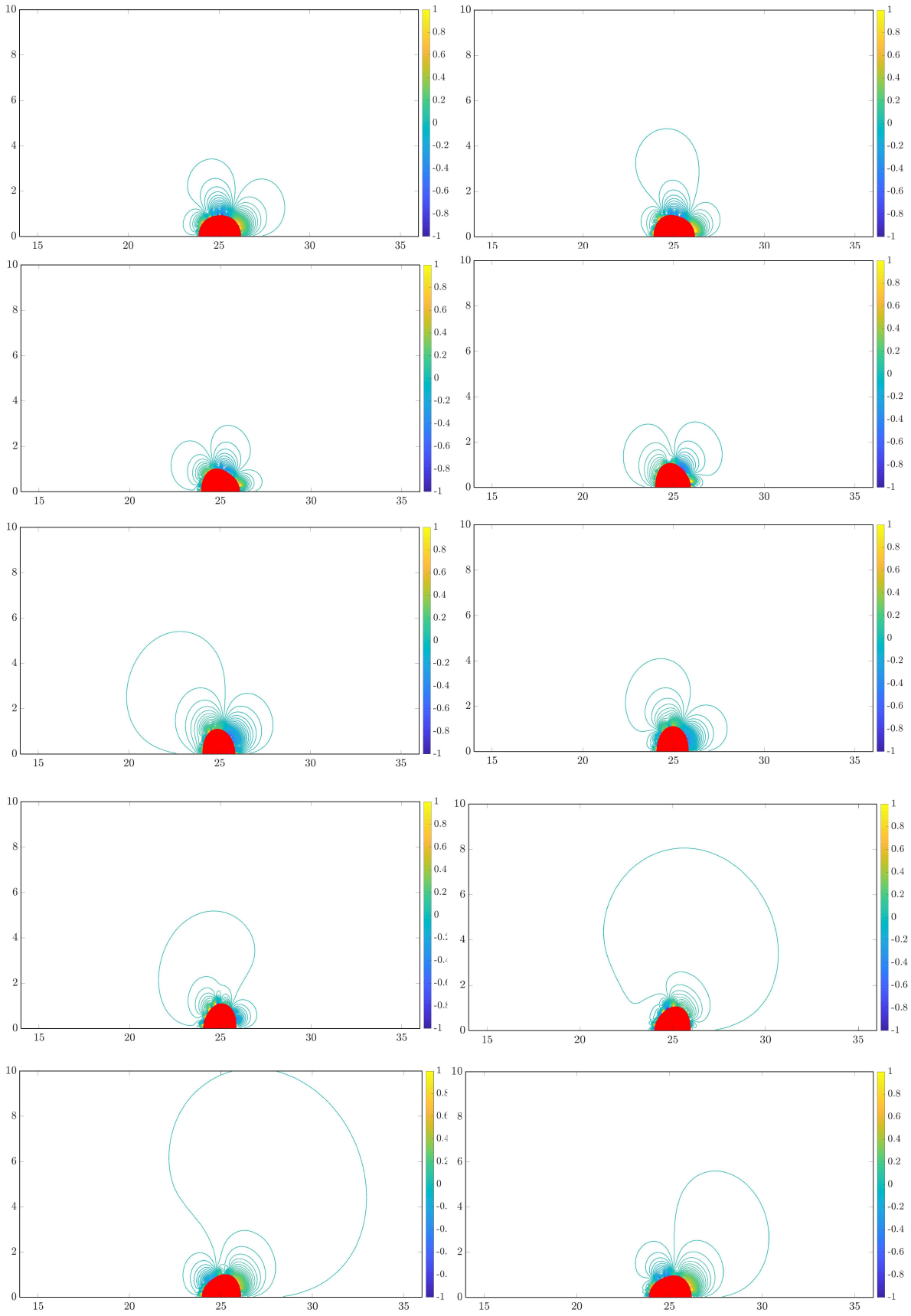

Figure 5.8: Contours of the vorticity for $s = 0.11$ in the near field of the combined-stroke-swimmer at 10 instants of its cycle. The vorticity is only confined to a narrow region close to the swimmer.

5.10. Streamlines and the vorticity for case 2

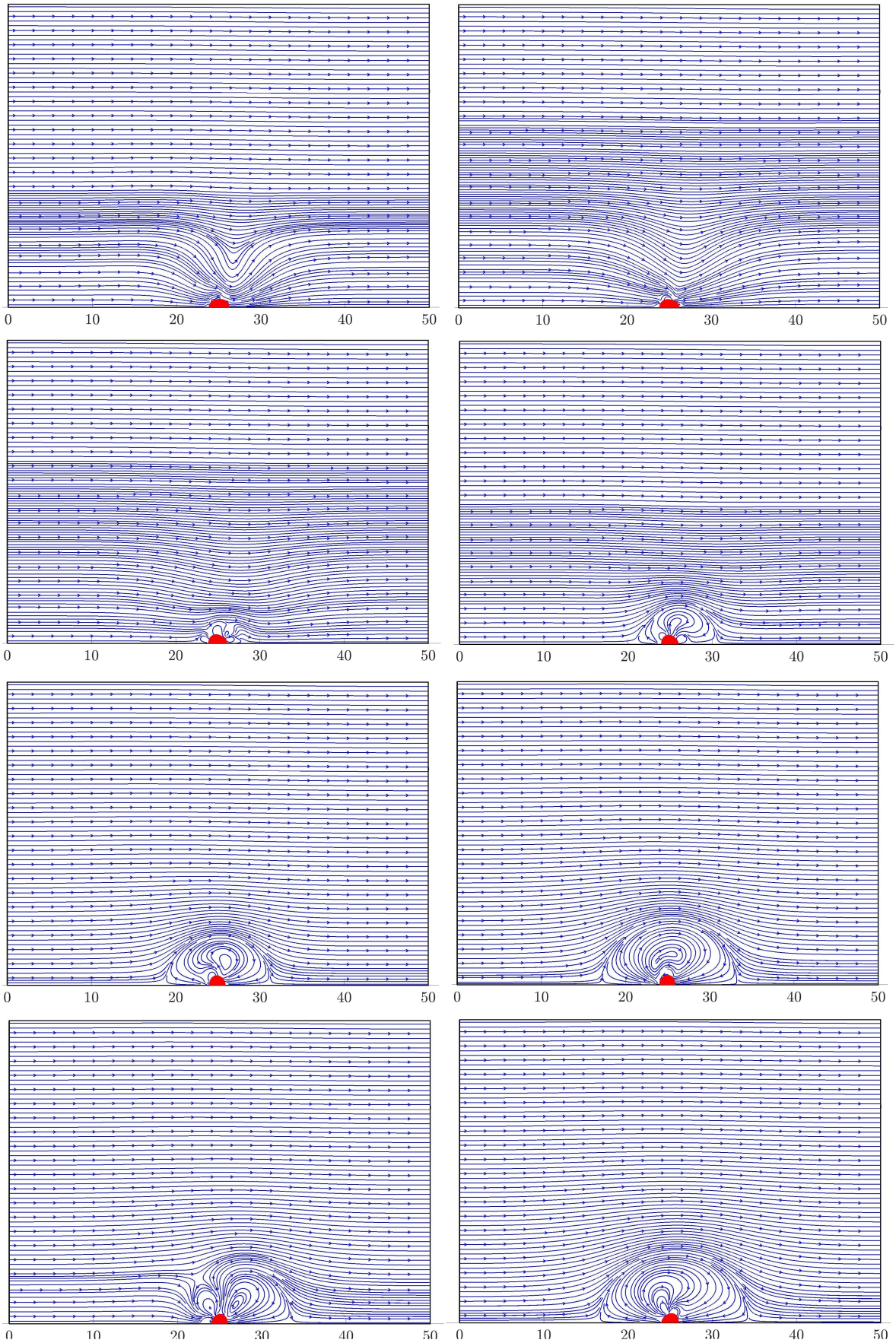

Figure 5.9: Streamlines in a co-moving frame for $s = 0.25$ in the far field of the combined-stroke-swimmer at 8 instants of its cycle. The sequence is to be read clockwise from top-left. The vertical axis (not shown in the figure) R^* ranges from 0 to 36R. The swimmer is moving to the left.

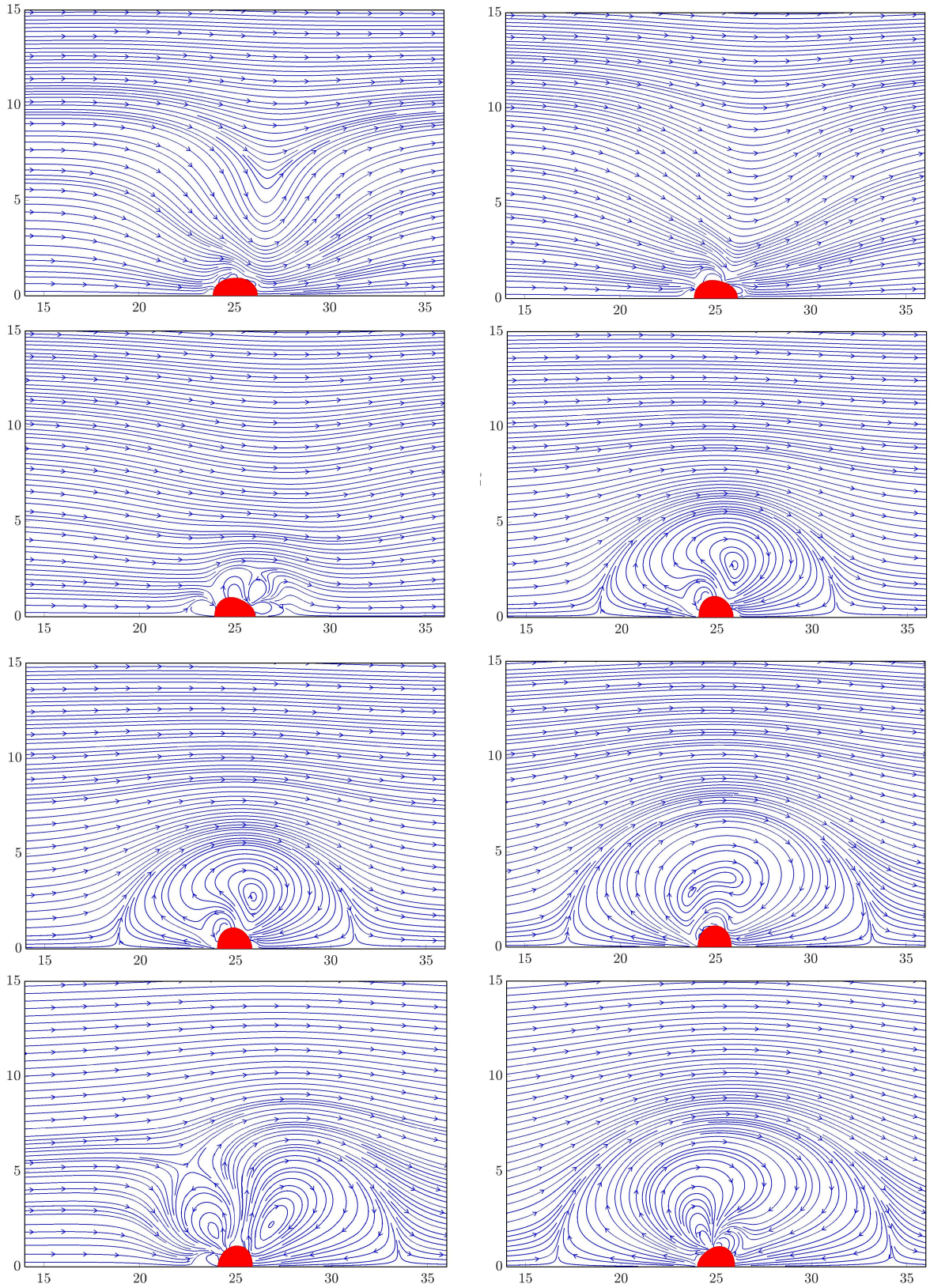

Figure 5.10: Streamlines in a co-moving frame for $s = 0.25$ in the near field of the combined-stroke-swimmer at 10 instants of its cycle equally spaced in time. The sequence is to be read clockwise from top-left. The swimmer is moving to the left.

Contours of the vorticity for case 2

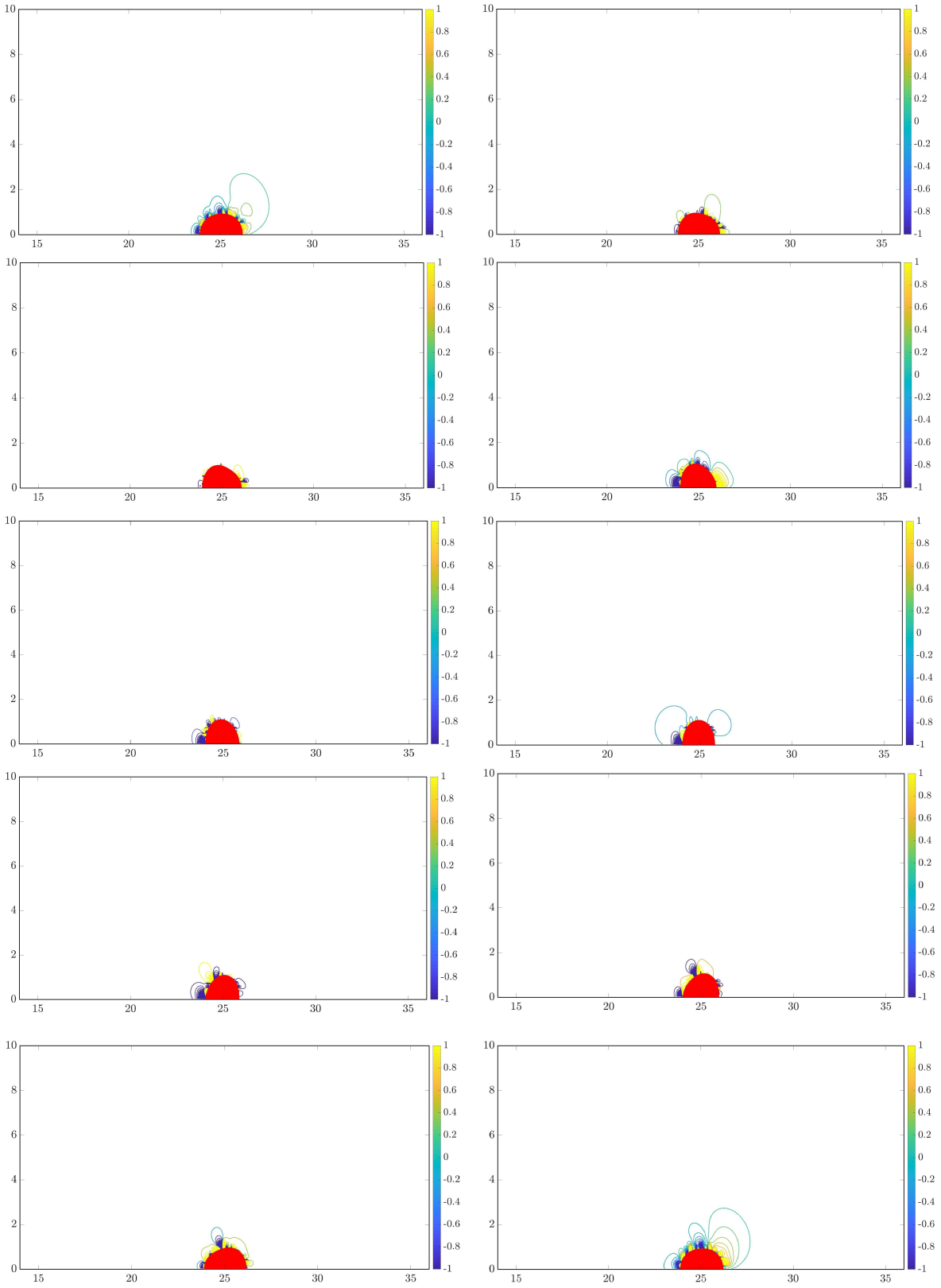

Figure 5.11: Contours of the vorticity for $s = 0.25$ in the near field of the combined-stroke-swimmer at 10 instants of its cycle.

5.11. Streamlines for case 3

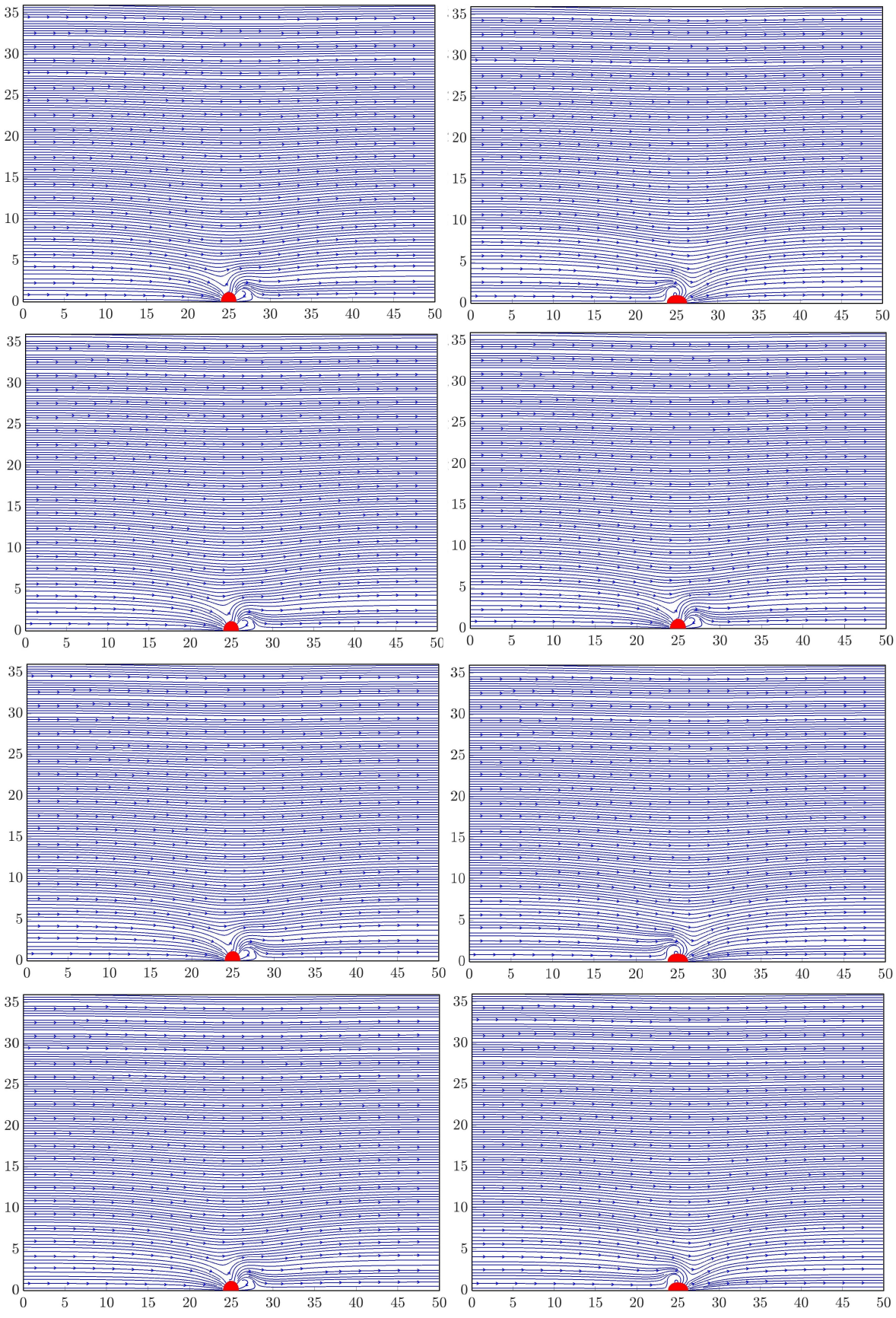

Figure 5.12: Streamlines in a co-moving frame for $s = 0.79$ in the far field of the combined-stroke-swimmer at 8 instants of its cycle. The sequence is to be read clockwise from top-left. The swimmer is moving to the left.

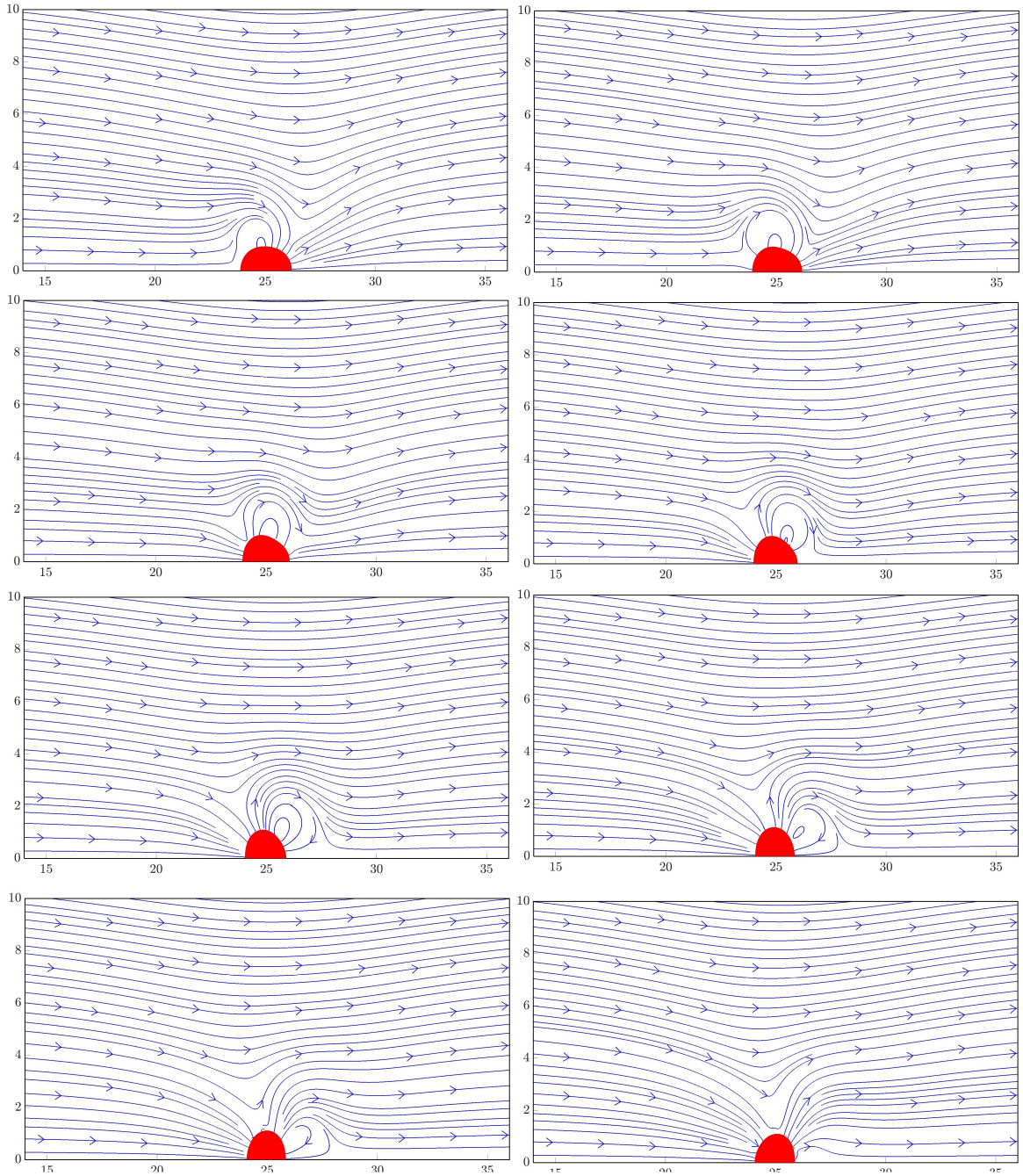

Figure 5.13: Streamlines in a co-moving frame for $s = 0.79$ in the near field of the combined-stroke-swimmer at 10 instants of its cycle. The sequence is to be read clockwise from top-left. The swimmer is moving to the left.

Contours of the vorticity for case 3

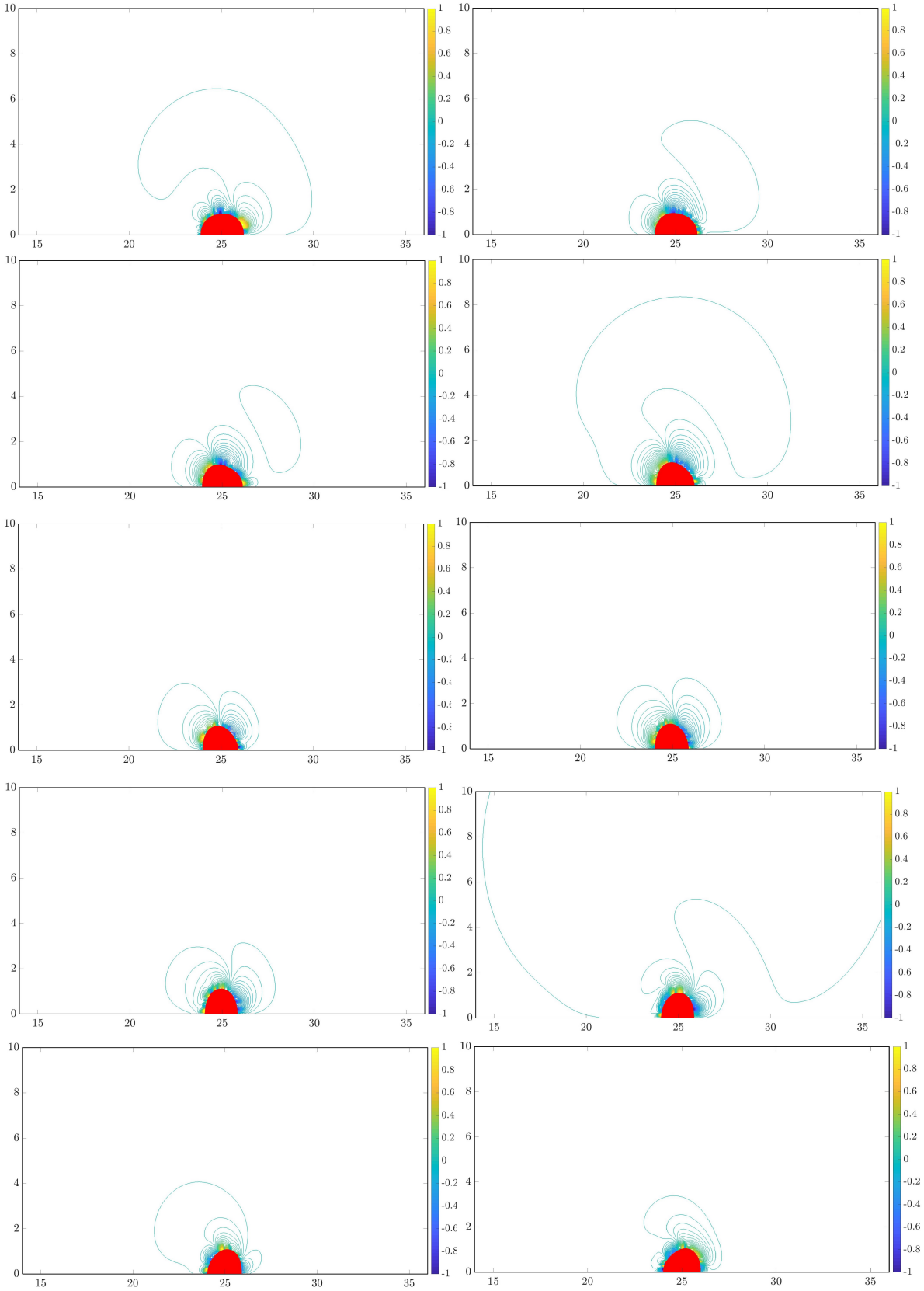

Figure 5.14: Contours of the vorticity for $s = 0.79$ in the near field of the combined-stroke-swimmer at 8 instants of its cycle.

5.12. Streamlines for case 4

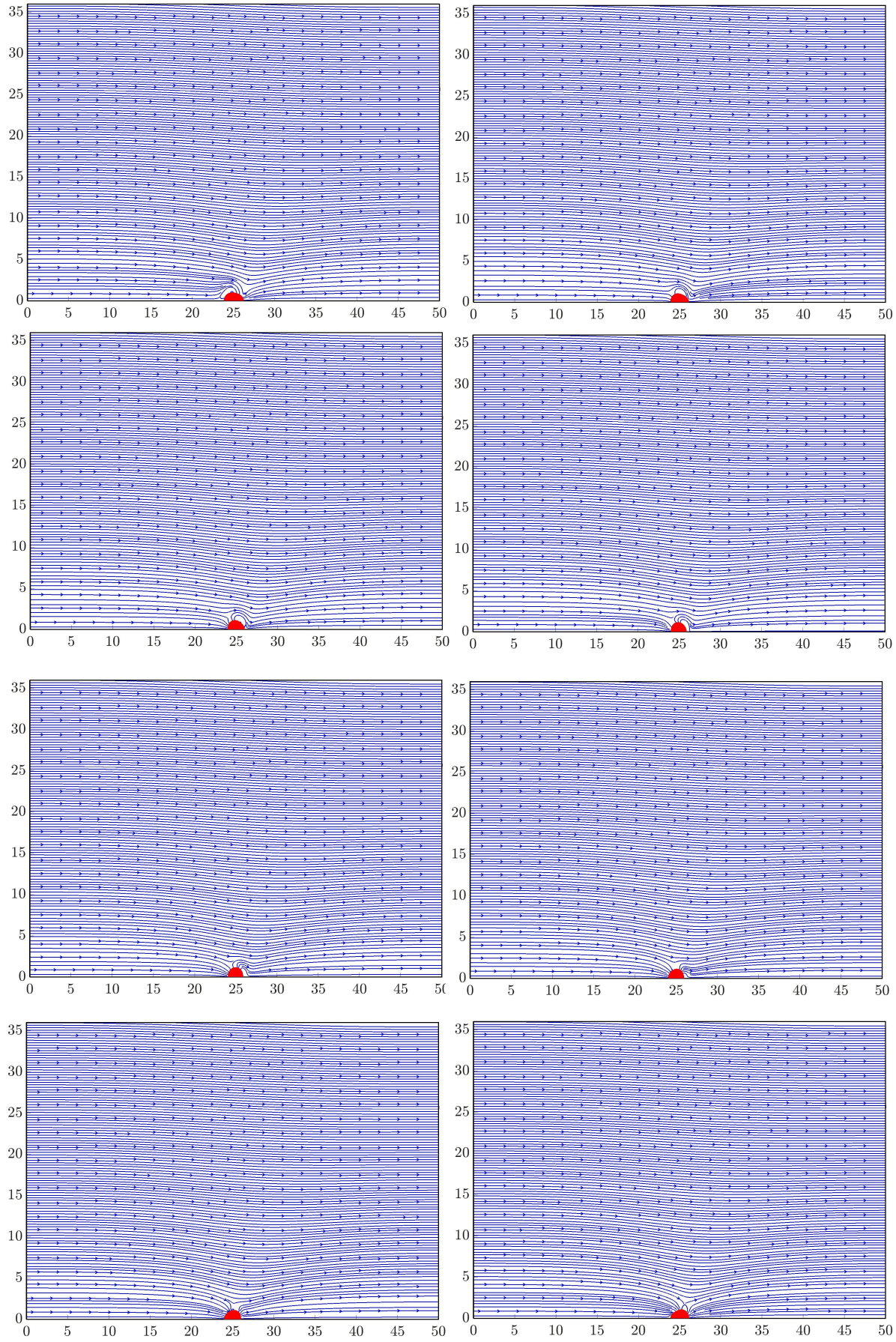

Figure 5.15: Streamlines in a co-moving frame for $s = 3.03$ in the far field of the combined-stroke-swimmer at 8 instants of its cycle. The sequence is to be read clockwise from top-left. The swimmer is moving to the left.

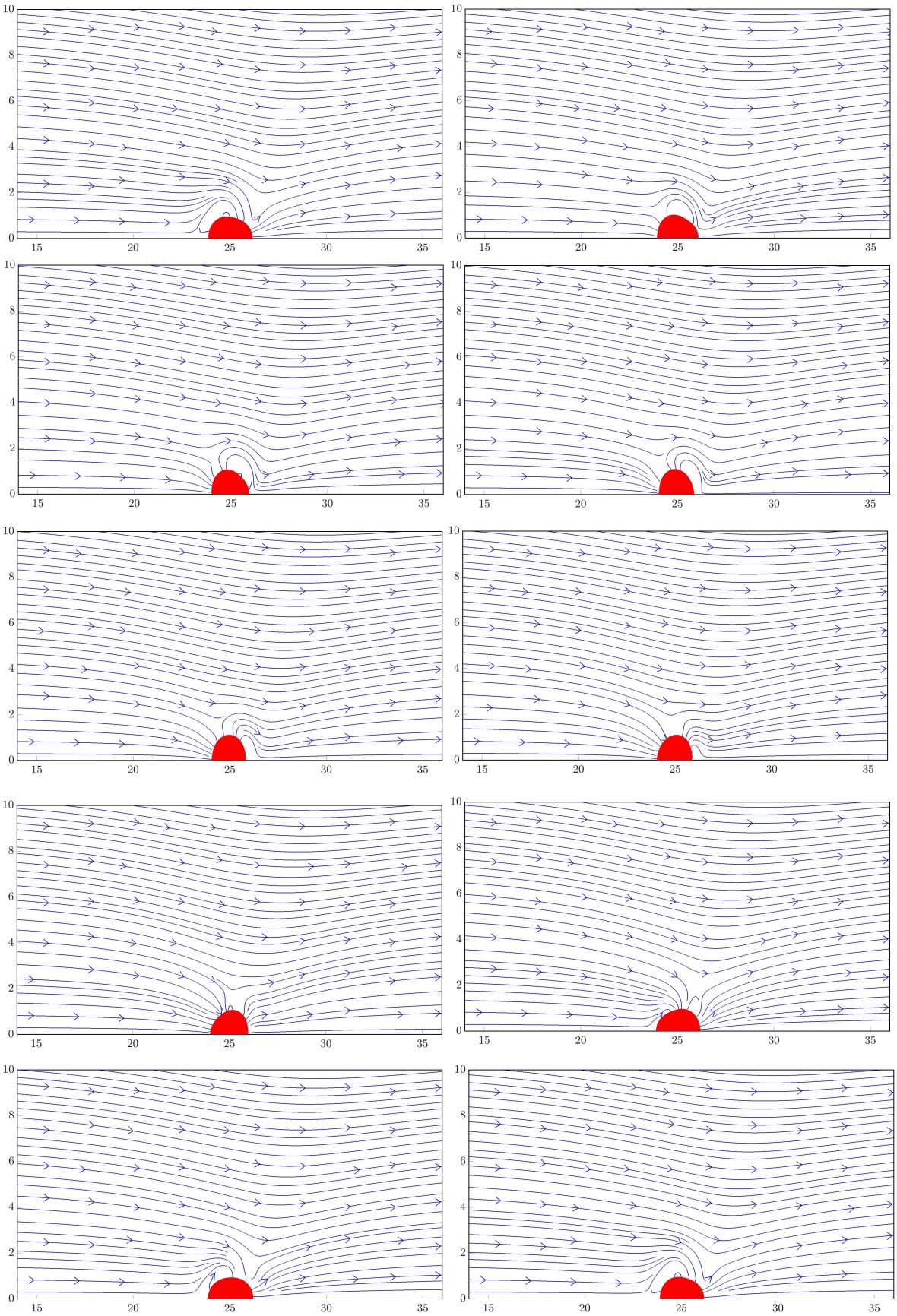

Figure 5.16: Streamlines in a co-moving frame for $s = 3.03$ in the near field of the combined-stroke-swimmer at 10 instants of its cycle. The sequence is to be read clockwise from top-left. The swimmer is moving to the left.

Contours of the vorticity for case 4

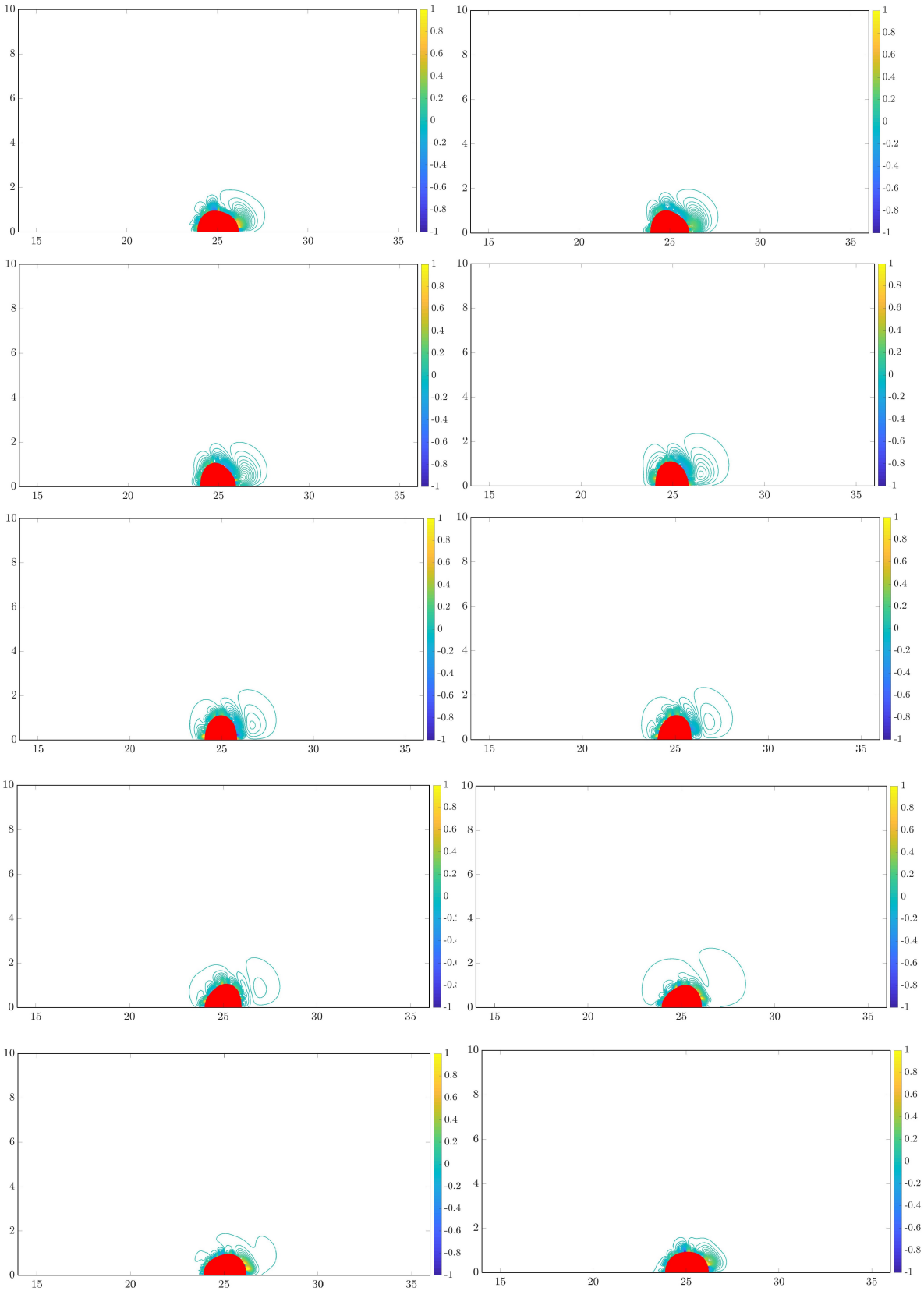

Figure 5.17: Contours of vorticity for $s = 3.03$ in the near field of the combined-stroke-swimmer at 10 instants of its cycle.

5.13. Discussion

A model as described by B.U. Felderhof [Felderhof, 2015] is used in this thesis to analyze the swimming of a spherically ciliated micro-organism. In the model, the deformations of a sphere are prescribed analytically using perturbation theory instead of making assumptions on the surface of the swimmer (see section 2.2). There are however certain nonphysical entities observed in the model and these are discussed below.

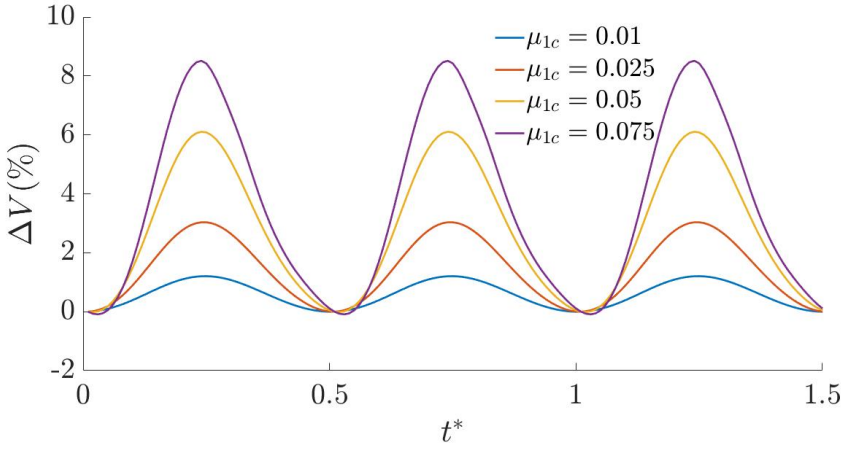

Figure 5.18: Variation in the volume for three cycles of the combined-stroke-swimmer at increasing values of the coefficient μ_{1c}. A cycle time (T_{cycle}) of 0.5s is chosen. t^* ($\frac{t}{T_{cycle}}$) denotes the non-dimensional time.

The combined-stroke-swimmer as given by B.U. Felderhof [Felderhof, 2015], deforms in such a way that its volume is not conserved. As shown in Fig. 5.18, the maximum deviation (≈8%) from its initial volume peaks at the middle of its cycle. This is only physical if there is an inflow/outflow across the envelope of the swimmer which is not the case, as the no-slip and the no-penetration boundary conditions on the envelope are assumed in the analytical model. The deviations in its volume are small (< 2%) but not negligible at lower values of the coefficient μ_{1c} (< 0.025) as shown in the figure. However, for small values of μ_{1c}, there is no discernible distortion of the sphere. As μ_{1c} tends to 0, the shape of the swimmer can be approximated as a steady sphere. The distorting sphere at various time instants for $\mu_{1c} = 0.01$ is shown in the figure 5.19.

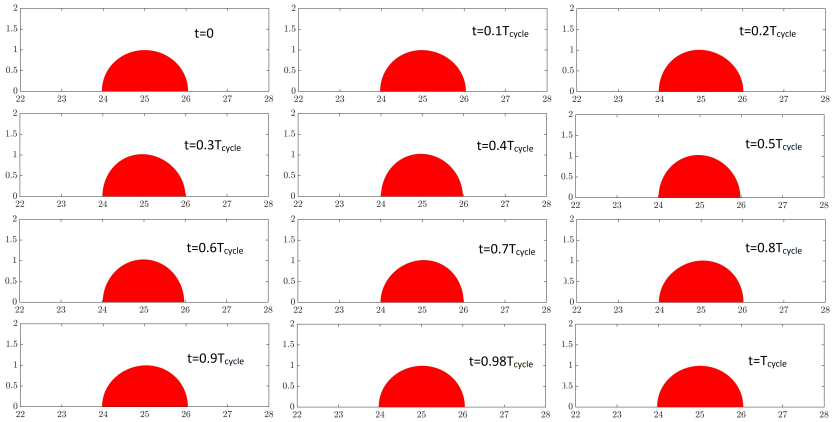

Figure 5.19: Deformations (one-half) of the combined-stroke-swimmer ($\mu_{1c} = 0.01$) as shown in red. The sequence is to be read clockwise from top-left. T_{cycle} in the frames denotes the cycle time of the swimmer. The Z and R axes (not shown in the figure) are in the horizontal and the vertical direction respectively

The variation in the volume does not reduce as the number of points defining the surface of the swimmer increases. This can be seen in Fig. 5.20.

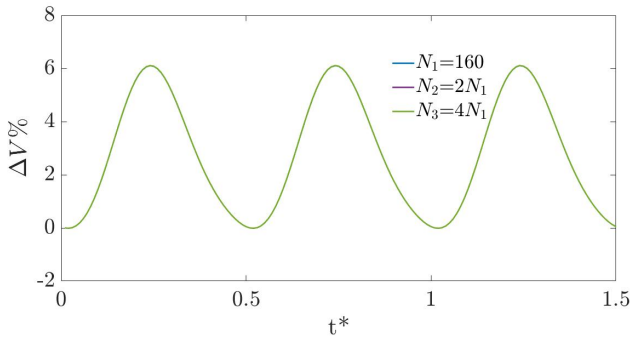

Figure 5.20: Variation in the volume for three cycles of the combined-stroke-swimmer ($\mu_{1c} = 0.05$) at increasing values of the number of points (N_1,N_2,N_3) used to define the surface of the swimmer. A cycle time (T_{cycle}) of 0.5s is chosen. t^* ($\frac{t}{T_{cycle}}$) denotes the non-dimensional time.

In the squirmer model that was developed by Blake [Blake, 1971] and Lighthill [Lighthill, 1952], the surface distortions were of the form given by equations 5.15 and 5.16

$$R = a[1 + \epsilon \sum_{n=2}^{N} \alpha_n(t) P_n cos(\theta_0)] \tag{5.15}$$

$$\theta = \theta_0 + \epsilon \sum_{n=1}^{N} \beta_n(t) V_n cos(\theta_0) \tag{5.16}$$

where R,θ denote the radial and polar coordinates of the oscillating surface of the sphere. ϵ represents the perturbations of the sphere. α_n, β_n correspond the modes of the radial and the tangential deformations of the sphere respectively. $P_n cos(\theta_0), V_n cos(\theta_0)$ correspond to the Legendre polynomials and their first derivatives respectively. α_0 corresponds to the swelling of the surface of an organism and is constrained to zero to ensure volume conservation. A similar effect is observed in the combined-stroke-swimmer in Fig. 5.18. The error (%) in the volume increases with increasing μ_{1c}, which could be related to the amount of the radial expansion in the sphere. The inclusion of the zeroth mode could affect the swimming velocities in the near field. Thus, by conserving the volume, the combined-stoke-swimmer could become suitable to model a ciliated micro-organism exhibiting Symplectic metachronism.

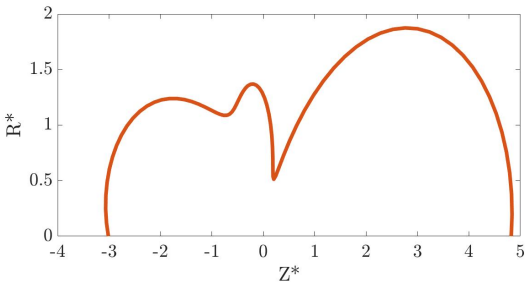

Figure 5.21: Deformation (one-half) of the combined-stroke-swimmer ($\mu_{1c} = 1$) at the start of its cycle.

In the case of an organism exhibiting Antiplectic metachronism, the no-slip and the no-penetration boundary conditions as used in the analytical model would also have to be modified. In addition to this, at a certain value of the coefficient $\mu_{1c} = 1$, the combined-stroke-swimmer is a highly distorted sphere and is of the form shown in Fig. 5.21. Cilia on the cell surface of a micro-organism are typically $\frac{1}{20}$

times their body-length. Hence, it is improbable that the envelope generated by connecting the tips of the cilia is of the form shown in the figure. However, this does not affect the flow pattern in the far field (>25R) of the swimmer. In the far field of the swimmer, the geometric shape of the swimmer becomes irrelevant.

The effects of inertia on the swimmer are discussed in the following section. Inertia reduces the mean swimming velocity of the combined-stroke-swimmer. This is very similar to the effect found in a puller. In addition to this, the time averaged force over a cycle for the combined-stroke-swimmer remains 0 for all the scale numbers chosen. The streamline and the vorticity patterns for all the scale numbers are similar with the exception for the case $s = 0.25$. The velocities generated at the surface of the swimmer die out to a nearly constant time averaged velcoity in the far field for all the scale numbers. The velocities in the far-field are computed in the reference frame of the swimmer. When the reference frame is switched back to the laboratory frame, the velocities in the far-field vanish. This shown for the two cases $s = 0.11$ and $s = 0.79$ in Fig. 5.22a and 5.22b respectively. This is in agreement with what is observed experimentally in the analysis of the swimming of micro-organisms.

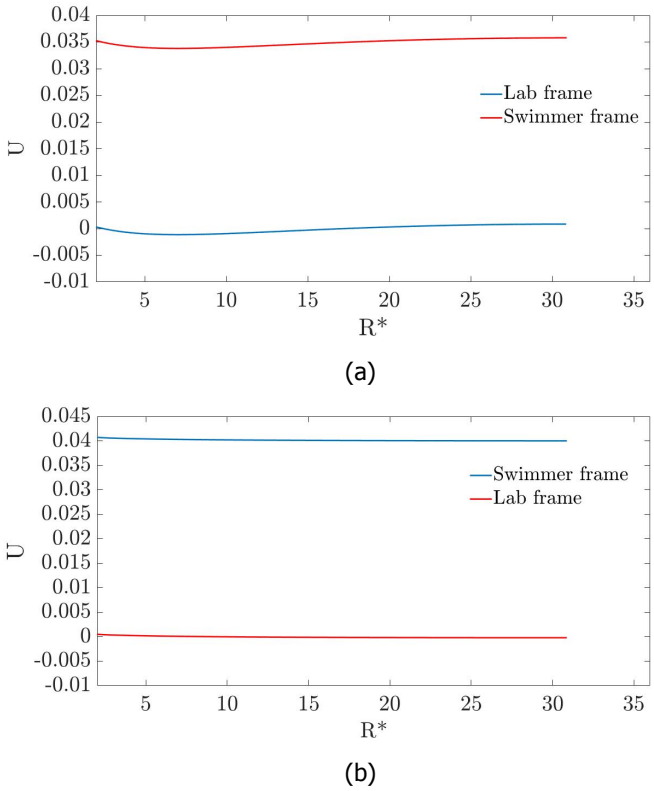

Figure 5.22: The plots of the axial velocity ($\frac{m}{s}$) along the vertical centerline (R^*) in the domain. The horizontal axis (R^*) begins at the surface of the swimmer. (a): The plot for the case $s = 0.11$; (b): The plot for the case $s = 0.79$.

For the scale number $s = 3.03$ in the analytical model, the mean swimming velocity of the swimmer is negative. In the numerical model, the swimming velocity is an order of magnitude lower than the cases $s = 0.11, 0.25, 0.79$ but positive. The non-dimesnional mean swimming velocities ($\frac{\overline{U}}{\omega a}$) obtained for case 1 and case 5 where the scale number is kept constant and the cycle time is changed by a factor of 5, differ by a factor of 2. This is shown in table A.4 in the Appendix A.9.

6

Conclusions and Recommendations

6.1. Conclusions

A model as described by B.U. Felderhof [Felderhof, 2015] is used in this thesis to analyze the swimming of a spherically ciliated micro-organism. In the model, the deformations of a sphere are prescribed analytically using perturbation theory instead of assuming the surface of the swimmer as a steady sphere (see section 2.2). Different swimmers can be obtained by using a different combination for the coefficients prescribing the deformations. The combined-stroke-swimmer used in this thesis is an example of this. The mean swimming velocity for the combined-stroke-swimmer is obtained in this work.

1. The mean swimming velocities for the combined-stroke-swimmer that are obtained numerically are more or less in agreement for the 2 cases of $s = 0.11$ and $s = 0.25$. At the scale number of $s = 3.03$, inertia seems to decrease the velocity of the swimmer though not in the same range of values as predicted by the analytical model.

2. The flow pattern obtained in the near field for the combined-stoke-swimmer for all the cases, differ significantly from the flow pattern obtained in the near-field of a swimming micro-organism by the widely used B1-B2 model. Hence, to capture the near-field effects (< 7R), prescribing the deformations of the sphere become important.

3. The combined-stroke-swimmer could be used to model a ciliated microorganism exhibiting symplectic metachronism by ensuring volume conservation

4. The accurate computation of the mass/volume fractions in the volume penalization scheme does not alleviate the problem of the spurious force oscillations (SFO's) as seen in other Immersed boundary methods.

6.2. Recommendations

The present work can be extended with the following recommendations.

1. The deformations could be modified to ensure volume conservation at all values for μ_{1c} ,making it more suited to model a ciliated micro-organism.
2. The volume penalization scheme can be modified to that of Vanella and Balaras [Vanella and Balaras, 2009] to remove the Spurious Force Oscillations (SFO's) that are seen in this IBM, and to enable a smoother coupling between the Lagrangian points describing the IB and the Eulerian grid.
3. The swimming efficiency and the mean dissipation for the combined-stroke-swimmer could be calculated and compared to the analytical solution.
4. It would be interesting to analyze the swimmer in a laboratory frame of reference. The decay of the velocity fields from the surface of the swimmer to the far-field can be more accurately captured. An estimate for the velocity of the swimmer that is imposed upon it in the laboratory frame of reference could be obtained from the analytical solution.
5. Apart from the combined-stroke-swimmer, the potential swimmer and the squirming swimmer could be simulated and their swimming velocities could be compared to the analytical model.

Bibliography

Amiralaei, M., Alighanbari, H., and Hashemi, S. (2010). An investigation into the effects of unsteady parameters on the aerodynamics of a low reynolds number pitching airfoil. *Journal of Fluids and Structures*, 26(6):979–993.

Behara, S. and Mittal, S. (2010). Flow past a circular cylinder at low reynolds number: Oblique vortex shedding. 22.

Blake, J. (1972). A model for the micro-structure in ciliated organisms. *Journal of Fluid Mechanics*, 55(1):1–23.

Blake, J. R. (1971). A spherical envelope approach to ciliary propulsion. *Journal of Fluid Mechanics*, 46(1):199–208.

Childress, S. (1981). *Mechanics of Swimming and Flying*. Cambridge Studies in Mathematical Biology. Cambridge University Press.

Coutanceau, M. and Bouard, R. (1977). Experimental determination of the main features of the viscous flow in the wake of a circular cylinder in uniform translation. part 1. steady flow. *Journal of Fluid Mechanics*, 79(2):231–256.

Cowan, M. K. (2018). *Microbiology: a systems approach*. McGraw-Hill.

de Graaf, J. and Stenhammar, J. (2017). Stirring by periodic arrays of microswimmers. *Journal of Fluid Mechanics*, 811:487–498.

Delmotte, B., Keaveny, E. E., Plouraboué, F., and Climent, E. (2015). Large-scale simulation of steady and time-dependent active suspensions with the force-coupling method. *Journal of Computational Physics*, 302:524–547.

Drescher, K., Dunkel, J., Cisneros, L. H., Ganguly, S., and Goldstein, R. E. (2011). Fluid dynamics and noise in bacterial cell–cell and cell–surface scattering. *Proceedings of the National Academy of Sciences*, 108(27):10940–10945.

Drescher, K., Goldstein, R. E., Michel, N., Polin, M., and Tuval, I. (2010). Direct measurement of the flow field around swimming microorganisms. *Physical Review Letters*, 105(16):168101.

Dunkel, J., Putz, V. B., Zaid, I. M., and Yeomans, J. M. (2010). Swimmer-tracer scattering at low reynolds number. *Soft Matter*, 6(17):4268–4276.

Elgeti, J., Winkler, R. G., and Gompper, G. (2015). Physics of microswimmers—single particle motion and collective behavior: a review. *Reports on progress in physics*, 78(5):056601.

Evans, A. A., Ishikawa, T., Yamaguchi, T., and Lauga, E. (2011). Orientational order in concentrated suspensions of spherical microswimmers. *Physics of Fluids*, 23(11):111702.

Felderhof, B. U. (2015). Stokesian spherical swimmers and active particles. , 91(4):043018.

Felderhof, B. U. and Jones, R. B. (2017). Swimming of a sphere in a viscous incompressible fluid with inertia. *Fluid Dynamics Research*, 49(4):045510.

Guirao, B. and Joanny, J.-F. (2007). Spontaneous creation of macroscopic flow and metachronal waves in an array of cilia. *Biophysical journal*, 92(6):1900–1917.

Hamel, A., Fisch, C., Combettes, L., Dupuis-Williams, P., and Baroud, C. N. (2011). Transitions between three swimming gaits in paramecium escape. *Proceedings of the National Academy of Sciences*, 108(18):7290–7295.

Ishikawa, T. (2009). Suspension biomechanics of swimming microbes. *Journal of The Royal Society Interface*.

Ishikawa, T. and Pedley, T. (2007). The rheology of a semi-dilute suspension of swimming model micro-organisms. *Journal of Fluid Mechanics*, 588:399–435.

Ishikawa, T., SIMMONDS, M. P., and PEDLEY, T. J. (2006). Hydrodynamic interaction of two swimming model micro-organisms. *Journal of Fluid Mechanics*, 568:119–160.

Kajishima, T., TAKIGUCHI, S., HAMASAKI, H., and MIYAKE, Y. (2001). Turbulence structure of particle-laden flow in a vertical plane channel due to vortex shedding. *JSME International Journal Series B Fluids and Thermal Engineering*, 44(4):526–535.

Kempe, T. and Fröhlich, J. (2012). An improved immersed boundary method with direct forcing for the simulation of particle laden flows. *Journal of Computational Physics*, 231(9):3663 – 3684.

Khaderi, S. N., den Toonder, J. M. J., and Onck, P. R. (2011). Microfluidic propulsion by the metachronal beating of magnetic artificial cilia: a numerical analysis. *Journal of Fluid Mechanics*, 688:44–65.

Lauga, E. and Powers, T. R. (2009). The hydrodynamics of swimming microorganisms. *Reports on Progress in Physics*, 72(9):096601.

Lee, J., Kim, J., Choi, H., and Yang, K.-S. (2011). Sources of spurious force oscillations from an immersed boundary method for moving-body problems. *Journal of computational physics*, 230(7):2677–2695.

Lemoine, A., Glockner, S., and Breil, J. (2017). Moment-of-fluid analytic reconstruction on 2d cartesian grids. *Journal of Computational Physics*, 328(Supplement C):131 – 139.

Lighthill, M. J. (1952). On the squirming motion of nearly spherical deformable bodies through liquids at very small reynolds numbers. *Communications on Pure and Applied Mathematics*, 5(2):109–118.

Linnick, M. N. and Fasel, H. F. (2005). A high-order immersed interface method for simulating unsteady incompressible flows on irregular domains. *Journal of Computational Physics*, 204(1):157–192.

Magar, V. and Pedley, T. J. (2005). Average nutrient uptake by a self-propelled unsteady squirmer. *Journal of Fluid Mechanics*, 539:93–112.

Mittal, R. and Iaccarino, G. (2005). Immersed boundary methods. *Annual Review of Fluid Mechanics*, 37(1):239–261.

Molina, J. J., Nakayama, Y., and Yamamoto, R. (2013). Hydrodynamic interactions of self-propelled swimmers. *Soft Matter*, 9(19):4923–4936.

Müller, U. and Videler, J. (1996). Inertia as a 'safe harbour': Do fish larvae increase length growth to escape viscous drag? 6:353–360.

Naganuma, T. (1996). Calanoid copepods: linking lower-higher trophic levels by linking lower-higher. *Mar Ecol Prog Ser*, 136:311–313.

NCFMF (1972). *Illustrated experiments in fluid mechanics: the NCFMF book of film notes*. MIT Press.

Niazi Ardekani, M., Abouali, O., Picano, F., and Brandt, L. (2018). Heat transfer in laminar couette flow laden with rigid spherical particles. *Journal of Fluid Mechanics*, 834:308–334.

Noor, D. Z., Chern, M.-J., and Horng, T.-L. (2009). An immersed boundary method to solve fluid–solid interaction problems. *Computational Mechanics*, 44(4):447–453.

O'Rourke, J., Chien, C.-B., Olson, T., and Naddor, D. (1982). A new linear algorithm for intersecting convex polygons. *Computer Graphics and Image Processing*, 19(4):384 – 391.

Osher, S. and Sethian, J. A. (1988). Fronts propagating with curvature-dependent speed: algorithms based on hamilton-jacobi formulations. *Journal of computational physics*, 79(1):12–49.

Park, J., Kwon, K., and Choi, H. (1998). Numerical solutions of flow past a circular cylinder at reynolds numbers up to 160. *KSME International Journal*, 12(6):1200–1205.

Pedley, T. J. (2016). Spherical squirmers: models for swimming micro-organisms. *IMA Journal of Applied Mathematics*, 81(3):488–521.

Peskin, C. S. (1972). Flow patterns around heart valves: a numerical method. *Journal of computational physics*, 10(2):252–271.

Purcell, E. M. (1977). Life at low reynolds number. *American Journal of Physics*, 45(1):3–11.

Qiu, T., Lee, T.-C., Mark, A. G., Morozov, K. I., Münster, R., Mierka, O., Turek, S., Leshansky, A. M., and Fischer, P. (2014). Swimming by reciprocal motion at low reynolds number. *Nature communications*, 5.

Sleigh, M. A. (1989). Adaptations of ciliary systems for the propulsion of water and mucus. *Comparative Biochemistry and Physiology Part A: Physiology*, 94(2):359 – 364.

Taira, K. and Colonius, T. (2007). The immersed boundary method: a projection approach. *Journal of Computational Physics*, 225(2):2118–2137.

Tamm, S. and Horridge, G. (1970). The relation between the orientation of the central fibrils and the direction of beat in cilia of opalina. *Proceedings of the Royal Society of London B: Biological Sciences*, 175(1040):219–233.

Taylor, G. (1951). Analysis of the swimming of microscopic organisms. In *Proceedings of the Royal Society of London A: Mathematical, Physical and Engineering Sciences*, volume 209, pages 447–461. The Royal Society.

Tillett, J. P. K. (1970). Axial and transverse stokes flow past slender axisymmetric bodies. *Journal of Fluid Mechanics*, 44(3):401–417.

Uhlmann, M. (2005). An immersed boundary method with direct forcing for the simulation of particulate flows. *Journal of Computational Physics*, 209(2):448–476.

Valentine, M. S., Rajendran, A., Yano, J., Weeraratne, S. D., Beisson, J., Cohen, J., Koll, F., and Van Houten, J. (2012). Paramecium bbs genes are key to presence of channels in cilia. *Cilia*, 1(1):16.

Vanella, M. and Balaras, E. (2009). A moving-least-squares reconstruction for embedded-boundary formulations. *Journal of Computational Physics*, 228(18):6617 – 6628.

Versteeg, H. and Malalasekera, W. (2007). *An Introduction to Computational Fluid Dynamics: The Finite Volume Method*. Pearson Education Limited.

Wang, S. and Ardekani, A. (2012a). Inertial squirmer. *Physics of Fluids*, 24(10):101902.

Wang, S. and Ardekani, A. (2012b). Unsteady swimming of small organisms. 702.

Zaidi, A. A., Tsuji, T., and Tanaka, T. (2014). A new relation of drag force for high stokes number monodisperse spheres by direct numerical simulation. *Advanced Powder Technology*, 25(6):1860 – 1871.

Zheng, H., Shi, B., Yu, Q., and Zhao, E. (2016). Numerical study of flow over periodically deforming circular cylinder. *Computers Fluids*, 136:348 – 353.

Zöttl, A. and Stark, H. (2016). Emergent behavior in active colloids. *Journal of Physics: Condensed Matter*, 28(25):253001.

A

Appendix A

A.1. Differences between Symplectic and Antiplectic metachrony

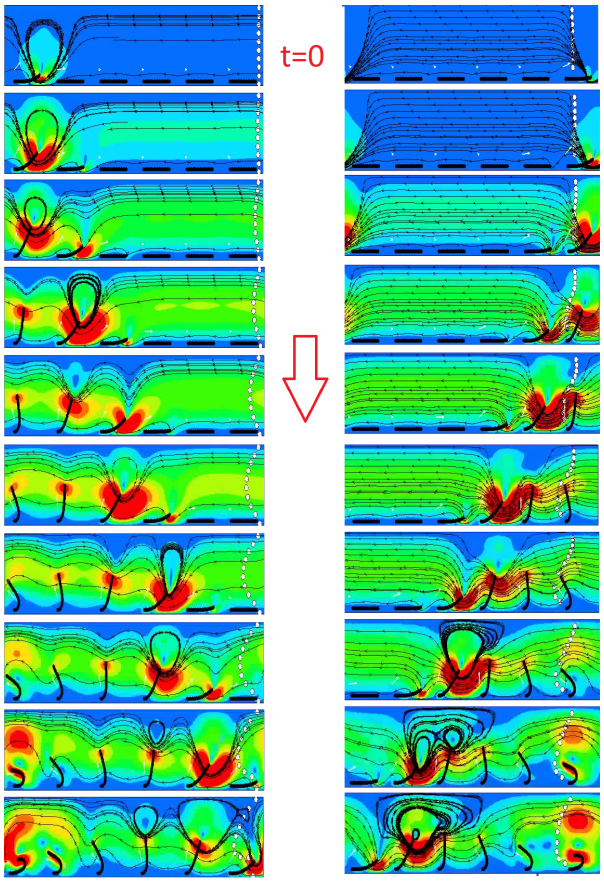

Figure A.1: Symplectic and Antiplectic metchrony. Symplectic metachrony is shown to the right, while Antiplectic metachrony is shown to the left. The travelling wave generated by the cilia is in the direction of the effective stroke in Symplectic metachrony and the vice versa is true in Antiplectic metachrony. The sequence of images is to be read from the top to bottom. The white dots denote particles to indicate the fluid motion. Reproduced from [Khaderi et al., 2011].

A.2. Accuracy in computation of the mass fractions

The test for the mass fractions for the polyogon clipping algorithm have been done on a sphere of radius 0.5 and a grid with resolution $\Delta z = \Delta r = \frac{D}{16}$. Kempe et al. [Kempe and Fröhlich, 2012] have done the same test on a sphere of radius 0.8. The error obtained from the present work is compared to their work in table A.1. The time spent in the computation of the mass fractions through this technique amounts to only 4% of the total time spent in the volume penalization algorithm.

Method	Actual volume	Numerical volume	Error (%)
Level-Set-Method [Kempe and Fröhlich, 2012]	2.144	2.133	0.5
Polygon clipping	0.523	0.523	-1.21 e^{-4}

Table A.1: The error in computation of the volume for Polygon clipping and the the Level set method that is traditionally used.

A.3. Coupling the deforming object to the Cartesian grid.

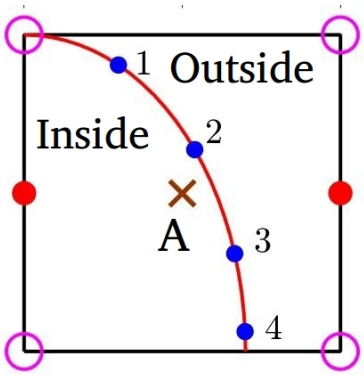

Figure A.2: The points shown in blue are the Lagrangian points that describe the deforming object shown by the red line. The grid cell bordered in black is centered at the u velocity (horizontal component) point *A*. The v velocity (vertical component) points are shown by the pink hollow circles. The u velocity at point *A* gets a contribution from the solid (inside) and the outside (fluid) through the solid volume fraction α as given by equation A.1. The contributions from the inside and outside are α and $1-\alpha$ respectively.

Fig. A.2 denotes the u,v and the pressure points of an interfacial cell. The interfacial cells are identified as those that have mass fractions between 0 and 1. The deforming object is described by the Lagrangian points as shown in blue in the figure. Since the deformations of the swimmer are both axial and radial, each Lagrangian point describing the swimmer has a different velocity. All the points 1,2,3 and 4 as shown in the Fig. A.2 have different axial and radial velocities respectively. Hence, the volume penalization scheme as defined in the section 3.6 is slightly modified **only** in the computation of the forcing term at point A ($f_A^{n+\frac{1}{2}}$). This is explained in the current section. The second prediction velocity at A is computed as usual as given by equation A.1. The forcing term is computed as given by equation A.2.

$$u_A^{**} = u_A^{*} + \Delta t f_A^{n+1/2} \tag{A.1}$$

where,

$$f_A^{n+1/2} = \alpha_A^{n+1}\left(\frac{U_{solid}^{n+1} - u_A^{*}}{\Delta t}\right) \tag{A.2}$$

where U_{solid}^{n+1} is given by the velocity of the last Lagrangian point in the grid cell.

The second prediction velocity at point A (u_A^{**}) gets a contribution from the solid and the fluid and through the volume fractions as given by equation A.1. In case of the deforming object, the solid velocity U_{solid}^{n+1} in equation A.2 is given by the velocity of the last Lagrangian point inside the grid cell (shown by point *4* in the figure). The differences in the solid velocities (U_{solid}^{n+1}) between the Lagrangian points that describe the swimmer reduce as the grid cells become smaller in size and the number of Lagrangian points that describe the swimmer increase. Hence, the contribution to u_A^{**} from point 1 would be the same as that of point 4. The velocities of the Lagrangian points (U_{solid}^{n+1}) at 1,2,3 and 4 are computed from their displacements in a time-step (Δt) as given by equations A.3 and A.4. This is first-order accurate in time.

$$U_{solid}^{n+1} = \frac{z^{n+1} - z^n}{\Delta t} \tag{A.3}$$

$$V_{solid}^{n+1} = \frac{r^{n+1} - r^n}{\Delta t} \tag{A.4}$$

where U_{solid}^{n+1} and V_{solid}^{n+1} denote the axial and radial velocities at the new time level respectively and z, r denote the coordinates of the Lagrangian points describing the swimmer respectively. $n+1, n$ indicate the new and the old time level respectively. Δt denotes the time-step.

A.4. C_D and C_L for two different grids.

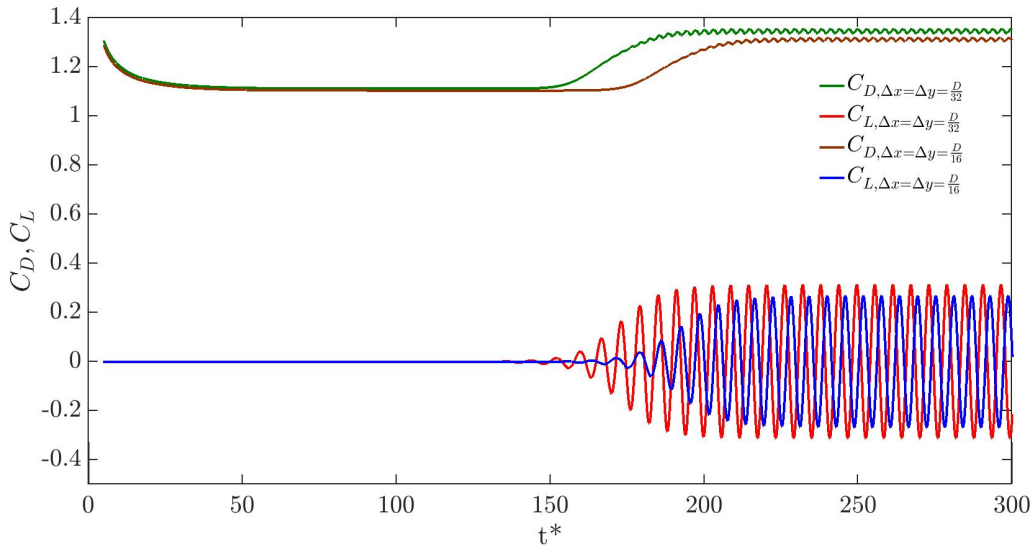

Figure A.3: The plots of the drag and the lift coefficients against the non-dimensional time (t^*) for a coarse grid ($\Delta x = \Delta y = \frac{D}{16}$) shown by the brown ($C_D$) and the blue ($C_L$) lines and a fine grid ($\Delta x = \Delta y = \frac{D}{32}$) shown by the green ($C_D$) and the red ($C_L$) lines.

The plots of the drag and the lift coefficients for a coarse grid and a fine grid which have 16 and 32 grid points over the cylinder diameter respectively are shown in the Fig. A.3. The mean and the peak values for the drag and the lift coefficient respectively have been tabulated in table A.2.

Grid	$\overline{C_D}$	$C_{L,peak}$
Coarse	1.25	0.26
Fine	1.34	0.31
Body conforming grid [Park et al., 1998]	1.33	0.33

Table A.2: The mean value of the drag and the peak value of the lift coefficient as obtained from the code using a coarse and a fine grid. The values in the last row are obtained from a code that uses a body conforming grid.

A.5. Comparison of the results obtained from the binary and the non-binary volume fractions.

The velocity and the pressure profiles obtained from the code for the steady flow over a cylinder at $Re = 40$, by setting the volume fractions to binary have been compared with those obtained by setting the volume fractions to non-binary in Fig. A.4. Both the simulations are done with the same grid resolution ($\Delta x = \Delta y = \frac{D}{32}$) and a time step $\Delta t = 0.01$ with *CFL*=0.32. The drag and the lift coefficients are tabulated in table A.3.

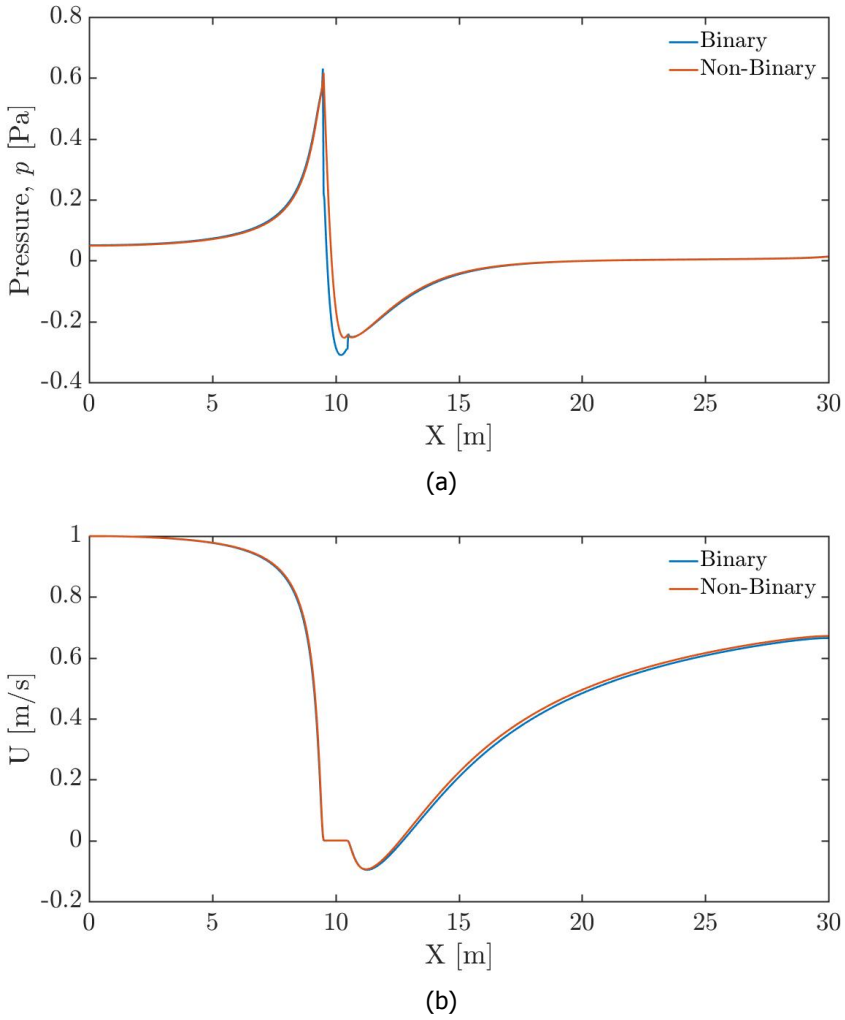

Figure A.4: Comparison of the pressure and the u velocity profiles obtained from the binary and the non-binary volume fractions. The pressure as predicted by the binary volume fractions is lower at the back end of the cylinder. ($X = 10.5m$)

Volume fractions	C_D
Binary	1.58
Non-Binary	1.56
[Taira and Colonius, 2007]	1.55

Table A.3: The drag and the lift coefficients obtained from the binary and the non-binary volume fraction. The drag obtained in the former differs from the latter by 1.2%.

A.6. Spurious force oscillations in the case of the binary volume fractions

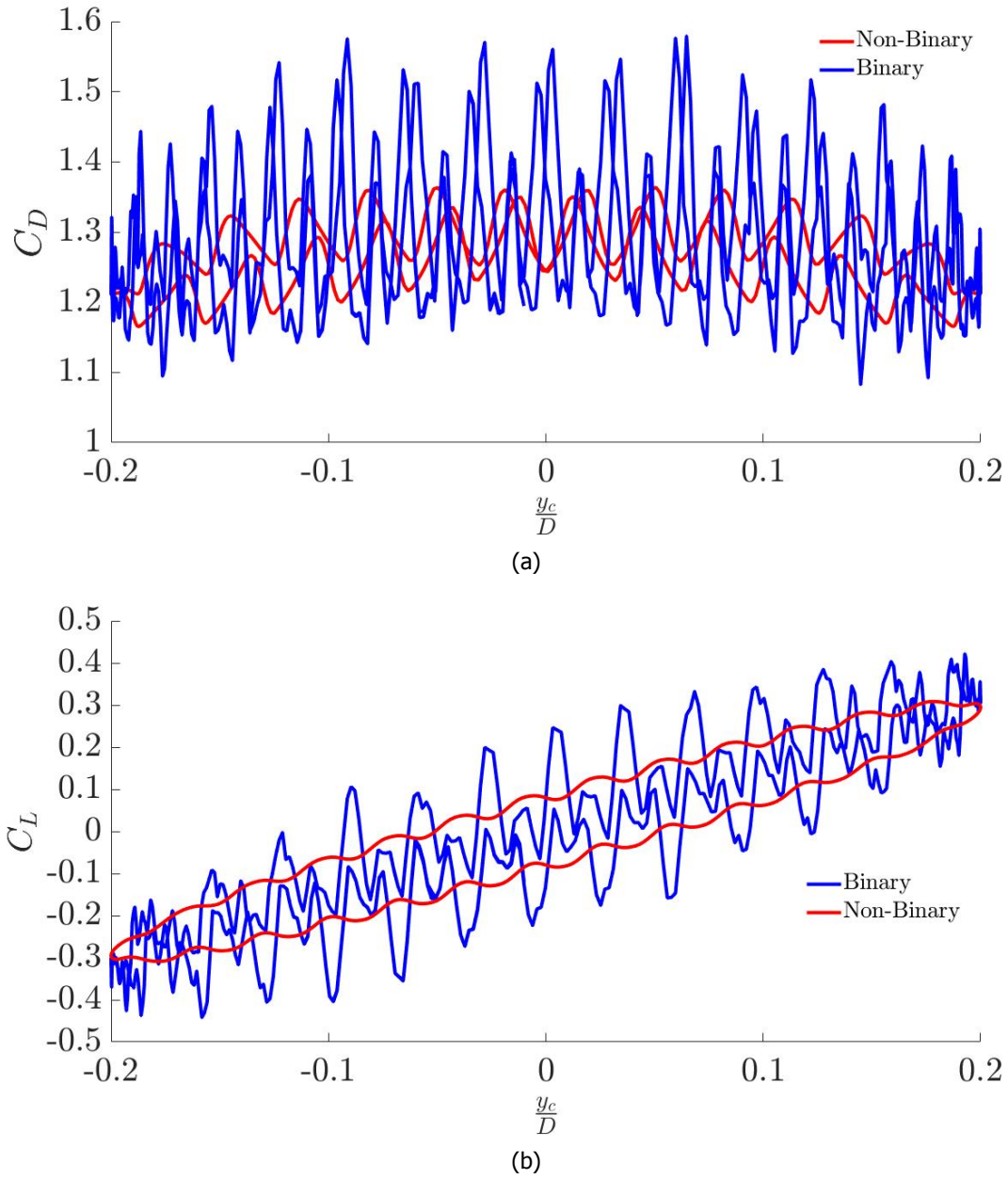

Figure A.5: Comparison of the drag and the lift coefficients obtained from the code with binary and non-binary volume fractions respectively. (a): Spurious force oscillations in the drag coefficient; (b): Spurious force oscillations in the lift coefficient. The red and blue lines indicate the curves that are obtained from the non-binary volume fraction and the binary volume fraction respectively. y_c is the centre of the cylinder, D is the diameter of the cylinder.

The spurious force oscillations in the drag and the lift coefficients that are obtained as a result of setting the volume fractions to binary, are shown by the blue curves in Fig. A.5. An accurate computation of the volume fractions helps in reducing the spurious force oscillations but does not remove it completely as seen by the red curves in the figure.

A.7. Flow over a deforming cylinder

The flow over a deforming cylinder using the scheme given in the Appendix A.3 is simulated. The sequence of the distortion shown in Fig. A.6. The radius in the lateral direction is varied sinusoidally as given by equation A.5. The deformations are such that the area is conserved. Hence, the radius in the longitudinal direction can be obtained as given by equation A.6.

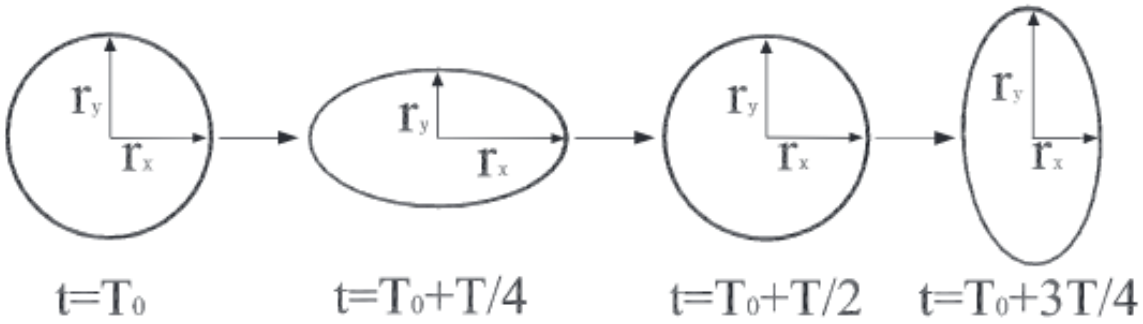

Figure A.6: Sequence of the distortion for the deforming cylinder. Reproduced from [Zheng et al., 2016].

$$r_y = R_0 - Asin(2\pi f_e t) \tag{A.5}$$

$$r_x r_y = R_0^2 \tag{A.6}$$

where, R_0 is the intial radius of the cylinder, A is the amplitude of the deformation of the cylinder, f_e is the excitation frequency. The simulations are done for a Reynolds number $Re = 200$ at $A = 0.1R$ for a frequency $f_e = 0.75f_0$. Here f_0 denotes the natural frequency of vortex shedding at $Re = 200$. The simulation is done for $\Delta x = \Delta y = \frac{D}{32}$ and a fixed Δt such that the *CFL <1*. The drag coefficient obtained as a function of time is shown in the Fig. A.7. The 2S mode of vortex shedding is observed at this frequency as shown in the Fig. A.8.

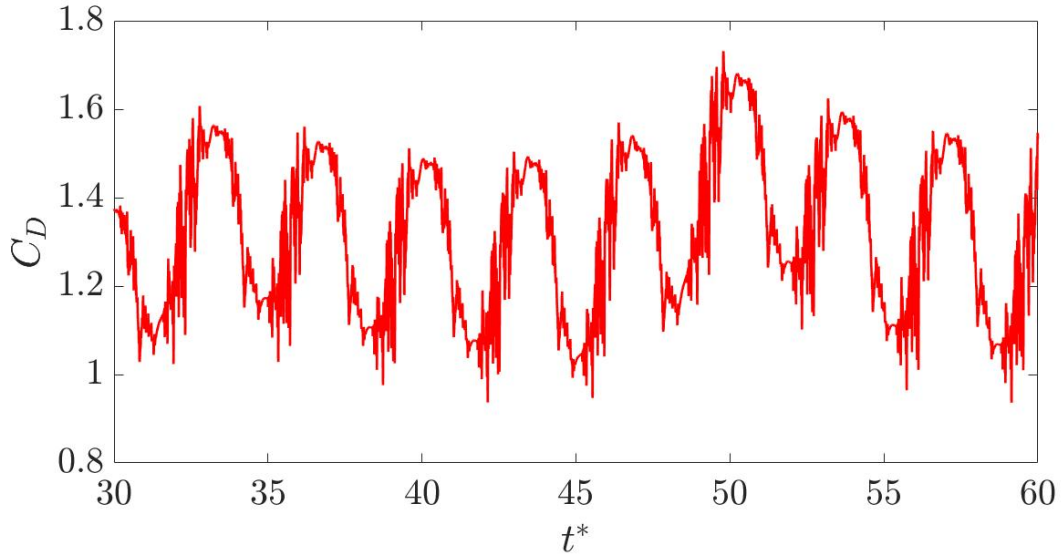

Figure A.7: The drag that is obtained from the code as function of the non-dimensional time t^* for the distorting cylinder at $Re = 200, f_e = 0.75f_0, A = 0.1R$. Spurious force oscillations are observed in this case as well.

The mean value of the drag obtained from the current simulation for $Re = 200, f_e = 0.75f_0, A = 0.1R$, showed a difference of 6% with the value reported in the [Zheng et al., 2016].

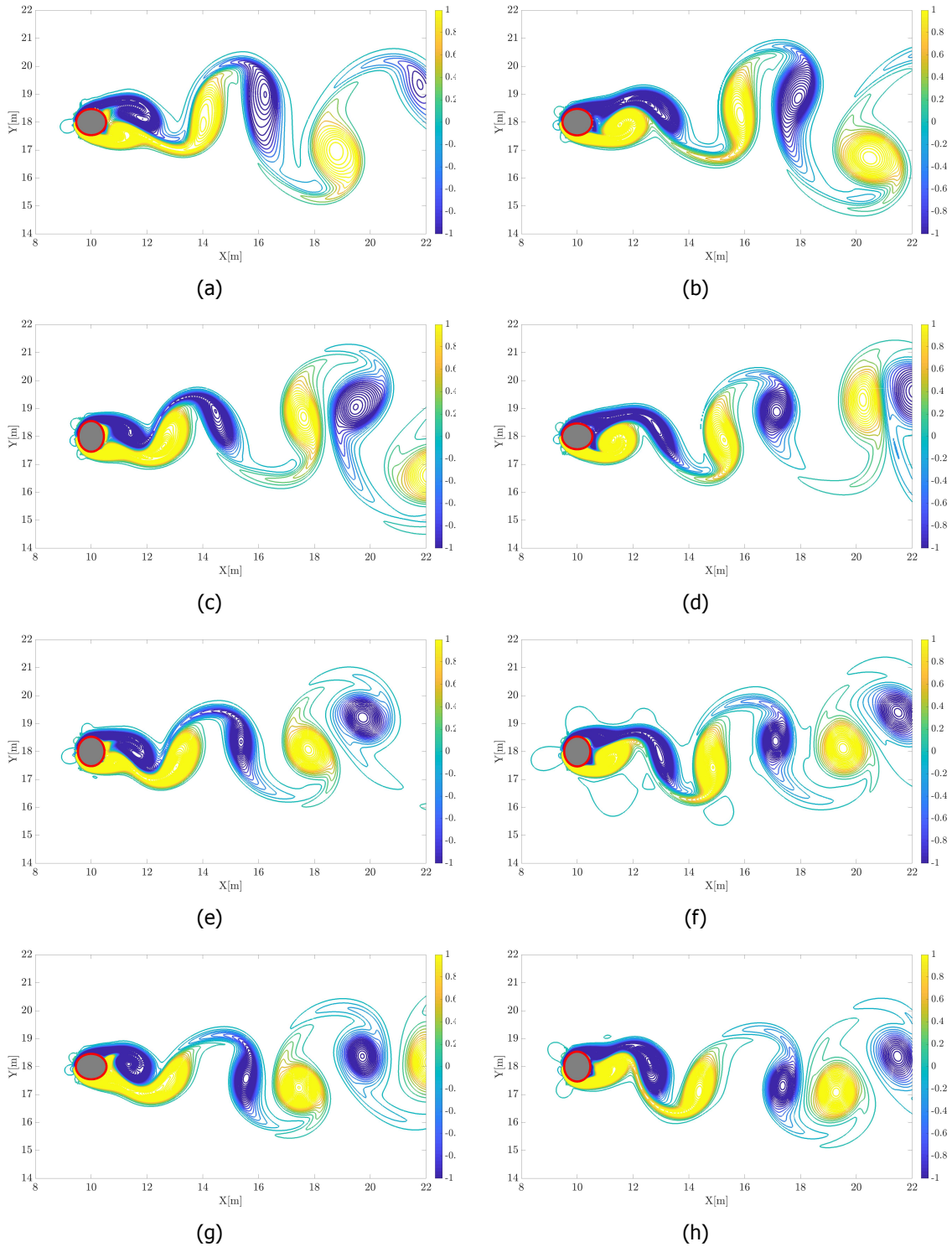

Figure A.8: Contours of the vorticity in $\frac{1}{s}$ at 10 instances of time for 2 cycles of deformation of the cylinder at $Re = 200$, $f_e = 0.75f_0$, $A = 0.1R$. 2S mode of vortex shedding is observed.

A.8. C_p for the axisymmetric flow over the sphere at $Re = 80$.

The coefficient of pressure obtained from the code is validated with that from a code that uses a body conforming grid (FLUENT) in Fig. A.9. It is found in good agreement with FLUENT.

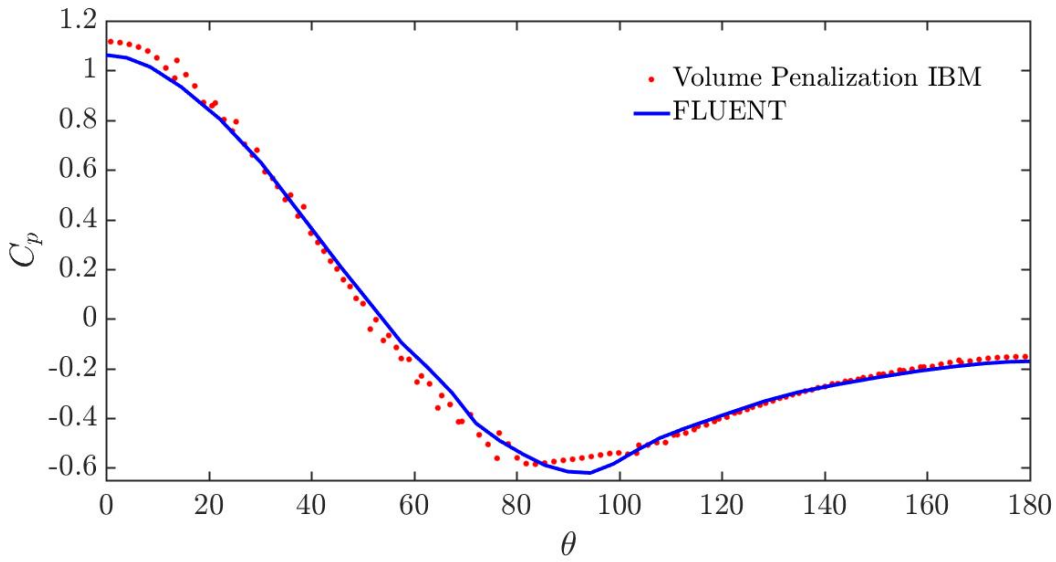

Figure A.9: Comparison of the pressure coefficient obtained from the code (shown by the red dots) and the pressure coefficient as obtained from a code that uses a body conforming grid (FLUENT) as shown by the blue line, for the flow over a sphere at a Reynolds number of 80. θ is the polar angle along the surface of the sphere (one-half).

A.9. Case 5, $s = 0.11$

The viscosity is increased by a factor of 5 and the cycle time is reduced by a factor of 5 from the case 1 to achieve the desired scale number in this case. The axial velocities are plotted with the non-dimensionalized time in Fig . A.10. The simulation is done for 12 cycles of the swimmer. The radial velocity induced is 0. The non-dimensionlized value of the axial velocity ($\frac{\overline{U}}{\omega a}$) is twice of that obtained in case 1 where the cycle time and the viscosity are five times larger and five times smaller than the cycle time and the viscosity in this case. The non-dimesionlized value for both the cases is tabulated in table A.4. There are oscillations in the axial velocities at all the monitor points in the domain. The amplitude of the oscillations at the monitor points are higher because of their finite distances to the swimmer and a higher viscosity of the fluid that is used in this case.

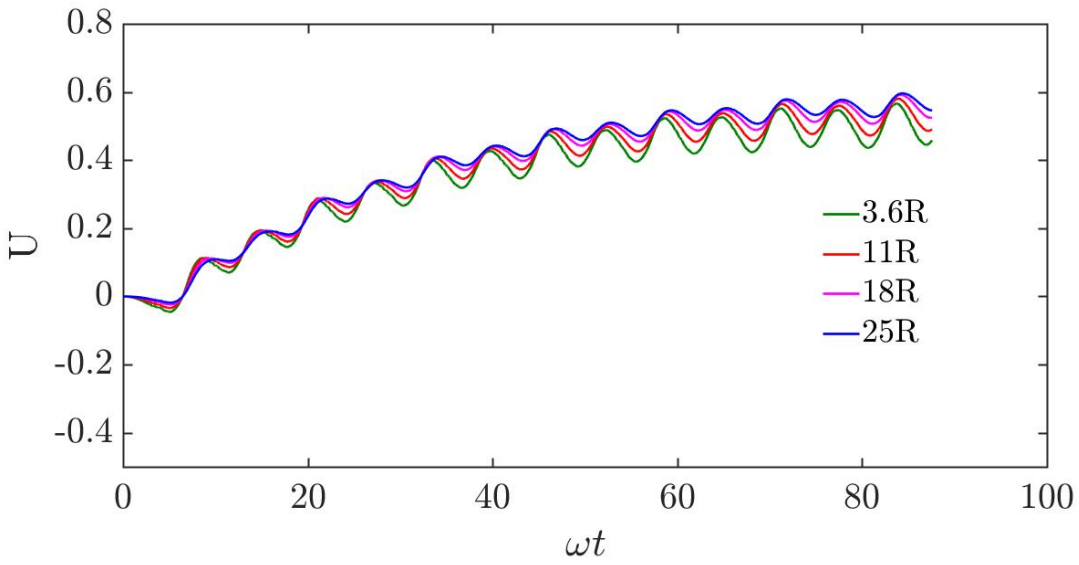

Figure A.10: The axial velocities ($\frac{m}{s}$) at the monitor points located at increasing distances from the swimmer for $s = 0.11, \nu = 500$.

Case number	$\nu(\frac{m^2}{s})$	$T_{cycle}(s)$	$\omega = \frac{2\pi}{T_{cycle}}$	$s = a\sqrt{\frac{\omega}{2\nu}}$	$Re_\omega = \frac{\omega L^2}{\nu}$	$\overline{U}\ (\frac{m}{s})$	$\frac{\overline{U}}{\omega a}$
1	100	2.5	2.51	0.11	0.0251	0.04	0.0159
5	500	0.5	12.56	0.11	0.02512	0.5	0.039

Table A.4: The Non-dimensional swimming velocities $\frac{\overline{U}}{\omega a}$ for the cases 1 and 5.